UNIVERSITY OF CALIFORNIA, SAN DIEGO

SAN DIEGO STATE UNIVERSITY

Ground Motion and Variability from 3-D Deterministic Broadband Simulations

A dissertation submitted in partial satisfaction of the
requirements for the degree
Doctor of Philosophy

in

Geophysics

by

Kyle Brett Withers

Committee in charge:

University of California, San Diego

Yifeng Cui
Enrique Luco
Peter Shearer

San Diego State University

Kim Olsen, Chair
Peter Blomgren
Steven Day

2016

The dissertation of Kyle Brett Withers is approved, and it is acceptable in quality and form for publication on microfilm and electronically:

_____

_____

_____

_____

_____

_____

Chair

University of California, San Diego
San Diego State University

2016

DEDICATION

To Winston Withers

EPIGRAPH

If you think you understand quantum mechanics,
you don't understand quantum mechanics.

– Richard Feynman

TABLE OF CONTENTS

Signature Page iii

Dedication iv

Epigraph v

Table of Contents vi

List of Figures ix

List of Tables xvi

Acknowledgements xvii

Vita xviii

Abstract of the Dissertation xix

Chapter 1 Introduction 1
1.1 Motivation 1
1.2 Background 2
1.2.1 GMPEs 2
1.3 Ground Motion Simulation Components 4
1.3.1 Rough Fault Topography 4
1.3.2 Frequency Dependent Attenuation 4
1.3.3 Small-scale Heterogeneity 5
1.4 Thesis overview 6

Chapter 2 Memory-Efficient Simulation of Frequency Dependent Q . . 7
2.1 Abstract 7
2.2 Introduction 8
2.3 Background 11
2.4 Method 13
2.5 Numerical Tests 17
2.6 Applications 20
2.7 Discussion 24
2.8 Conclusions 26
2.9 Data and Resources 27
2.10 Acknowledgments 27
2.11 Appendix 42
2.11.A Additional Figures 42
2.12 References 47

Chapter 3 Ground Motion and Intraevent Variability from 3-D Deterministic Broadband (0-7.5 Hz) Simulations along a Non-planar Strike-slip Fault 51
3.1 Abstract 51
3.2 Introduction 52
3.3 Background 54
3.3.1 Hybrid Deterministic-stochastic Broadband Approach 54
3.3.2 Rough Fault Topography 55
3.3.3 Frequency Dependent Attenuation 56
3.3.4 Small-scale Heterogeneity 56
3.4 Method 57
3.4.1 Rough Fault Topography 57
3.4.2 Simulations Details 59
3.4.3 Frequency Dependent Attenuation 61
3.4.4 Small-scale Heterogeneity 61
3.5 Results 63
3.5.1 Qualitative Comparions 63
3.5.2 Effects of Q 64
3.5.3 Effects of Heterogeneity 67
3.5.4 Duration 72
3.5.5 Pulse Period 73
3.6 Discussion 75
3.6.1 κ 75
3.6.2 Future Work 78
3.7 Conclusions 82
3.8 Data and Resources 84
3.9 Acknowledgments 85
3.10 Author Addresses 104
3.11 Appendix 105
3.11.A Verification of the Two-step Procedure 105
3.11.B Accuracy of Small-scale Heterogeneity Implementation 107
3.11.C Log-normality of Residuals 116
3.12 References 124

Chapter 4 Validation of Deterministic Broadband (0-8 Hz) Ground Motion and Variability from Ensemble Simulations of Buried Thrust Earthquakes 131
4.1 Abstract 131
4.2 Introduction 133
4.3 Background 134
4.4 Method 135

4.4.1 Dynamic Simulations 135
4.4.2 Kinematic Simulations 136
4.5 Results 138
4.5.1 Spectral Acceleration 138
4.5.2 Cumulative Absolute Velocity 142
4.5.3 $SA_{RotD100}/SA_{RotD50}$ 144
4.5.4 ϵ 144
4.5.5 Bias 145
4.6 Discussion 146
4.6.1 R_x Dependence 146
4.7 Conclusions 147
4.8 Data and Resources 148
4.9 Acknowledgments 149
4.10 Appendix 169
4.10.A Verification of the Two-step Procedure 169
4.11 References 171

Chapter 5 Conclusions 173
5.0.1 Overview 173
5.1 Summary of findings 174
5.2 Future research directions 176

LIST OF FIGURES

Figure 2.1: (a) Comparison of fits obtained between model Q (dashed line) and target Q (solid line) for several values of γ in equation (2) using the low-loss approximation as in equation (8) for an unscaled Q. (b) Ratio between target model and approximations shown in (a). 28

Figure 2.2: (a) Comparison of fits obtained between model Q (dashed line) and target Q (solid line) for several values of γ in equation 2 using the interpolation coefficients in equation (15) for effective Q in equation (12) at an example value of $Q = 20$. (b) Ratio between target model and approximations shown in (a). 29

Figure 2.3: Half-space point source test: Comparison of FK and FD results for an elastic medium. 30

Figure 2.4: Half-space point source Test: Comparison of FK and FD results for a constant Q model with $\gamma = 0.0$. 31

Figure 2.5: Half-space point source test: Comparison of FK and FD results for a Q(f) model where $\gamma = 0.6$. 32

Figure 2.6: Layered-model point source test: Comparison of FK and FD results for a Q(f) model with $\gamma = 0.6$. 33

Figure 2.7: Simulated region of the Chino Hills event (rectangle) and location of 110 strong ground motion stations with 6 stations highlighted that are plotted in Figure 2.8. The star depicts the epicenter for the Chino Hills source. 33

Figure 2.8: Comparison between data and synthetic velocity time-series, energy (normalized by density), and Fourier amplitude spectra for the east-west component of motion at stations ordered with increasing distance to the fault. The labels to the left show the station's network name, distance to the epicenter while the right labels show the peak ground velocity. The seismograms are bandpassed from $0.1 - 4$ Hz while the energy plots are bandpassed from $1.0 - 4.0$ Hz. 34

Figure 2.9: Cumulative energy as a function of distance to the fault for time series band-passed between 1.0 and 4.0 Hz using the strong ground motion stations in Figure 2.7. Dots depict values for individual stations and lines depict a 5-point moving average. R_{rup} indicates the closest distance to the ruptured surface of the fault plane. 35

Figure 2.10: Median spectral acceleration as a function of distance centered at 3 s using the strong ground motion stations in Figure 2.7 as compared to the range of several GMPE predictions. A 5-point moving average was used for both synthetics and data for the strong ground motion station locations. R_{rup} indicates the closest distance to the ruptured surface of the fault plane. 36
Figure 2.11: Similar to Figure 2.10, but here at 0.4 s. 37
Figure 2.12: Fourier amplitude as a function of distance centered at 3.5 Hz using the strong ground motion stations in Figure 2.7. Dots depict values for individual stations and lines depict a 5-point moving average. R_{rup} indicates the closest distance to the ruptured surface of the fault plane. 38
Figure 2.A.1: Layered-model point-source test: comparison of (f-k) and FD results for an elastic model for (left) velocity and (right) Fourier amplitude. 43
Figure 2.A.2: Median spectral acceleration (in units of gravity) as a function of distance centered at 1 s, using the strong ground motion stations in Figure 2.7 as compared to the range of several ground-motion prediction equation (GMPE) predictions. A five-point moving average was used for both synthetics and data for the strong ground motion station locations. R_{rup} indicates the closest distance to the ruptured surface of the fault plane. 44
Figure 2.A.3: Fourier amplitude as a function of distance centered at 0.25 Hz, using the strong ground motion stations in Figure 2.7. Dots depict values for individual stations, and lines depict a five-point moving average. R_{rup} indicates the closest distance to the ruptured surface of the fault plane. 45
Figure 2.A.4: Fourier amplitude as a function of distance centered at 2.25 Hz using the strong ground motion stations in Figure 2.7. Dots depict values for individual stations, and lines depict a five-point moving average. R_{rup} indicates the closest distance to the ruptured surface of the fault plane. 46

Figure 3.1: (Left) Model geometry and dimensions of the strike-slip rough fault used in this study. The rupture surface uses 4.7 million subfaults that follows a self-similar fractal distribution with wavelengths ranging from 80 meters to 80 kilometers. The strike slip fault is 80 kilometers in length, and 16 km in width. Reproduced in full from Shi and Day (2013). (Right) 1D layered velocity used in the dynamic simulation derived from the SCEC broadband platform validation exercise for southern California. 86

Figure 3.2: Model domain (rectangle) used in our 3D models with the same dimensions as the 1D simulations ($204, 124, 41$ km). The intersection of fault plane along surface is shown by the line, input along a 80 km segment of the San Andreas Fault. The star depicts the epicenter. 87

Figure 3.3: Example of small-scale heterogeneity of V_s (m/s) along the free surface with a correlation length of 150 m, anisotropy factor (vertical-to-horizontal stretch) of 5, and a standard deviation of 5% across the model domain. The black line indicates the surface intersection of the rough fault and the star depicts the epicenter. 88

Figure 3.4: (Left) Surface view of shear wave velocity (m/s) extracted from the CVM including the GTL. (Right) Same as the left, with the addition of a statical model of heterogeneity superimposed on the background 3D model, here before clamping the minimum V_s in the background CVM. 88

Figure 3.5: Snapshots of the fault-parallel velocity at the surface at two moments in time using a 1D layered background model (m/s). (Left) No small-scale media heterogeneity is included. (Right) Small-scale media heterogeneity with vertical correlation length of 150 m, $H = 0.05$, and $\sigma = 5\%$. 89

Figure 3.6: GMRotD50 maps of spectral acceleration in units of g at T = 0.3 s. (Left) Models without statistically-described media heterogeneity. (Right) Models with statistically-described media heterogeneity using a vertical correlation length of 150 m, $H = 0.05$, and $\sigma = 5\%$. (Top Row) 1D layered models. (Bottom row) 3D models extracted from the CVM. 90

Figure 3.7: (Top) The spectral acceleration median (GMRotD50) for 3 periods as a function of distance. The shaded region indicates the range of the GMPE medians, where the dashed blue lines are the ± 1 and +2 interevent standard deviation. Unless specified, $Q_s = 0.05 * V_s$. (Bottom) Intraevent standard deviations as a function of distance, with the shaded area indicating the 2014 intra-event standard deviation range of 4 GMPE models. 91
Figure 3.8: SA and intraevent variability for a characteristic long and short period showing the influence of several models of heterogeneity compared with GMPE predictions and a hybrid technique using a 1D background layered velocity model. 'Hetero' refers to small-scale heterogeneity. 92
Figure 3.9: Similar to Figure 3.7, but using a 3D background model extracted from the CVM. 93
Figure 3.10: Accelerograms extracted from a profile perpendicular to the fault for a background 1D layered model, with coordinates as given in Figure 3.6 for models with 0 (red), 5 (green) and 10% (black) value of σ in heterogeneity shown in Figure 3.8. 94
Figure 3.11: Accelerograms extracted from a profile perpendicular to the fault for a background 3D CVM, with coordinates as given in Figure 3.6 for models with 0 (red), 5 (green) and 10% (black) value of σ in heterogeneity shown in Figure 3.9. . 95
Figure 3.12: Median and intraevent variability for $5 - 95\%$ duration of Arias Intensity for a 1D background layered structure. . . 96
Figure 3.13: Similar to Figure 3.11, but using a 3D background model extracted from the CVM. 97
Figure 3.14: Regions where a directivity pulse occurs and its corresponding pulse period (s) for (left) 1D and (right) 3D background models. 98
Figure 3.15: (Left) Pulse Period as a function of distance. (Right) Gray bins are the number of stations as each distance, with red and green colored bins the number of stations observed to have a pulse period. 99
Figure 3.16: We calculate κ for both 1D and 3D background models, with and without heterogeneity over the relatively narrow bandwidth 5-7 Hz. (Left) Plot of stacked energy for stations at a distance of $r_{rup} = 5$km with corresponding sloping lines used to calculate κ. (Right) Plot of κ compared with the Anderson and Hough (1984) empirical relation for hard rock sites. 100

Figure 3.17: κ values calculated over the bandwidth 2-7 Hz, using the new approach, described in the text for (Left) 1D and (Right) 3D background models. 101
Figure 3.18: (Top) Spectral acceleration at a long and short period and (bottom) corresponding intraevent variability, using a 1D layered background velocity model. We also include the comparison with a hybrid broadband approach (SDSU) that is generated from the low-frequency deterministic synthetics. 102
Figure 3.19: Same as Figure 3.18, but using a 3D background velocity model. 103
Figure 3.A.1: (a) Comparison of fits obtained between dynamic and wave-propagation codes, SORD and AWP respectively, for (a) 3-component time-series low-passed to 10 Hz and (b) Fourier spectra. This station is 9 km along the fault-parallel direction and 9 km perpendicular from the hypocenter in an elastic homogeneous background model. 106
Figure 3.B.1: 3-component seismograms and spectra for a homogenous model comparing the FK, AWP, and SW4 approaches. . 110
Figure 3.B.2: Envelope and phase misfits for a homogenous model comparing the FK, AWP, and SW4 approaches, corresponding to Figure 3.B.1. 110
Figure 3.B.3: Same as Figure 3.B.1, but using a layered model plotted in Figure 3.1. 111
Figure 3.B.4: Envelope and phase misfits for a layered model comparing the FK, AWP, and SW4 approaches, corresponding to Figure 3.B.3. 111
Figure 3.B.5: Same as Figure 3.B.1, but using a layered model with superimposed 1D (vertical) small-scale heterogeneity. 112
Figure 3.B.6: Envelope and phase misfits for 1D (vertical) small-scale heterogeneity superimposed on a layered model comparing the FK, AWP, and SW4 approaches, corresponding to Figure 3.B.5. 112
Figure 3.B.7: Same as Figure 3.B.1, but using a homogenous model with 3D small-scale heterogeneity superimposed, comparing just the AWP and SW4 techniques. 113
Figure 3.B.8: Envelope and phase misfits for 3D small-scale heterogeneities superimposed on a background homogenous model comparing the FK, AWP, and SW4 approaches, corresponding to Figure 3.B.7. 113
Figure 3.B.9: Envelope misfit plots for the 3D models shown in Figure 3.B.7. 114
Figure 3.B.10: Phase misfit plots for the 3D models shown in Figure 3.B.7. 115

Figure 3.C.1: (Left) Histogram of spectral acceleration residuals at 3.33 Hz with corresponding normal distribution and (right) q-q plot for the 1D layered model with small-scale heterogeneity (5 % σ and $CL = 150$ m). The blue points map the normal distribution and the black lines show the 95% confidence interval of the normal distribution residuals given the size of the data sample. 119
Figure 3.C.2: Same as Figure 3.C.1 but using a 3D background model with small-scale heterogeneity superimposed. 120
Figure 3.C.3: Directivity amplitude correction factor from Spudich et al. (2013) to distinguish regions of forward and backward directivity for the 1D layered strike-slip model. 121
Figure 3.C.4: Same as Figure 3.C.1, but using only the stations located in the backward directivity regions. 122
Figure 3.C.5: Same as Figure 3.C.1, but using only the stations located in the forward directivity regions. 123

Figure 4.1: Rough fault geometry of dip-slip fault with complex geometry modeled off the dimensions of the 1994 Northridge earthquake. 150
Figure 4.2: Final slip along the fault (m). 151
Figure 4.3: (Top) Maximum slip-rate (m/s) along the 3 different rupture models. 152
Figure 4.4: Simulation region location (large rectangle) with strong ground motion stations indicated by triangles. Small box indicates vertical projection of rupture plane to surface. 153
Figure 4.5: Plot of small-scale media heterogeneity of shear wave velocity at surface for a background velocity model with minimum V_s of 863 m/s. The correlation length = 150 m, with $H = 0.05$, and $\sigma = 5\%$. 154
Figure 4.6: Map-view of shear wave velocity extracted from CVMSi.426, including a GTL layer (left) without and (right) with small-scale media heterogeneity. 155
Figure 4.7: Average of 4 GMPE media predictions of SA(g) at a period of 0.3 s for (left) for 1D-layered model and (right) for the 3D CVM including a GTL layer. 156
Figure 4.8: Spectral acceleration of $T = 0.3$ s in g for (top) models without small-scale heterogeneity, and (bottom) including small-scale heterogeneity. The left 3 columns indicate the three hypocenter locations as in Figure 4.4, with the rightmost column the average of the three. 157

Figure 4.9: (Top) Median spectral acceleration and (bottom) intraevent variability as a function of period at a short, medium and far distance within our model domain. 'Hetero' refers to small-scale heterogeneity. 158
Figure 4.10: Spectral acceleration at 0.3 s (g) for a background CVM model (left) without small-scale heterogeneity, (middle) including small-scale heterogeneity, and (right) including both plasticity and small-scale heterogeneity. 159
Figure 4.11: (Left) Reduction of SA % at 0.3 s for Event 1 when including plasticity within the model. (Right) Final principal plastic strain η at the surface (log units) corresponding to Event 1 plotted in Figure 4.10. The rectangle and line depict the surface projection of the fault plane and the projection of the fault to the surface, respectively. 160
Figure 4.12: Similar to Figure 4.8, but using a 3D model with stations located in the basin. 161
Figure 4.13: Same as Figure 4.12, but for rock sites. 161
Figure 4.14: CAV versus distance for 1D layered velocity models. 'Hetero' refers to small-scale heterogeneity. 162
Figure 4.15: CAV versus distance for 3D background CVM velocity models for basin sites. 'Hetero' refers to small-scale heterogeneity. 163
Figure 4.16: Same as Figure 4.17 but for rock sites. 'Hetero' refers to small-scale heterogeneity. 164
Figure 4.17: $SA_{RotD100}/SA_{RotD50}$ across period and intraevent variability prediction and comparison with synthetic models. 'Heterogeneity' refers to small-scale heterogeneity. 165
Figure 4.18: Correlation of ϵ at a reference period of (left) 0.3 and (right) 3 s for empirical and synthetic models. 'Heterogeneity' refers to small-scale heterogeneity. 166
Figure 4.19: Bias (ln[data/model]) of spectral acceleration, depicting median, 95% confidence interval, and standard deviation. 'Hetero' refers to small-scale heterogeneity. 167
Figure 4.20: Spectral Acceleration (g) versus R_x for averaged profiles within the fault strike, for (left) 1D layered models, and (right) 3D CVM structures. (Top) is for period of 3.0 s and (bottom) for 0.3 s. 'Hetero' refers to small-scale heterogeneity. 168
Figure 4.A.1: (Left) Comparison of fits obtained between dynamic and wave-propagation codes, SORD and AWP respectively, for (a) time-series low-passed to 4 Hz and (b) Fourier spectra. 170

LIST OF TABLES

Table 2.1: Relaxation times and weight coefficients for a range of power law exponents*. 39
Table 2.2: Relaxation times and weight coefficients for a range of power law exponents. 40
Table 2.3: Media parameters defined in layered model. 41

ACKNOWLEDGEMENTS

I would like to thank my advisor, Kim Olsen. Next, I would like to thank my thesis committee for their advice, in particular, Steven Day. I would like to thank my coauthors, including Zhejiang Shi. I would also like to thank the many students and Postdocs I have worked with and become friends with over the years.

Chapter 2, in full, is a reformatted version of the material as it appears in *Bull. Seism. Soc. Am.*: Withers, K., K. Olsen and S. Day. (2015) Memory Efficient Simulation of Frequency Dependent Q, *Bull. Seism. Soc. Am.* 105, 3129-3142. I was the primary investigator and author of this paper.

Chapter 3, in full, is a reformatted version of a paper currently being prepared for submission for publication to *Bull. Seism. Soc. Am.*: Withers, K. K. Olsen, and S. Day. Ground Motion and Intraevent Variability from 3-D Deterministic Broadband (0-8 Hz) Simulations along a Non-planar Strike-slip Fault. (2016). I was the primary investigator and author of this paper.

Chapter 4, in full, is a reformatted version of a paper currently being prepared for submission for publication to *Bull. Seism. Soc. Am.*: Withers, K. K. Olsen, Z. Shi, and S. Day. Validation of Deterministic Broadband (0-8 Hz) Ground Motion and Variability from Ensemble Simulations of Buried Thrust Earthquakes based on the 1994 Northridge Earthquake. (2016). I was the primary investigator and author of this paper.

VITA

2007	A. S., Pima Community College
2010	B. S. in Physics and Applied Math, University of Arizona
2016	Ph. D. in Geophysics, University of California, San Diego and San Diego State University

PUBLICATIONS

Withers, K. K. Olsen, Z. Shi, and S. Day. Validation of Deterministic Broadband (0-8 Hz) Ground Motion and Variability from Ensemble Simulations of Buried Thrust Earthquakes. (2016) (currently being prepared for submission for publication to *Bull. Seism. Soc. Am.*).

Withers, K. K. Olsen, and S. Day. Ground Motion and Intraevent Variability from 3-D Deterministic Broadband (0-8 Hz) Simulations along a Non-planar Strike-slip Fault. (2016) (currently being prepared for submission for publication to *Bull. Seism. Soc. Am.*).

Withers, K., K. Olsen and S. Day. (2015) Memory Efficient Simulation of Frequency Dependent Q, *Bull. Seism. Soc. Am.* 105, 3129-3142.

ABSTRACT OF THE DISSERTATION

Ground Motion and Variability from 3-D Deterministic Broadband Simulations

by

Kyle Brett Withers

Doctor of Philosophy in Geophysics

University of California and San Diego, 2016
San Diego State University, 2016

Professor Kim Olsen, Chair

The accuracy of earthquake source descriptions is a major limitation in high-frequency (> 1 Hz) deterministic ground motion prediction, which is critical for performance-based design by building engineers. With the recent addition of realistic fault topography in 3D simulations of earthquake source models, ground motion can be deterministically calculated more realistically up to higher frequencies. We first introduce a technique to model frequency-dependent attenuation and compare its impact on strong ground motions recorded for the 2008 Chino Hills earthquake. Then, we model dynamic rupture propagation for both a generic strike-slip event and blind thrust scenario earthquakes matching the fault geometry of the 1994 Mw 6.7 Northridge earthquake along rough faults up to 8 Hz. We

incorporate frequency-dependent attenuation via a power law above a reference frequency in the form $Q_0 f^n$,with high accuracy down to Q values of 15, and include nonlinear effects via Drucker-Prager plasticity. We model the region surrounding the fault with and without small-scale medium complexity in both a 1D layered model characteristic of southern California rock and a 3D medium extracted from the SCEC CVMSi.426 including a near-surface geotechnical layer.

We find that the spectral acceleration from our models are within 1-2 interevent standard deviations from recent ground motion prediction equations (GMPEs) and compare well with that of recordings from strong ground motion stations at both short and long periods. At periods shorter than 1 second, Q(f) is needed to match the decay of spectral acceleration seen in the GMPEs as a function of distance from the fault. We find that the similarity between the intraevent variability of our simulations and observations increases when small-scale heterogeneity and plasticity are included, extremely important as uncertainty in ground motion estimates dominates the overall uncertainty in seismic risk. In addition to GMPEs, we compare with simple proxy metrics to evaluate the performance of our deterministic models and to determine the importance of different complexities within our model. We find that 3D heterogeneity, at both the long and short scale-lengths, is necessary to agree with data, and should be included in future simulations to best model the ground motion from earthquakes.

Chapter 1

Introduction

1.1 Motivation

The strong shaking created by large magnitude earthquakes is of principal interest to structural engineers to determine the ground motion a building must be able to endure. Typically, a building's response is designed to withstand a peak motion described by some metric, such as peak ground acceleration or spectral acceleration at a certain frequency. Ground motion prediction equations (GMPEs) seek to predict this motion by using empirical observations of events. Along with a median value for the ground motion, there is also an uncertainty associated with the GMPEs' prediction; this is limited by the finite number of observations, and is currently constant as a function of distance in most implementations, but varies as a function of period. At moment magnitudes > 6, there is a shortage of observations at distances close to the source. Thus, features from synthetic simulations have been used to supplement the database. This has been done successfully at low frequencies (< 1 Hz or so) for many years, but only recently has there been the computational ability to facilitate 3D simulations of high frequency earthquakes at significant distances from the source. The importance is due to the simple fact that a building's response is related to its height; a rough approximation is 0.1 second period per individual story. A 10 story building would have a natural frequency near 1 Hz, but anything shorter would have a higher resonant frequency. Thus, it is extremely important to extend earthquake ground motion prediction to

higher frequencies, to determine the seismic hazard to these shorter structures.

Computational simulations allow one to generate synthetic ground motion of both historical and hypothetical events and to perform analysis on the resulting ground motion using a user-defined station distribution. This allows for a multitude of possible research avenues to explore. A particular research need is in regions where significant seismic hazard is known, but a paucity of data exists to constrain the expected ground motion. Another avenue of interest is investigation into reducing the ground motion uncertainty. Simulations work particularly well to accomplish this task, as they can produce a large dataset of stations to work with and extract important characteristics and statistics from. This can be done both in regions where synthetics can be compared with recorded data, and regions where no recent historical earthquakes have occurred.

1.2 Background

3D wave propagation simulations of ground motions are already playing a role in assessment of hazard and risk: 1) prediction of ground motion for scenario earthquakes for planning of earthquake emergency response and public earthquake preparedness exercises, 2) physics-based seismic hazard assessment and 3) complementing ground motion prediction equations in regions of poor sampling. The ability to extend deterministic ground motion predictions to higher frequencies and predict PGA and PSA is invaluable for structural engineers, as there is only a finite amount of empirical data from prior earthquakes to determine future seismic hazard.

1.2.1 GMPEs

GMPEs are used in seismic design codes, national seismic hazard maps, earthquake loss and risk modeling, as well as site-specific seismic hazard evaluations for important critical factors. GMPEs incorporate datasets of many records at multiple stations for many earthquakes using sources at different distances to build site-specific ground motion. This is based on a group of parameters, such

as magnitude, distance, style of faulting, site conditions, and others. The models predict a median and a standard deviation term (sigma), the latter of which is extremely important for probabilistic seismic hazard analysis (PSHA), as it controls the hazard level at very low probabilities of exceedance. An important goal for PSHA is to reduce the sigma associated with ground motion prediction equations, which has remained stable over the past 40 years. The uncertainty has been applied both with and without the ergodic assumption that assumes that the variability of ground motion at a single station is the same as the variability in a more global dataset. Thus PSHA based on the ergodic assumption can overestimate the hazard. Dropping this assumption typically reduces the variability, but requires site-specific and path-specific ground motion models, which, if lacking, will increase the epistemic uncertainty (scientific uncertainty caused by limited data and knowledge). Part of the aleatory sigma (random variability) can be transferred to the epistemic uncertainty (which in turn may be reduced by increased knowledge of source, path and site effects) if repeated measurements are available.

The uncertainty can be separated into inter- (between) and intra- (within) event terms. The between-event residual corresponds to the average source effects, depending on stress drop and other factors not included in the statistical GMPE model. The within-event residual includes azimuthal variations in the source, path, and site effects that correspond to crustal heterogeneity, geological structure, and near-surface layering not captured in a site calibration (typically based on average shear-wave velocity). The within-event variability can be subdivided into site-specific effects where there are multiple records from earthquakes at one site, and path-specific effects, where there are multiple recordings from earthquakes located in a constrained source region. This systematic path effect variability can be used to reduce uncertainty in ground motion prediction. Site and path effects will become even more significant at higher frequencies. For path effects, heterogeneity at both large and small scales is important for reducing uncertainty, depending on the frequency bandwidth of interest.

1.3 Ground Motion Simulation Components

There are several components that can affect ground motion spatial patterns and amplitudes. Next, we introduce a few that we will consider within this thesis.

1.3.1 Rough Fault Topography

Faults manifest varying degrees of geometrical complexities over a broad range of scales: from large-scale features such as branching and segmentation to smaller-scale features such as topographic variations on the fault slip surfaces. Earthquake rupture propagation along a rough-fault surface can excite high-frequency radiation as rupture fronts accelerate, decelerate, or lose coherence from the interaction with geometric irregularities. Meanwhile, changes of rupture properties such as the amplitude and shape of the slip rate induced by fault roughness can lead to a heterogeneous distribution of fault slip.

With the recent addition of realistic fault topography in 3D simulations of earthquake source models, ground motion can be deterministically generated more accurately up to higher frequencies. The synthetic ground motions have been shown to match the characteristics of real data, having a flat power spectrum up to some cutoff frequency, generated because of the complex motion of the rough fault as it propagates due to the complex stress field generated by the topography.

1.3.2 Frequency Dependent Attenuation

Anelastic attenuation is modeled via the use of the quality factor, Q, related to the change in peak strain energy loss per cycle. It is a physical parameter required for accurate simulation of seismic wave propagation, critically important for strong ground motion prediction. Simulation of Q using time-domain techniques has been notoriously difficult, mainly due to its computational requirements. The technique has been to add memory variables into the simulation via the use of relaxation functions. These relaxation functions can approximate the attenuation and dispersion by specifying a set of weights and relaxation times to fit a target Q spectrum.

In previous studies, numerical simulations using time-stepping routines, such as the finite difference method, have been restricted to constant Q models, where the weights that scale the relaxation times have been chosen with various algorithms or simply set equal to a constant. These simulations have been mostly confined to $1-2$ Hz. In the bandwidth below about 1 Hz, observations show that a constant-frequency attenuation relationship is appropriate. At higher frequencies, however, ground motion data indicates that anelastic attenuation decreases as frequency increases. This behavior is typically found to follow the form of a power-law:

$$Q(f) = Q_0 \cdot (f/f_0)^{\gamma}, \tag{1.1}$$

where f_0 is a reference frequency with Q_0 and γ constants that vary with the region and geology.

1.3.3 Small-scale Heterogeneity

The shaking caused by earthquakes can be dramatically amplified by local site effects, with prominent examples from the 1989 Loma Prieta earthquake in the Marina District of San Francisco and the 1985 Michoacan earthquake in Mexico City. The variation of the soil amplification over short distances (from tens to hundreds of meters) is important for the design of structures such as bridges and pipelines, or other constructions that extend over considerable horizontal length. State of the art area-specific Community Velocity Models (CVMs), e.g., the Southern California Earthquake Center (SCEC) CVM version 4.0 and CVM-H, resolve near-surface velocities at best on the order of kilometers. However, the resolution of small-scale amplification effects at about 1-2 Hz, the approximate maximum frequencies in state of the art ground motion simulations, typically requires a resolution of the velocities less than 1 km. Due to the expensive acquisition of the data, it may not be feasible in the foreseeable future to capture the rapid spatial variation of the near-surface material by deterministic methods. Previous studies have investigated the importance of small-scale heterogeneity included within wave propagation simulation, that statistically models the variation in velocity and density throughout the medium.

1.4 Thesis overview

With the recent addition of realistic fault topography in 3D simulations of earthquake source models, ground motion can be deterministically generated more accurately up to higher frequencies. However, the earthquake rupture description is not the only source of complexity in the high-frequency ground motion; there are also scattering effects caused by small-scale velocity and density heterogeneities in the medium that can affect the ground motion intensity. Additionally, anelastic attenuation can dramatically affect the ground motions. Previous studies have been limited to constant Q across the frequency bandwidth; a more realistic representation of the earth is to model anelastic attenuation (Q) as a varying function of frequency.

Here we deterministically model earthquakes by incorporating realistic fault topography in 3D simulations of earthquake source models and include scattering effects caused by small-scale velocity and density heterogeneities in the medium that can affect the ground motion intensity. To further increase the accuracy of our model, we have implemented frequency-dependent attenuation via a power law above a reference frequency as well as including nonlinear effects through Drucker-Prager plasticity. We validate our simulations with empirical observations that make up the Next Generation Attenuation relations as well as compare to strong-motion data from individual earthquakes. Additionally, we compare with simple proxy metrics which have been shown to be consistent across a wide range of observations.

Chapters 2, 3, and 4 of this thesis were originally written to be self-contained articles suitable for individual publications. They are, however, all similar enough to one another to be contained in this thesis with a central theme.

Chapter 2 introduces the method and importance of frequency dependent attenuation. Chapters 3 and 4 build off of Chapter 2 by including Q(f), as well as including source complexity and media heterogeneity (on both small and large wavelengths) and compare the deterministic simulations with that of empirical data. Finally, in Chapter 5, we briefly summarize our findings and discuss future research plans.

Chapter 2

Memory-Efficient Simulation of Frequency Dependent Q

2.1 Abstract

Memory-variable methods have been widely applied to approximate frequency-independent Q in numerical simulation of wave propagation. The frequency-independent model is often appropriate for frequencies up to about 1 Hz, but at higher frequencies is inconsistent with some regional studies of seismic attenuation. We apply the memory-variable approach to frequency-dependent Q models that are constant below, and power-law above, a chosen transition frequency. We present numerical results for the corresponding memory-variable relaxation times and weights, obtained by non-negative least squares fitting of the Q(f) function, for a range of exponent values; these times and weights can be scaled to arbitrary transition frequency and power-law prefactor, respectively. The resulting memory-variable formulation can be used with numerical wave-propagation solvers based on methods such as finite differences or spectral elements, and may be implemented in either conventional or coarse-grained form. In the coarse-grained approach, we fit 'effective' Q for low Q values (< 200) using a nonlinear inversion technique and use an interpolation formula to find the corresponding weighting coefficients for arbitrary Q. A 3D staggered-grid finite difference implementation closely approximates

the frequency-wavenumber solution to both a half-space and layered model with a shallow dislocation source for Q as low as 20 over a bandwidth of two decades. We compare the effects of different power-law exponents using a finite-fault source model of the 2008 M_w 5.4 Chino Hills, CA, earthquake and find that Q(f) models generally better fit the strong motion data than constant Q models for frequencies above 1 Hz.

2.2 Introduction

Anelastic attenuation, modeled by the quality factor Q, is needed for accurate simulation of seismic wave propagation, which plays an important role in many areas of seismology, including strong ground motion prediction (e.g. Olsen et al., 2000; Komatitsch et al., 2004; Cui et al., 2010; Graves and Aagaard, 2011), seismic imaging (e.g. Savage et al., 2010; Tape et al., 2010; Lee and Chen, 2014), and forensic seismology (e.g. Xie, 2005). Simulation of attenuation using time-domain techniques is not computationally feasible when the viscoelastic stress-strain relationship is expressed in convolutional form. The problem has been made tractable by by approximating the stress-strain relationship with a discrete decay spectrum which gives rise to what are known as memory variables into the simulation, where each memory variable represents a relaxation process, with a characteristic time constant, satisfying a first-order differential equation (Day and Minster, 1984; Emmerich and Korn, 1987; Blanch et al., 1995). The relaxation time constants can be chosen, and the memory variables weighted, such that, collectively, the relaxations approximate a target Q(f) spectrum and the associated dispersion. The number of relaxation times is usually chosen so that the superposition of the memory variables accurately models Q across the desired bandwidth.

In principle, all relaxation times operate on each stress component, for each volume element in the simulation, and the memory-variables approach has often been implemented in that form. The added storage and calculations for an anelastic simulation are directly proportional to the number of relaxation times introduced into the approximation; in very large simulations, especially in 3D,

the added storage and computations may become burdensome. To decrease the computational burden, Day (1998) introduced the coarse-grained approach for a 3D anelastic medium, where the relaxation times and weights are distributed across the unit cells, approximating the intrinsic attenuation with a coarser sampling. Day and Bradley (2001) implemented the coarse-grained approach in a staggered-grid finite difference method, and the finite difference implementation was adapted to very low-Q media by Graves and Day (2003) and to discontinuous media by Kristek and Moczo (2003). The coarse-grained approach has also been adapted to the finite element method by Ma and Liu (2006), and to the spectral element method by van Driel and Nissen-Meyer (2014)

In previous studies, numerical simulations have mainly been restricted to constant (frequency-independent) Q models, where the memory-variable weights have been chosen with various algorithms (e.g. Emmerich and Korn, 1987; Xu and McMechan, 1998, although these approaches allowed for a more general Q) or simply set equal to a constant (Day and Bradley, 2001). Recently, Fitchtner and van Driel (2014) modeled Q with a power-law dependence on frequency across the entire model bandwidth. These approaches have been mostly used for simulations confined to frequency $f \leq 1 - 2$ Hz (e.g. Olsen et al., 2000; Komatitsch et al., 2004; Cui et al., 2010). With the recent addition of source complexities (such as surface roughness) to simulations of earthquake sources, ground motion can now be simulated by dynamically consistent sources, retaining frequencies up to roughly 10 Hz. Such simulations are generally consistent with the spectral characteristics of recorded data (Dunham et al., 2011; Shi and Day, 2013). With the continued advancement of high performance computing, high-frequency ground motion prediction can be extended to significant distances from the fault using highly scalable numerical techniques.

In the frequency range below about 1 Hz, observations show that a frequency-independent Q relationship is often an appropriate approximation (e.g. Liu et al., 1976). At higher frequencies, however, seismic observations frequently are more consistent with models in which Q is an increasing function of frequency (e.g. McNamara et al., 2012; Raoof et al., 1999; Lekic, 2009; Phillips et al., 2013). This

behavior is typically found to follow the form of a power-law:

$$Q(f) = Q_0 \cdot (f/f_0)^{\gamma}, \tag{2.1}$$

where f_0 is a reference frequency with Q_0 and γ constants that vary with the region and geology. For example, Erickson et al. (2004) found Q_0 to be in the range $100 - 150$ and $\gamma = 0.6$ - 0.7 for California, but found Q_0 to be around 650 and $\gamma = 0.3$ - 0.4 in the eastern United States, showing a weaker frequency dependence for Lg shear waves. Additionally, Phillips et al. (2013) found evidence that the frequency dependence is stronger (larger γ) in low-Q tectonic regions compared to high-Q stable areas.

Here, we use both linear and nonlinear least squares to find the weights that scale the memory variables to fit a target Q model, with no frequency dependence up to a transition frequency f_T and following a power law formulation above this transition:

$$Q(f) = \begin{cases} Q_0 & 0 < f < f_T \\ Q_0 \cdot (f/f_T)^{\gamma} & f > f_T \end{cases}, \tag{2.2}$$

where Q is the quality factor, Q_0 is the low-frequency value of Q, and $0 \leq \gamma \leq 1$. We solve for a range of possible values of γ $(0.0 - 0.9)$, linearizing the relationship between $1/Q$ and memory-variable weights for high Q (> 200) through a low-loss approximation and fitting the effective Q or harmonic average over the coarse-grained cell for low Q values $(15 - 200)$. Our technique begins with a specified set of relaxation times appropriate to the bandwidth of the simulation, and then fits the corresponding memory variable weights to the model of equation (2). We use a nominal value Q_0^* for Q_0 for high Q, so that the resulting set of weights can then be scaled to give the target Q_0 by multiplying them by the factor Q_0^*/Q_0. For low Q, we fit a discretized range of Q values and solve for a simple formula so that the weights can be quadratically interpolated. This procedure yields a Q(f) function that matches equation (2) typically within 4% across the spectrum 0.1 - 10 Hz, becoming slightly more inaccurate for high-exponent power-law models ($\gamma > 0.7$) near the transition frequency at low Q.

The method is implemented into a fourth-order staggered grid finite difference code using the coarse-grained technique with eight relaxation times dis-

tributed with periodicity of two nodes (as in Day, 1998), with a single relaxation time at each node. To verify the method, we compare synthetic seismograms computed with the finite difference program to those from a frequency-wavenumber code, and we illustrate the importance of including Q(f) in ground motion estimation by simulating the 2008 M_w 5.4 Chino Hills, California, earthquake.

2.3 Background

This section reviews the previous development of the conventional memory variable method, used as a starting point for our technique. The result is an (approximate) expression for Q in terms of N weighting coefficients and N relaxation times.

Anelastic attenuation is implemented into time-stepping routines through the use of memory variables, whereby energy is dissipated from the system. The isotropic stress (σ), strain (ϵ) relation can be written as a set of relations of the form

$$\sigma(t) = M_u \left[\epsilon(t) - \Sigma_{k=1}^{N} \xi_k(t)\right], \tag{2.3}$$

where M_u is the unrelaxed modulus and ξ_k is a memory variable. Equation (3) represents either mean stress in terms of volumetric strain (with M_u representing a bulk modulus), or a deviatoric stress component in terms of the corresponding deviatoric strain component (with M_u representing the shear modulus). The memory variables ξ_k follow the N first-order differential equations (Day, 1998):

$$\tau_k \frac{d\xi_k(t)}{dt} + \xi_k(t) = \lambda_k \epsilon(t), \tag{2.4}$$

at each relaxation time τ_k with weight λ_k (our definition of λ_k is equivalent to the product $(\delta M/M_u)\lambda_k$ of Day (1998), equation (14), where δM is the modulus defect, i.e. the unrelaxed modulus minus the relaxed modulus). These may be time-stepped using standard approximations (e.g. Day, 1998):

$$\xi_k(t+\delta t) = e^{-\delta t/\tau_k} \xi_k\left(t - \delta t\right) + \lambda_k \left(1 - e^{-\delta t/\tau_k}\right) \epsilon(t), \tag{2.5}$$

The result of approximating the stress-strain relation in the form of equation (3) is that the complex viscoelastic modulus (as a function of angular frequency ω) takes the form:

$$M(\omega) = M_u \left(1 - \Sigma_{k=1}^{N} \frac{\lambda_k}{1 + i\omega\tau_k}\right). \tag{2.6}$$

One definition of Q is

$$Q^{-1}(\omega) = \frac{Im[M(\omega)]}{Re[M(\omega)]} = \frac{\Sigma_{k=1}^{N} \frac{\lambda_k \omega\tau_k}{1+(\omega\tau_k)^2}}{1 - \Sigma_{k=1}^{N} \frac{\lambda_k}{1+(\omega\tau_k)^2}}, \tag{2.7}$$

and if we assume the low-loss approximation $\delta M << M_u$, this becomes

$$Q^{-1}(\omega) = \Sigma_{k=1}^{N} \frac{\lambda_k \omega\tau_k}{1 + (\omega\tau_k)^2}, \tag{2.8}$$

which gives a good approximation for $Q \geq 20$ in the memory intensive non-coarse-grained approach. In the case the memory-efficient coarse-grained technique is used, Graves and Day (2003) determined that the harmonic average of the modulus is more accurate than equation (6) for $Q < 20$. Equation (7), besides representing Q for a discrete approximation to an anelastic model with continuous relaxation spectrum (Day and Minster, 1984), can also be interpreted as the Q of a spring-dashpot network model of either the generalized Maxwell or generalized Zener type (e.g., Moczo, 2005). It takes the form of a sum of Debye peaks centered at frequencies given by the inverses of the respective relaxation times.

Wavespeeds input to numerical simulations usually correspond to measured or hypothesized wavespeeds at some finite reference frequency. The reference frequency has to be taken into account in the computation of the unrelaxed elastic moduli from the input wavespeeds. With a given choice of relaxation times and weighting coefficients, the unrelaxed modulus can be expressed in terms of the phase velocity c at reference frequency ω_0 by

$$M_u = \frac{c^2\rho \left(Re[\sqrt{\frac{1}{1+iQ^{-1}(\omega_0)}}]\right)^{-2}}{Re[1 - \Sigma_{k=1}^{N} \frac{\lambda_k}{1+iw_0\tau_k}]}, \tag{2.9}$$

where

$$c(\omega_0) = \sqrt{\frac{Re[M(\omega_0)]}{\rho}} \left(Re[\sqrt{\frac{1}{1 + iQ^{-1}(\omega_0)}}]\right)^{-1} \tag{2.10}$$

where ρ is density and M is given by equation (6) and Q by equation (7). In the case of effective Q, the modulus is found from:

$$M_E(\omega) = N \cdot (\Sigma_{k=1}^{N} \frac{1}{M_k(\omega)})^{-1}, \tag{2.11}$$

where

$$M_k(\omega) = M_u(1 - \frac{\lambda_k}{1 + i\omega\tau_k}) \tag{2.12}$$

and Q in equations (9) and (10) is replaced by

$$Q_E^{-1}(\omega) = \frac{Im[M_E(\omega)]}{Re[M_E(\omega)]}. \tag{2.13}$$

Equation (9) then becomes (assuming material homogeneity across the coarse-grained cell)

$$M_u = \frac{c^2\rho\left(Re[\sqrt{\frac{1}{1+iQ^{-1}(\omega_0)}}]\right)^{-2}}{N \cdot Re[\left\{\Sigma_{k=1}^{N}(1 - \frac{\lambda_k}{1+iw_0\tau_k})^{-1}\right\}^{-1}]}, \tag{2.14}$$

With these expressions, velocity dispersion corresponding to the defined Q function is accurately accounted for.

2.4 Method

It remains to describe the method for selecting the relaxation times and weights to approximate $Q(f)$; in previous applications, the target has typically been a frequency-independent Q function. When the τ_k are approximately logarithmically spaced, the frequency-independent Q model is well fit with nearly equal λ_k for each relaxation time (e.g., Day, 1998 found that even exactly equal-value λ_k gave a good fit, within 5% tolerance, to frequency-independent Q).

In the current paper, we generalize the above approach to include power-law Q(f). This generalization is done by numerical fitting of the λ_k to the target Q(f) (equation 2). Here we set the τ_k to be equally distributed logarithmically:

$$\ln \tau_k = \ln \tau_m + \frac{2k-1}{16}(\ln \tau_M - \ln \tau_m), \tag{2.15}$$

where τ_m corresponds to the minimum relaxation time and τ_M the maximum, the lower and upper absorption-band cutoffs.

The best fits are typically obtained when these limits are set outside the bandwidth of computational interest. For large Q, we use constrained least squares to solve for the λ_k in equation (8) to fit a target Q function of the form in equation (2) by minimizing the sum of the squares. The λ_k are constrained to be positive in the inversion to ensure that energy is dissipated from the system. Since equation (8) is linear in λ_k, solving for λ_k for one value of Q_0 (denoted Q_0^*) allows the weights to be scaled to any other value of Q_0, giving the same target shape as a function of frequency. For simplicity, we set $Q_0^* = 1$ (and the fitted weights can subsequently be scaled to arbitrary Q_0 by multiplication by $1/Q_0$). The low-loss approximation used here closely approximates Q (in the form of equation 7) for $Q_0 > 50$. As Graves and Day (2003) pointed out, once scaled to the desired Q_0, the sum of the the weights must be bounded above by 1 to ensure stability (and the sum is bounded below by 0, since each weight is non-negative). This condition is satisfied for all λ_k after scaling for $Q_0 > 50$ for the range of γ solved for here. The Q(f) model generated by this technique can also be shifted in frequency, so that the transition to a power-law model occurs at any specified frequency, f_T. This frequency shift is achieved by dividing the relaxation times by the desired factor; the weights remain unchanged.

Graves and Day (2003) analyzed the coarse-grained low-Q accuracy and determined that the best results are obtained when using the harmonic average of the moduli over the volume of the coarse-grained cell to determine the coefficients. We use a nonlinear least squares approach to fit equation (11) based on the conjugate gradient method with the effective weights bounded between 0 and 1 and solve for the weighting coefficients for each integer value of Q ranging from $15 - 220$. We then inverted for the coefficients (using least squares) a_k and b_k in the expression

$$\lambda_k = \frac{a_k}{Q^2} + \frac{b_k}{Q} \tag{2.16}$$

that fits Q accurately to within 5% (and generally much better) between 0.1 and 10 Hz. This is similar in concept to the interpolation technique proposed by Liu and Archuleta (2006), but uses a simpler formula, with fewer coefficients. We chose this approach up to $Q < 200$ after performing plane wave tests and determining

that even large values of Q (> 50) can be inaccurately modeled using the arithmetic modulus for wide bandwidths (> 2 decades) in the coarse-grained approach, particularly when the weighting coefficients vary significantly in magnitude.

Figure 2.1 shows an example of the fits between the target Q spectrum and the approximation, for various power-law exponents with $N = 8$ in equation (8) using the linear technique (applicable for large Q). The weights scale the individual terms (Debye peaks) in the summation of equation (8) and these terms superpose to give an approximation to the target spectrum. Here we have chosen the transition frequency f_T to be 1 Hz, and implemented a transition region between 0.8 to 1.2 Hz, where the Q spectrum is defined as a power-law function with $\gamma/2$. This region allows a better fit when using least squares to invert for the weights, as a sharp transition is impossible to fit using the superposition of Debye peaks. Figure 2.1 also plots the ratio between the target spectrum and the approximation for the same power-law exponents. It is clear that the fits are within a 5% tolerance across the entire bandwidth. The ratio is oscillatory about 1 (a perfect fit) due to the overlap of the Debye peaks.

Table 1 lists the minimum and maximum relaxation times used for each power law exponent, and the corresponding weights. We have limited this table to positive values, and to the range $\gamma = 0.0 - 0.9$, as γ can never be > 1 (Q^{-1} can never fall off faster than ω due to the shape of the Debye peak). Our technique is entirely general, in the sense that the weights determined in this manner can be used in either a conventional memory variable implementation (i.e. where the memory variables associated with all N relaxation times are calculated and summed, as in equation (3), at every stress node) or a coarse-grained implementation. In the latter case, there is an additional scale factor N related to the increased volume element represented by each memory variable in the coarse-grained discretization: λ_k on the right-hand side of equation (4) is replaced by w_k, where $w_k = N\lambda_k$ (Day, 1998, equation 43), where $N = 2^3$, for a 3D finite difference medium with a periodicity factor of 2. Note that some coefficients are near zero, indicating that there is little contribution from that relaxation time; this indicates that the bandwidth could be chosen to be wider and most likely still obtain accurate fits. We found

that the given choice of relaxation times performs well for the technique for low Q, where example spectra and fits are plotted in Figure 2.2 for $Q = 20$ using the interpolation formula as in equation (16) and the coefficients in Table 2. Here, w_k implicitly includes the factor N in λ_k already, so no normalization is required. It is evident that towards the low end of our Q range, it becomes harder for high-power law exponents to fit the transition region within 5%. Inverting for the weighting coefficients and relaxation times simultaneously would allow for a denser distribution of relaxation times near sharp changes or complex regions in the Q spectrum. However, more accurate fits in the frequency domain do not necessarily transmit to the actual coarse-grained time domain simulations, due to the dependence on the relative magnitude between coefficients and the choice of bandwidth. In practice, this misfit is probably negligible when comparing synthetics with real data, as the resolution of Q is significantly lower than this.

To accommodate both shear and bulk losses, it is convenient to absorb the unrelaxed moduli into the forcing term for the memory variable evolution equation (4) (so the memory variables have the same dimensions as stress), and remove the modulus factor on the memory variables in stress-strain equation (3). Then adding the respective evolution equations for shear and bulk, we obtain (following Day and Bradley, 2001)

$$\tau_k \frac{d\xi_{ij}}{dt} + \xi_{ij} = \lambda_k [2\mu_u Q_{s0}^{-1} \epsilon_{ij} + [(\kappa_u + \frac{4}{3}\mu_u) Q_{p0}^{-1} - 2\mu_u Q_{s0}^{-1}] \epsilon_{kk} \delta_{ij}], \tag{2.17}$$

where ϵ_{ij}, ϵ_{kk}, μ_u and κ_u are deviatoric and volumetric strains, and unrelaxed shear and bulk moduli, respectively, and Q_{s0}^{-1}, Q_{p0}^{-1} are reference values of Q_s^{-1}, Q_p^{-1}, which differs from Day and Bradley (2001) since $\frac{\delta M}{M_u}$ has now been absorbed into the weights. Adding the bulk and shear equations for stress, equation (3) becomes:

$$\sigma_{ij} = 2\mu_u \epsilon_{ij} + (\kappa - \frac{2}{3}\mu_u) \epsilon_{kk} \delta_{ij} - \Sigma_{l=1}^{N} \xi_{ijl}. \tag{2.18}$$

The time-differentiated form of equation (17) gives a first-order ODE that one can solve for the memory variable $\dot{\xi_{ij}}$ given the strain rate $\dot{\epsilon_{ij}}$. The stress rate $\dot{\sigma}_{ij}$ can then be calculated from $\dot{\xi_{ij}}$ and $\dot{\epsilon_{ij}}$. For a fixed set of weights, the righthand side of equation (17) scales linearly with Q_0^{-1}, as noted earlier (assuming $Q >> 1$).

We have implemented our technique using the memory-efficient coarse-grained approach of Day and Bradley (2001) described earlier, using a scalable staggered-grid velocity-stress finite difference (FD) method, 4th-order accurate in space and 2nd-order accurate in time (Cui et al., 2010). The weights are distributed with a period of 2 nodes, in the same periodic scheme as the corresponding relaxation times. Here the memory variables ξ_{ij} are collocated with the stresses σ_{ij} and the summation in equation (18) is removed, becoming

$$\sigma_{ij} = 2\mu_u \epsilon_{ij} + (\kappa - \frac{2}{3}\mu_u)\epsilon_{kk}\delta_{ij} - \xi_{ij}, \tag{2.19}$$

and λ_k in equation (17) replaced by w_k. The implementation assumes that Q_κ and Q_μ (where κ and μ correspond to the bulk and shear modulus, respectively) have identical frequency dependence, though they may have different prefactors Q_0. For $Q > 200$, this simplification allows us to use the same set of weights for both bulk and shear attenuation (scaled to their respective Q_0 values), though this simplification is not necessary in our approach. For $Q < 200$, or when using independent shear and bulk Q spectra, two different sets of weights are used for the bulk and shear components.

2.5 Numerical Tests

We have performed several simulations using simple earth models with a shallow dislocation source. To verify our technique, we have modified a frequency-wavenumber code (FK) (Zhu and Rivera, 2002) to account for the dispersion associated with a power-law Q(f) and used the frequency dependent modulus as given by equation (6) for the given choice of relaxation times and weights to find the complex wavenumber used in the computation. We used an iterative approach to solve for $Q^{-1}(\omega)$ as given by equation (7), where first the weights are set to some initial value (0's work fine) and inserted into the term in the denominator of equation (7). The resulting expression (identical to the low-loss approximation of equation (8) divided by a factor) is fit by using linear least squares. These weighting coefficients are used in the next iteration and the procedure is continued in

succession until there is negligible change in the coefficients or $Q(\omega)$ is fit to within a certain tolerance (2-3% is typically as accurate as can be achieved for fixed τ_k).

We use a double-couple buried point source equivalent to right-lateral slip with a strike = 90°, dip = 90°, and rake = 0° at a depth of 1.8 km, using the cosine-bell moment-rate function:

$$\dot{M}(t) = \begin{cases} M_0(1 - \cos(2\pi t/T) & 0 < t < T \\ 0 & \text{otherwise} \end{cases}, \tag{2.20}$$

with $T = 0.2$ sec and $M_0 = 10^{16}$ N m, equating to a $M_w = 4.6$ earthquake. We use a grid spacing of 40 m and a time step of 0.002 sec. The upper frequency limit (i.e. the frequency up to which the solution is accurate to within a specific tolerance) scales with minimum wave speed v_s. For example, for a minimum v_s of 2000 m/s and a resolution criterion of 5 grid points per minimum shear wavelength, the upper limit of this grid is 10 Hz. We have constructed our model domain to be large enough to have no reflections from boundaries at the receiver station during the simulated time. The source is averaged across two depth points in the FD program since the shear stress σ_{xy} in our scheme is located one-half grid point below the target grid location. As the horizontal components of the staggered-grid are located 1/2 point below the free surface, we have also averaged the horizontal components of the receiver stations to be closer to the target geometry (Gottschämmer and Olsen, 2001).

First, we compare the computed time histories obtained with a purely elastic (infinite Q) model to determine the accuracy of the FD solution for the prescribed model parameters. Here we set $v_p = 6000$ m/s, $v_s = 3464$ m/s and $\rho = 2700$ kg/m^3. Figure 2.3 shows seismograms and the Fourier spectra for each component of a surface station located at a horizontal distance of 15 km from the source with an azimuth of 53.13 °from North. The seismograms have been band-passed between 0.2 and 10 Hz using a fourth-order, zero-phase Butterworth filter; a reference frequency of $f_0 = 1$ Hz was used for calculating the unrelaxed modulus. We used the time-frequency representations of misfit between two seismograms classified as envelope misfit (EM) and phase misfit (PM) as in Kristekova et al. (2009) to determine the match quantitatively, and found arrival times of all major phases

are reproduced with phase error less than 1% and peak amplitudes are matched with relative error less than 2%. Fourier spectral amplitudes are nearly identical in the two solutions. The Rayleigh wave (4.5-5.5 s, radial and vertical components), is free of visible spurious oscillations and reproduces the wavenumber-integration solution with considerable precision.

Next, we use a viscoelastic half-space model simulating constant Q, i.e. a power law exponent of 0.0, using the values listed in Table 2, where we have set $Q_{s0} = Q_{p0} = 50$. Figure 2.4 plots the results for the same surface station as located in Figure 2.3; it is evident that the two solutions are very similar and that the FD synthetics match the analytical counterparts to high accuracy, demonstrating that the method is working well, even in the presence of the free surface. EM and PM here are less than 6% and 2%, respectively, for all components. By optimizing the weighting coefficients for effective Q, we are able to obtain better accuracy here than simply setting the coefficients equal to one another, as in Day and Bradley (2001).

Next, we implement our routine in a half-space using a power-law model with an exponent of 0.6, again with low-frequency $Q_{s0} = Q_{p0} = 50$, with Q increasing above the reference frequency of 1 Hz in the form of equation (2) using the coefficients in Table 2. The results are shown in Figure 2.5 for the same surface station as in Figures 2.3-2.4. It is evident in the seismograms that less energy has been attenuated, and that the Fourier spectra have more energy at frequencies > 1 Hz, compared to the constant-Q model. The close fit between the FK and FD waveforms indicates that our technique works well for all phases present in the uniform half space, with even better accuracy than in the constant Q model, where here maximum EM and PM are less than 2% and 1%, respectively.

To further verify our technique, we have used a simple layered model (see Table 3) composed of a thin velocity layer over a half-space, using a power-law model, $\gamma = 0.6$, with Q_{s0} and Q_{p0} values of 20 in the low-velocity layer and 210 in the underlying half-space. This problem tests the method in the presence of strata of large contrasting Q as well as seismic velocity, and also tests its performance for Love waves.

Figure 2.6 shows the comparison between the FK and FD results. It is clear that the two techniques compare very well with one another, even with Q as low as 20 and a sharp Q contrast. EM and PM here are within 5% and 2%, respectively, for the first 5 s, but increase to 8% - 10% for EM and 2% for PM for the later surface wave arrivals. The corresponding goodness-of-fit values are above 9 in the scale used in Kristekova et al. (2009), classified as an excellent fit. For reference, the elastic case is plotted in Figure 2.A.1 with maximum EM of 3% and PM of 1%. The harmonically averaged Q over the coarse-grained cell in the shallow layer and arithmetically averaged Q in the underlying half-space is seen to work well even in the presence of layer discontinuities. The larger misfits in the later arrivals would likely be smaller if heterogenous Q across the coarse-grain cell was implemented, allowing a sharper transition in Q, but we find that we have sufficient accuracy here for a much higher contrast in Q than would likely be present within the real earth. For frequency-independent Q, Kristek and Moczo (2003) show that the coarse-grained scheme loses accuracy in the presence of sharp discontinuities involving very low Q, and they propose an alternative coarse-grained formulation that is more accurate in that limit. Those results for discontinuous models are likely to apply also to the power-law case when $Q_0 << 20$.

2.6 Applications

We have shown that we obtain accurate seismograms using a frequency-dependent Q model, and that there are differences in both the amplitude and frequency content compared to a constant-Q model. To demonstrate the importance of Q(f), here we model ground motion for the 2008 M_w5.4 Chino Hills, CA, earthquake and compare results for different power-law Q models against strong motion data. We use a finite-fault source model adapted from Shao et al. (2012), obtained by inversion of local earthquake records, to model the event. Even though their model was only constrained by data up to 2.5 Hz, there is significant energy in their source above this threshold, as shown by Taborda and Bielak (2014), so we design our simulation to numerically resolve frequencies up to 4 Hz with 6.25

points per minimum wavelength. We use the Southern California Earthquake Center (SCEC) Community Velocity Model V4 (CVM-4) (Magistrale et al., 2000 and Kohler et al., 2003), limiting the minimum shear wave velocity to 200 m/s, and set the P-wave velocity to 600 m/s when this occurs. Here we choose Q_0 to be related to the shear wave velocity by the relation $Q_{s0} = v_s * 0.1$ and $Q_{p0} = 2 * Q_s$, where v_s is in km/s. We calculate Q_0 after imposing the lower limit on v_s; this ensures that the minimum Q_0 is always greater than 20. We run two end-member models with $\gamma = 0.0$ and 0.8 (0.8 is the upper limit of the γ estimate of Song and Jordan (2013) for southern California).

Figure 2.7 plots the modeled region, indicating the boundary and 110 strong ground motion stations from which data were obtained from the Center for Engineering Strong Motion Data database (see Data and Resources), to compare with our simulations. The simulation domain extends 56 by 40 km in the east and north directions, respectively, to 24 km in depth, using a grid spacing of 8 meters. We used Cerjan boundary conditions (sponge zone layers) in our 3D models, which dampens the reflections significantly, reducing energy that would reflect back into the model.

In Figure 2.8, the east-west component of individual waveforms, as well as cumulative energy (integral of particle velocity squared) and Fourier amplitude spectra, are plotted at the stations highlighted in Figure 2.7, ordered with increasing distance to the fault.

The velocity waveforms were band-pass filtered between 0.1 and 4 Hz, while the energy plots are focused on the higher frequencies, calculated from seismograms band-passed filtered between $1.0 - 4.0$ Hz. There are first-arrival amplitude differences between the two simulations and more energy in the coda for the Q(f) model relative to the constant-Q model. The frequency domain shows that the two simulations start to diverge above 1 Hz as expected, with Q(f) having more energy. At stations near the source, the similarity between the synthetics and data in this frequency range is largely related to the accuracy of the source and site effects. At stations farther from the source, there is seen to be a greater difference between the two simulations; it is clear that the Q(f) model has significantly more

energy. It is not evident whether constant Q or Q(f) performs better compared with data when looking at individual stations.

To determine the significance of Q(f) for the bulk of the data, we calculated the cumulative energy in the waveforms in the passband $1-4$ Hz for each horizontal component, and then computed the geometrical mean of these components for each station. Figure 9 plots the geometrical-mean cumulative energy as a function of the closest distance to the rupture plane r_{rup} for the strong ground motion stations in

Figure 2.7. The differences between the data and constant-Q synthetics are similar to those between data and power-law Q synthetics at distances near the fault (< 25 km). At further distances, however, there is a significant divergence between the constant-Q and power-law synthetics, with the power-law synthetics in better agreement with the data.

We next compare our Q(f) simulations to several leading ground motion prediction equations (GMPEs) (Boore and Atikinson, 2008, Campbell and Bozorgnia, 2008, Chiou and Youngs, 2008). These models are dependent on information about the source (M_w, width, etc..) as well as site effects ($Vs30$ and others) and distance to the source r_{rup}. We compute orientation independent median spectral motion (GMRotD50) (Boore et al., 2006) at several periods for both the data and our synthetic models and compare to the spectra predicted from the GMPE's. Figure 2.10 plots the range of the medians of the three different GMPE models at a period of 3 s. Also plotted is the 5 point moving average of the observed data and the synthetic predictions. We see that the strong ground motion data is similar to that of the GMPE predictions, but that there are significant differences between the data and synthetics. We attribute most of this misfit to inaccuracy in the source and the medium parameters (velocity and density), as stations near the source don't have a significant impact from Q. We see that both power-law simulations plot almost identically on top of one another, as they should at frequencies lower that 1 Hz.

Figure 2.11 plots the same thing, but at a period of 0.4 s. Here it is evident that the power-law model matches the decay in energy seen in the observations

better than the constant-Q model, as less energy has been attenuated than by the constant-Q model. The effect becomes more important at further distances from the source. Figure 2.A.2 plots the comparison at a period of 1 s, showing differences of constant Q and Q(f) intermediate between Figures 2.10 and 2.11.

The method of picking the peak spectral response includes information about a range of frequencies. Thus, we choose not to compute spectral accelerations above 2.5 Hz. Instead, we compute the Fourier spectral amplitude at several frequencies for both models and data by averaging the spectral amplitude in a narrow bandwidth (≈ 0.1 Hz) and plot those averages as a function of R_{rup}. Figures 2.A.3 and 2.A.4 show that we obtain qualitatively similar results to Figures 2.10 and 2.11 at frequencies of 0.25 and 2.5 Hz. Figure 2.12 shows the result at 3.5 Hz. Even though the source model from Shao et al. (2012) was only constrained by seismic observations up to 2.5 Hz, the figure shows that the model nonetheless generates 3.5 Hz spectral amplitudes that are consistent with observed spectra at station distances up to about 20 km, a distance range where the Q model has a less appreciable effect. Thus, we use the source model without modification to examine the effect of the Q model on the 3.5 Hz amplitude decay at larger distances. It is clear from Figure 2.12 that at distances larger than 25 km from the fault, constant-Q is too attenuating, whereas although there is considerable scatter, the Q(f) model with $\gamma = 0.8$ matches the trend of observed amplitudes better. The constant-Q model predicts amplitudes that are deficient by a factor of 3 to 5, relative to both the data and the $\gamma = 0.8$ power-law model, in the distance range considered.

We note that these simulations have used a velocity structure that is considered accurate only for estimating long-period ground motions. The waveforms would be expected to change significantly with the inclusion of scattering from small-scale heterogeneity in the media parameters. Current work is being performed to determine the significance and the role that scattering plays in ground motion simulation (Savran and Olsen, 2014). The presence of additional scattering will add complexity to the wavefield and lengthen the coda, and scattering-model parameters may trade off with anelastic parameters. Preliminary calculations con-

firm, however, that those effects are unlikely to change our conclusion about the importance of including frequency dependent Q in the model.

2.7 Discussion

Predicting amplitudes of high-frequency regional phases is important for discriminating explosions when events are small, as well as for accurate imaging in techniques determining earth's structure. Additionally, pushing deterministic simulations of earthquakes to higher frequencies is critically important for physics-based seismic hazard analysis, to enable structural engineers to design buildings and structures with shorter natural periods to withstand earthquake ground motions. As recent work has improved the accuracy of the source at higher frequencies and as computational resources have become greater, realistic ground motion up to ≈ 10 Hz has become achievable at considerable distances from the source in a 3D medium. These synthetic ground motions have been shown to match the characteristics of real data, having a flat power spectrum up to some cutoff frequency (Shi and Day, 2013). However, the earthquake source is not the only source of complexity in the high-frequency ground motion; to model ground motions accurately, the medium needs to be realistically modeled as well. Included within this complexity is the model of anelastic attenuation. As simulations extend to higher frequencies, energy losses from anelasticity become progressively more important as there are more wavelengths of propagation within a modeled domain.

Observations have shown that Q increases as frequency increases, changing from the constant behavior below 1 Hz or so. Here, we have implemented frequency-dependent Q into a staggered-grid velocity-stress FD code via a power-law function above a reference frequency, f_T: $Q = Q_0 f^{\gamma}$, where Q_0 and γ are constants that may vary with the region being studied (e.g. Phillips et al., 2013). We have used the low-loss approximation for $Q > 200$, and effective Q values lower than this.

The Q spectrum fits are generally accurate to within 5% across 2-3 decades of bandwidth. We have seen that the scheme simulates broadband frequency-

dependent Q accurately for both a half-space and a layered model as verified by agreement with the respective analytical solutions. This includes both body waves as well as surface waves. The lower limit of $Q = 15$ that we apply our approach to is not the lower bound; we choose a minimum Q value of 15, as this will be valid for almost all regions (except for very low velocity sediments) and allows us to accurately fit the rapidly changing coefficients at low values of Q with a simple interpolation formula. Additionally, for a given absorption band-width, the Q value has a lower bound determined by the thermodynamic constraint that the sum of the λ_k values be less than one (and the equivalent constraint in the coarse-grained approach is that each w_k value be less than one).

The approach demonstrated here could be applied to other grid methods, both structured and unstructured, and extended using the coarse-grained technique as long as the coarse graining periodicity is less than half the shortest seismic wavelength of interest (Day, 1998; van Driel and Nissen-Meyer, 2014). The same technique can be applied to solve for weights to fit a power law across all frequencies or a negative value of γ as found by Lindley and Archuleta (1992).

A benefit of this technique is in its flexibility; the Q spectrum can be scaled to any value of $Q > 200$ by linear scaling of the weighting coefficients and transferred to the desired frequency range simply by dividing the set of relaxation times by the desired shifting factor. Additionally, only $3N$ coefficients (where N is a small number - 8 in our examples) per Q model need to be tabulated, allowing for many different models to be easily stored in memory. In the future, as GPU hardware becomes less memory-bound, it will likely become unnecessary to use the coarse-grained approximation, and thus a more simple interpolation procedure could be used to solve for the weighting coefficients in equation (7) down to very low values of Q, again using a linear scaling relationship for large Q.

High performance computing now allows seismologists to simulate the propagation of seismic waves through 3D complex crustal structures. This includes simulating the scattering effects caused by small-scale velocity and density heterogeneities in the medium that can affect the ground motion intensity increasingly at higher frequencies. It is important to note that scattering from small-scale

heterogeneities may play a large role in the effect of attenuation in the frequency range > 1 Hz. It remains to determine the relative role of scattering versus intrinsic attenuation in high-frequency simulations and determine Q_{p0} and Q_{s0} in combination with scattering parameters. Additionally, the effects of non-planar topography should be included in future studies as this could also influence the scattering of energy.

Future work should explore regional variations in Q_0 and γ and examine the relationships of these parameters to seismic velocities, lithology, and tectonic setting. It remains to be determined whether the parameter κ in $exp(-\pi\kappa f)$ proposed by Anderson and Hough (1984), the high-frequency decay in Fourier amplitude spectra observed in ground-motion recordings, can be accurately modeled by some combination of depth variation and frequency dependence of Q. This parameter will become more important as ground-motion models are extended to frequencies beyond those covered here, where the effects of kappa are limited.

2.8 Conclusions

We have developed an approach to determine the weighting coefficients in power-law Q models for use in time-domain wave propagation techniques and found that we can fit low-order memory-variable approximations to those power laws to within 5% tolerance over 2 orders of magnitude in frequency. The resulting memory-variable models can be implemented either in conventional (point-wise) form, or in a coarse-grained version. We have verified the accuracy of the coarse-grained finite difference implementation by comparison of solutions with frequency-wavenumber synthetics for both uniform and layered half space models.

We illustrate the importance of including Q(f) in ground motion estimation by modeling the M_w 5.4 Chino Hills, CA, earthquake. We find, by looking at both the distance decay of the Fourier amplitude spectrum and the cumulative energy of seismograms at various distances from the fault, that frequency dependent Q does a better job than constant Q at frequencies above 1 Hz. Q(f) is shown to become increasingly important at higher frequencies.

The utility of our approach will also extend to many other areas of seismology besides strong ground motion prediction, including explosion monitoring and seismic imaging, where accurate prediction of amplitudes and arrival times are important.

2.9 Data and Resources

The seismograms from the 2008 Mw 5.4 Chino Hills earthquake used here were obtained from the archives of the Center for Engineering Strong Motion Data at http://www.strongmotioncenter.org/. The southern California velocity model CVM-S 4.26 can be obtained from SCEC at http://scec.usc.edu/scecpedia/.

Most of the data-processing work was done using MATLAB (http://www.mathworks.com/products/matlab/). Figures were prepared using MATLAB and the Generic Mapping Tools package (http://www.soest.hawaii.edu/gmt/). All electronic addresses referenced here were last accessed October 2014. All other data used in this paper came from published sources listed in the references.

2.10 Acknowledgments

Chapter 2, in full, is a reformatted version of the material as it appears in *Bull. Seism. Soc. Am.*: Withers, K., K. Olsen and S. Day. (2015) Memory Efficient Simulation of Frequency Dependent Q, *Bull. Seism. Soc. Am.* 105, 3129-3142. I was the primary investigator and author of this paper.

This research was supported by NSF awards OCI-1148493 (SI2-SSI), EAR-1135455 (FESD), through the Southern California Earthquake Center (SCEC). SCEC is funded by NSF Cooperative Agreement EAR-1033462 and USGS Cooperative Agreement G12AC20038. The Chino Hills simulations were generated on the Titan Cray XK7 at the Oak Ridge Leadership Computing Facility in Tennessee. Thanks to two anonymous reviewers for their help in improving the manuscript.

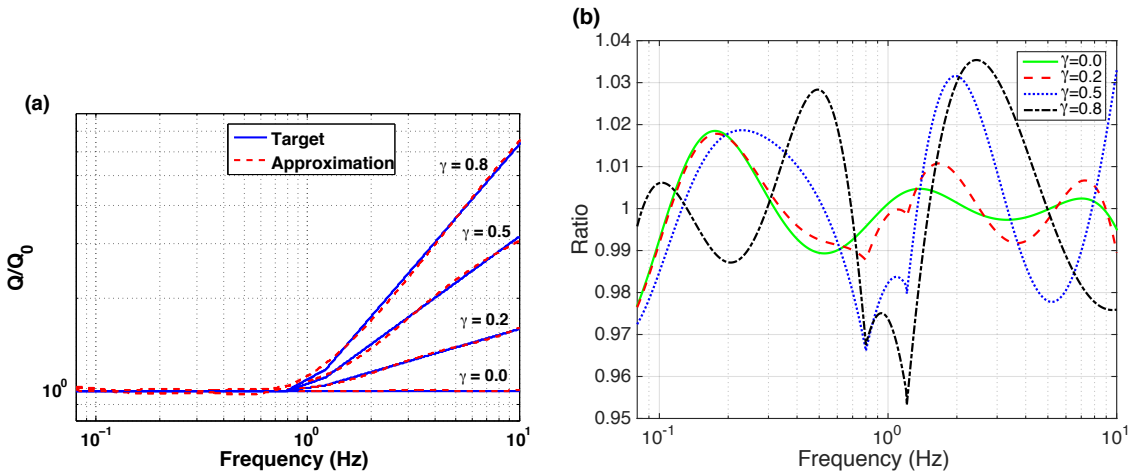

Figure 2.1: (a) Comparison of fits obtained between model Q (dashed line) and target Q (solid line) for several values of γ in equation (2) using the low-loss approximation as in equation (8) for an unscaled Q. (b) Ratio between target model and approximations shown in (a).

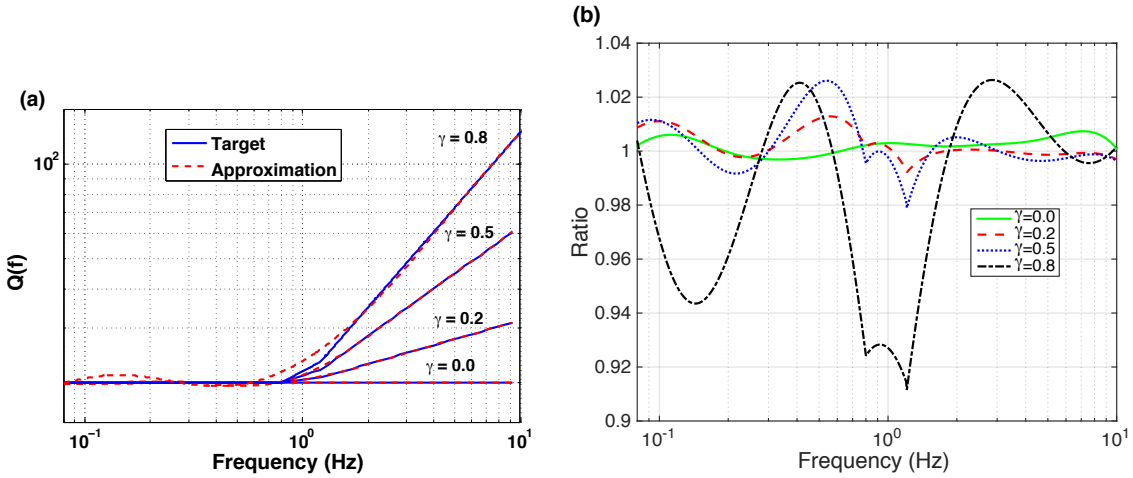

Figure 2.2: (a) Comparison of fits obtained between model Q (dashed line) and target Q (solid line) for several values of γ in equation 2 using the interpolation coefficients in equation (15) for effective Q in equation (12) at an example value of $Q = 20$. (b) Ratio between target model and approximations shown in (a).

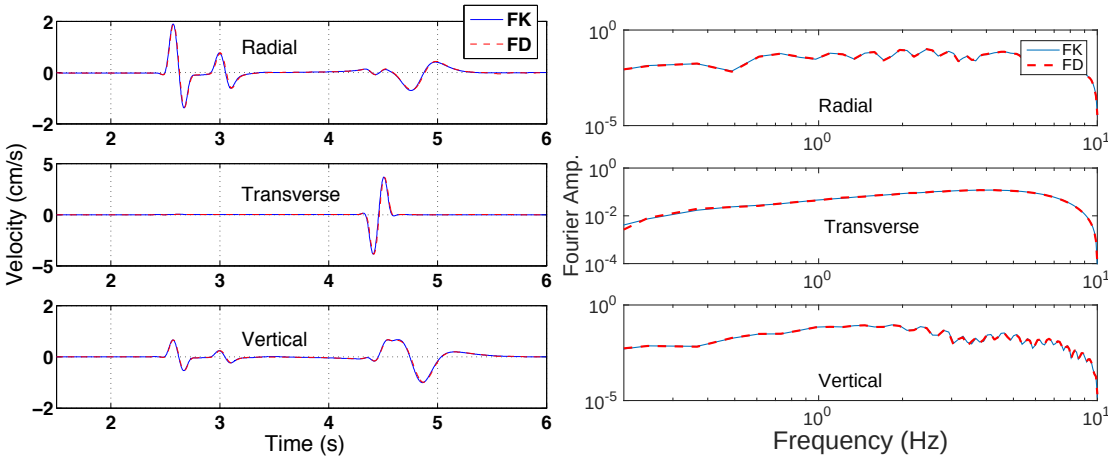

Figure 2.3: Half-space point source test: Comparison of FK and FD results for an elastic medium.

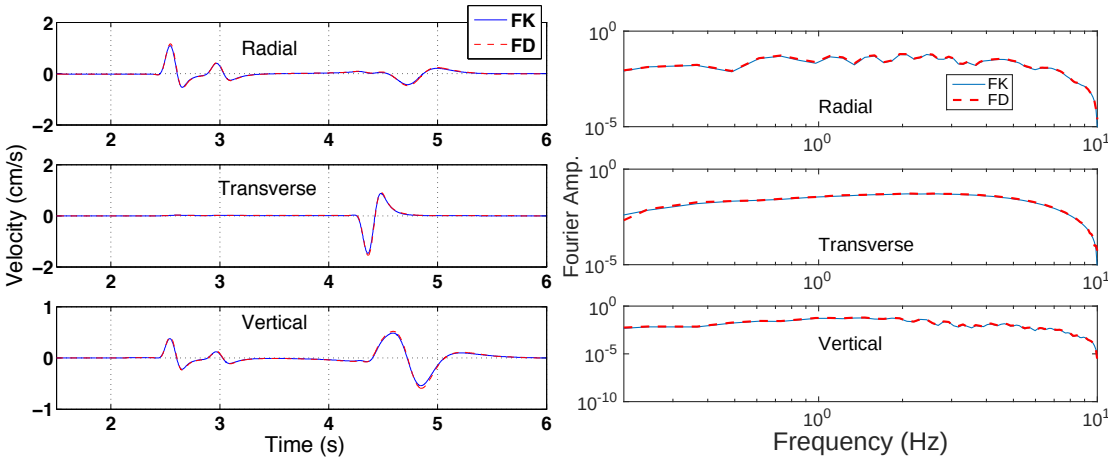

Figure 2.4: Half-space point source Test: Comparison of FK and FD results for a constant Q model with $\gamma = 0.0$.

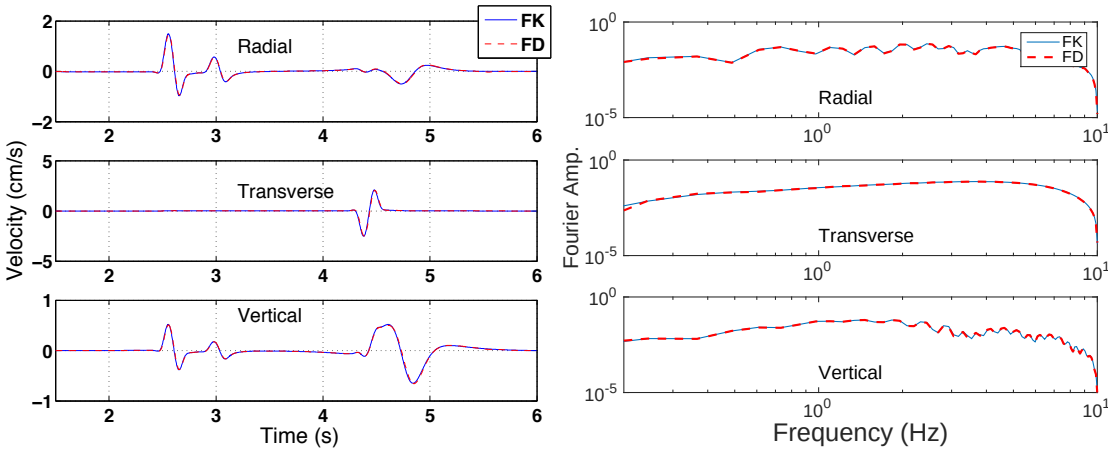

Figure 2.5: Half-space point source test: Comparison of FK and FD results for a Q(f) model where $\gamma = 0.6$.

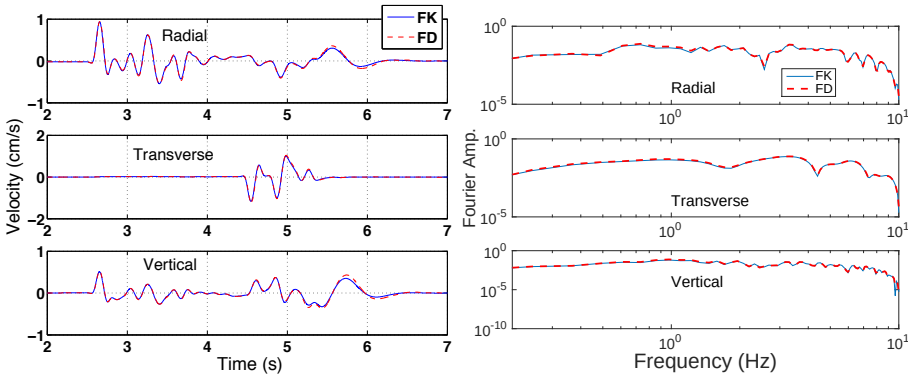

Figure 2.6: Layered-model point source test: Comparison of FK and FD results for a Q(f) model with $\gamma = 0.6$.

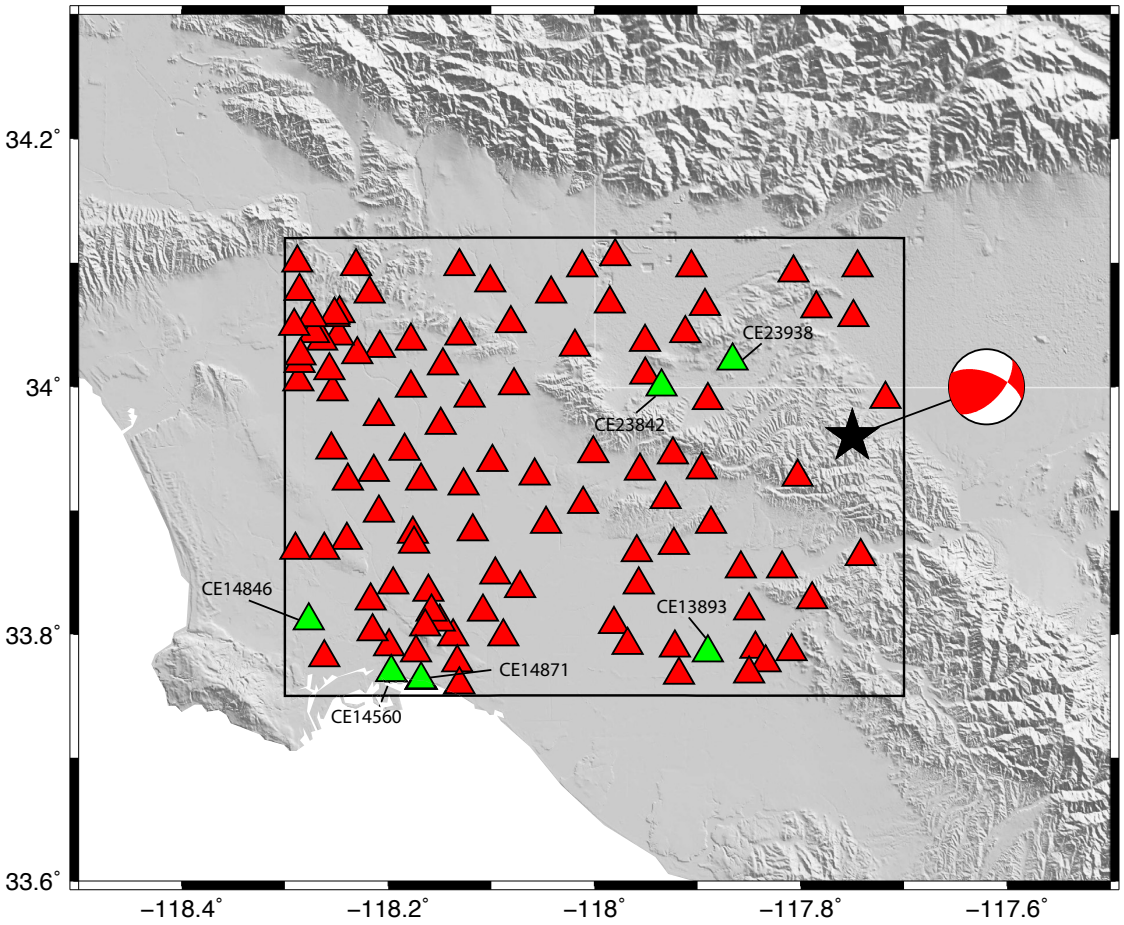

Figure 2.7: Simulated region of the Chino Hills event (rectangle) and location of 110 strong ground motion stations with 6 stations highlighted that are plotted in Figure 2.8. The star depicts the epicenter for the Chino Hills source.

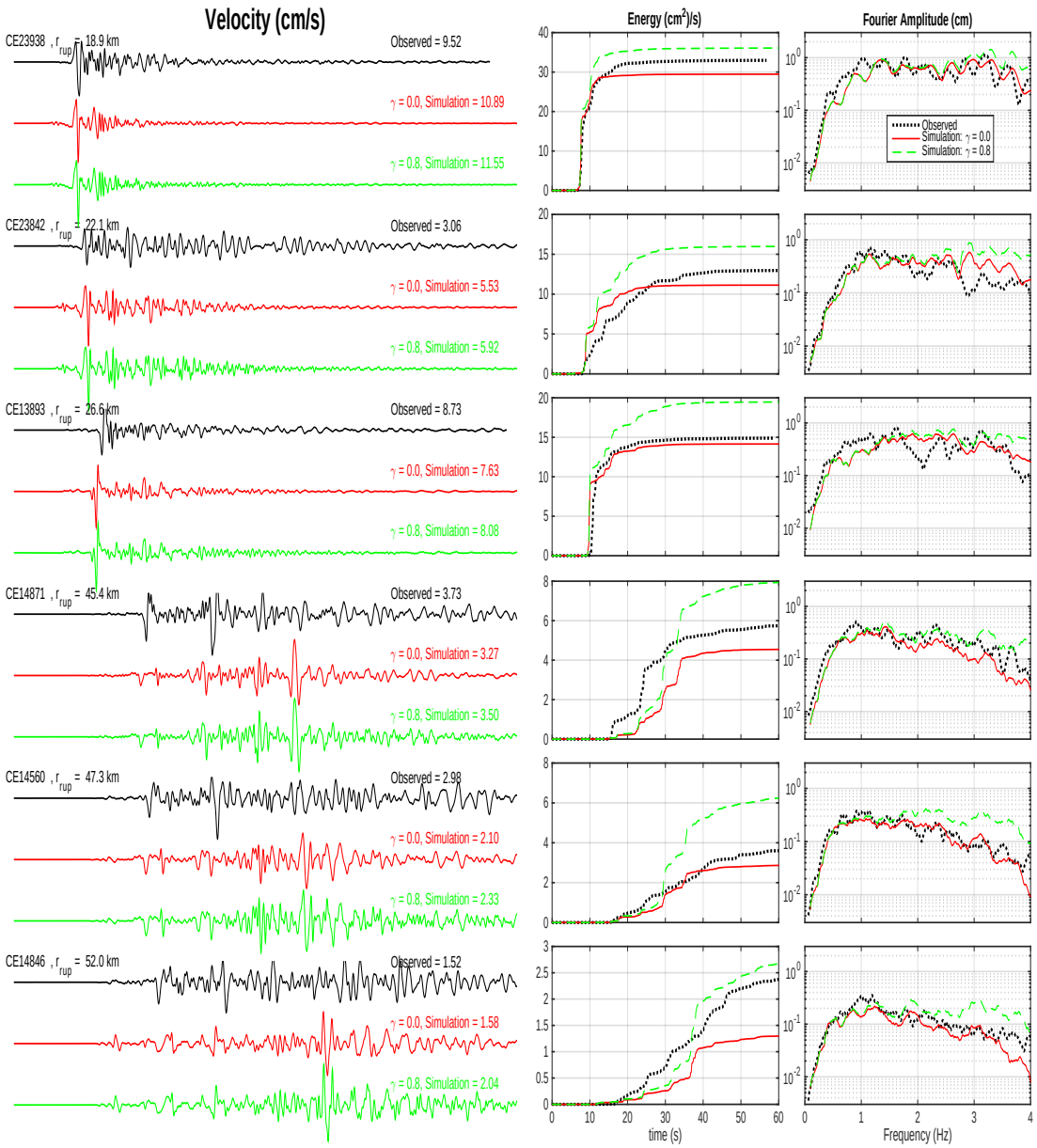

Figure 2.8: Comparison between data and synthetic velocity time-series, energy (normalized by density), and Fourier amplitude spectra for the east-west component of motion at stations ordered with increasing distance to the fault. The labels to the left show the station's network name, distance to the epicenter while the right labels show the peak ground velocity. The seismograms are bandpassed from $0.1 - 4$ Hz while the energy plots are bandpassed from $1.0 - 4.0$ Hz.

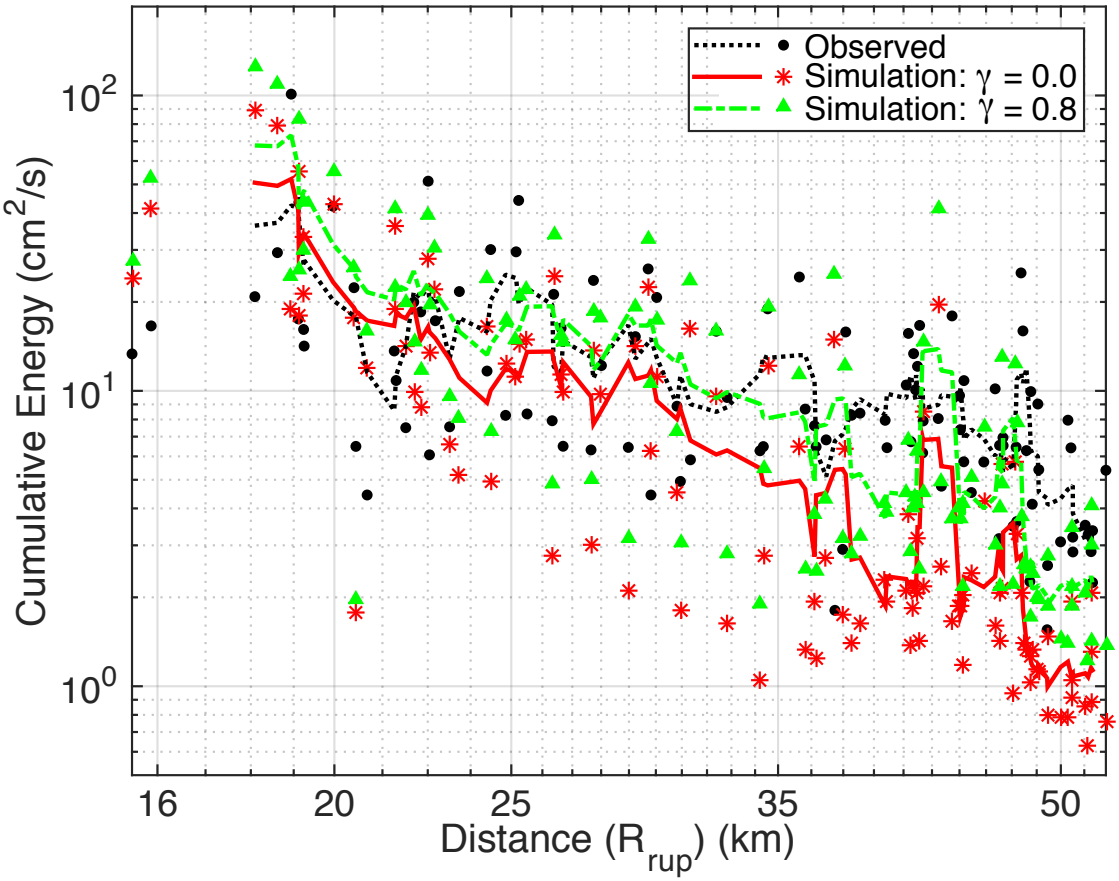

Figure 2.9: Cumulative energy as a function of distance to the fault for time series band-passed between 1.0 and 4.0 Hz using the strong ground motion stations in Figure 2.7. Dots depict values for individual stations and lines depict a 5-point moving average. R_{rup} indicates the closest distance to the ruptured surface of the fault plane.

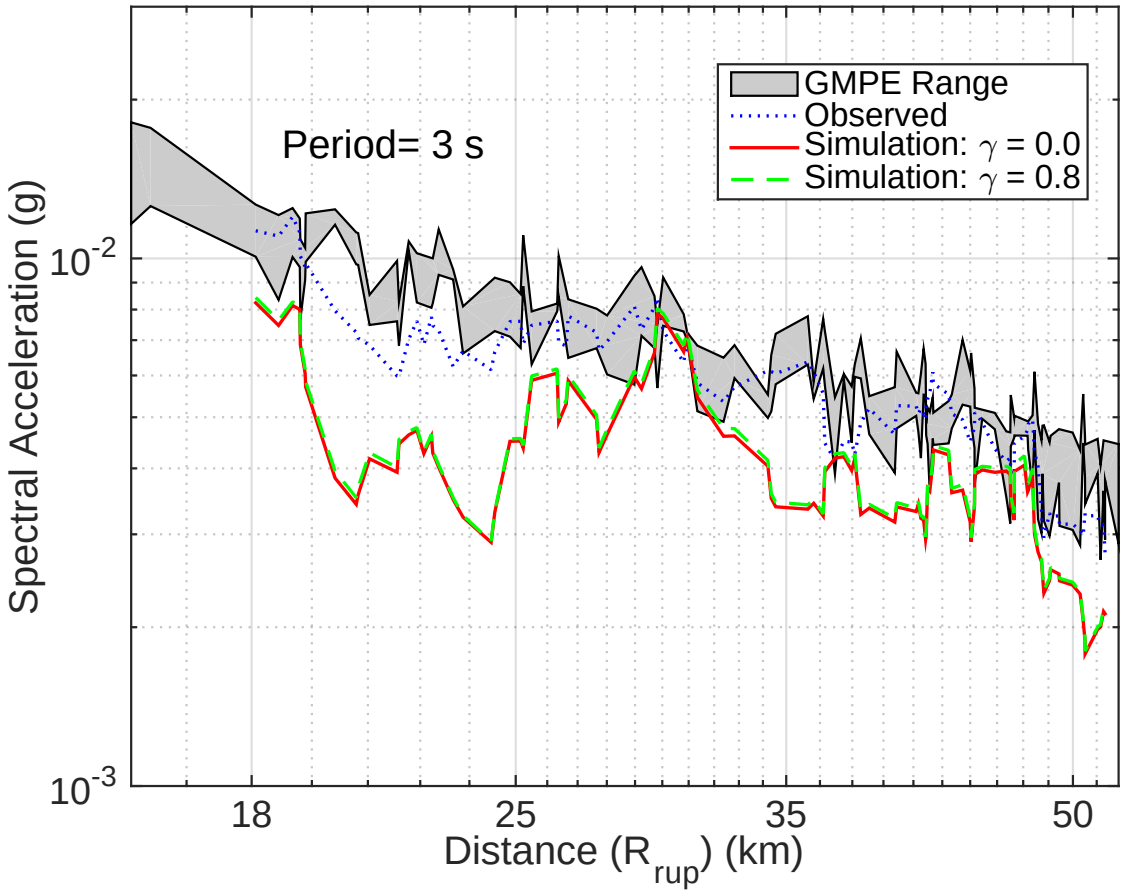

Figure 2.10: Median spectral acceleration as a function of distance centered at 3 s using the strong ground motion stations in Figure 2.7 as compared to the range of several GMPE predictions. A 5-point moving average was used for both synthetics and data for the strong ground motion station locations. R_{rup} indicates the closest distance to the ruptured surface of the fault plane.

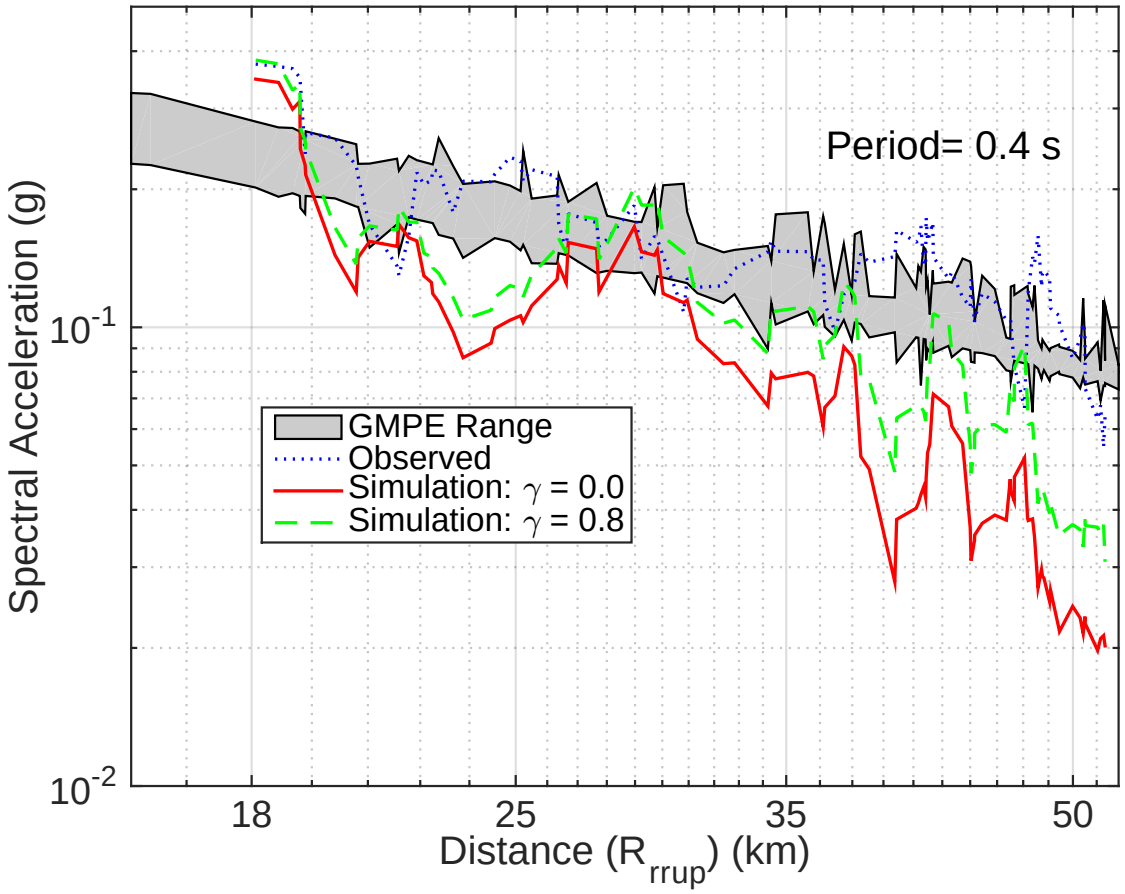

Figure 2.11: Similar to Figure 2.10, but here at 0.4 s.

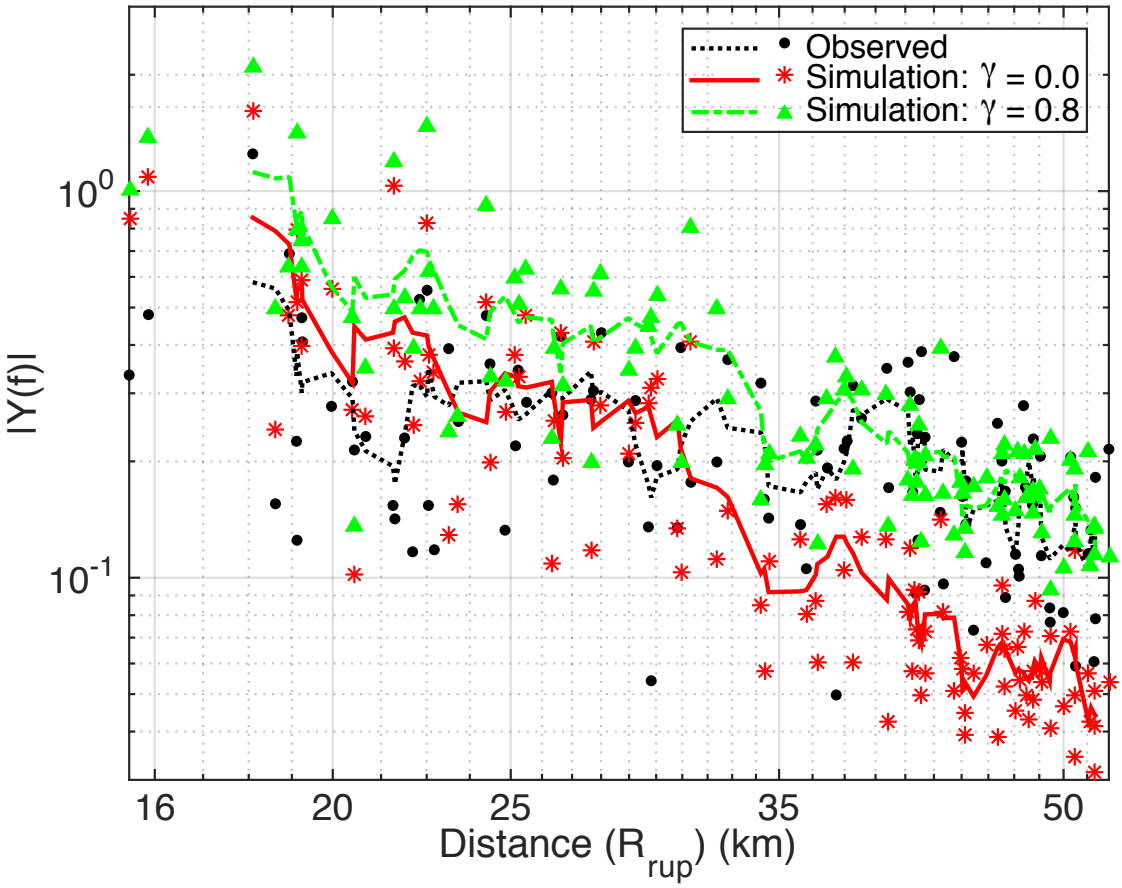

Figure 2.12: Fourier amplitude as a function of distance centered at 3.5 Hz using the strong ground motion stations in Figure 2.7. Dots depict values for individual stations and lines depict a 5-point moving average. R_{rup} indicates the closest distance to the ruptured surface of the fault plane.

Table 2.1: Relaxation times and weight coefficients for a range of power law exponents*.

γ	0.0	0.1	0.2	0.3	0.4	0.5	0.6	0.7	0.8	0.9
τ_m	0.0032	0.0032	0.0032	0.0032	0.0032	0.0032	0.0032	0.0066	0.0066	0.0085
τ_M	15.9155	15.9155	15.9155	15.9155	15.9155	15.9155	15.9155	3.9789	3.9789	3.9789
w_1	0.8867	0.3273	0.001	0.001	0.001	0.2073	0.3112	0.1219	0.0462	0.001
w_2	0.8323	0.8478	0.804	0.6143	0.4639	0.1872	0.001	0.001	0.001	0.001
w_3	0.5615	0.369	0.2005	0.0918	0.001	0.001	0.001	0.001	0.001	0.001
w_4	0.811	0.9393	1.0407	1.1003	1.1275	1.081	1.0117	0.2999	0.1585	0.1935
w_5	0.4641	0.4474	0.4452	0.4659	0.509	0.6016	0.7123	1.3635	1.4986	1.5297
w_6	1.044	1.0434	1.0349	1.0135	0.9782	0.912	0.8339	0.001	0.001	0.001
w_7	0.0423	0.044	0.0497	0.0621	0.082	0.1186	0.1616	0.5084	0.4157	0.1342
w_8	1.7275	1.7268	1.7245	1.7198	1.7122	1.6984	1.6821	1.2197	1.3005	1.5755

*Power laws using γ as in equation 2 with $Q_0 = 1$. These weights can scale to any $Q > 20$ with accuracy within 5%. The minimum relaxation time, τ_m, was adjusted for higher values of γ to optimize the fits. Here, $w_k = N\lambda_k$, where $N = 8$.

Table 2.2: Relaxation times and weight coefficients for a range of power law exponents.

γ	0.0	0.1	0.2	0.3	0.4	0.5	0.6	0.7	0.8	0.9
a_1	-27.5	7.37	31.8	43.7	41.6	20.0	8.08	1.99	5.16	-0.811
a_2	-34.1	-37.6	-42.0	-43.4	-41.1	-23.07	-13.0	-2.7	-8.2	0
a_3	-1.62	13.1	25.7	34.3	38.0	31.4	25.4	0	0	0
a_4	-27.7	-36.1	-40.8	-41.4	-43.2	-25.1	-10.4	41.3	58.9	56.03
a_5	14.6	12.3	7.02	-2.87	5.63	-45.2	-75.9	-88.8	-108.6	-116.9
a_6	-52.2	-51.4	-49.2	-45.3	-73.0	-27.8	-13.2	0	15.02	22.0
a_7	72.0	69.0	65.4	60.9	103.0	45.9	35.7	40.7	-5.88	0.03
a_8	-82.8	-83.1	-83.2	-83.1	-164.	-81.6	-79.9	-76.6	-46.5	-61.9
b_1	7.41	4.165	1.612	-0.1091	-0.734	-0.435	-0.196	0.418	0.212	0.162
b_2	6.02	5.52	5.08	4.58	3.82	2.67	1.81	0.59	0.345	0
b_3	4.68	3.47	2.28	1.19	0.393	-0.0434	-0.394	0	0	0
b_4	6.28	7.210	7.931	8.39	8.67	8.245	7.657	2.18	0.813	0.797
b_5	3.88	3.61	3.46	3.53	3.32	4.847	6.17	11.0	12.4	13.02
b_6	8.17	8.193	8.15	8.02	8.58	7.19	6.36	0	-0.283	-0.402
b_7	0.529	0.498	0.511	0.592	-0.419	1.15	1.68	1.95	1.42	-0.0006
b_8	13.19	13.13	13.07	13.0	14.9	12.8	12.7	11.3	11.7	12.5

Table 2.3: Media parameters defined in layered model.

v_p (m/s)	v_s (m/s)	Density (kg/m^3)	Q_{p0}	Q_{s0}	γ	Thickness (m)
5196	3000	2550	20	20	0.6	1000
6000	3464	2700	210	210	0.6	-

2.11 Appendix

2.11.A Additional Figures

Here we include additional figures showing an elastic layered-model point-source test comparison between the frequency-wavenumber (f-k) and finite difference (FD) results. In addition, we plot median spectral acceleration centered at 1 s and Fourier amplitude centered at 0.25 and 2.25 Hz as a function of distance using the strong ground motion stations in Figure 2.7.

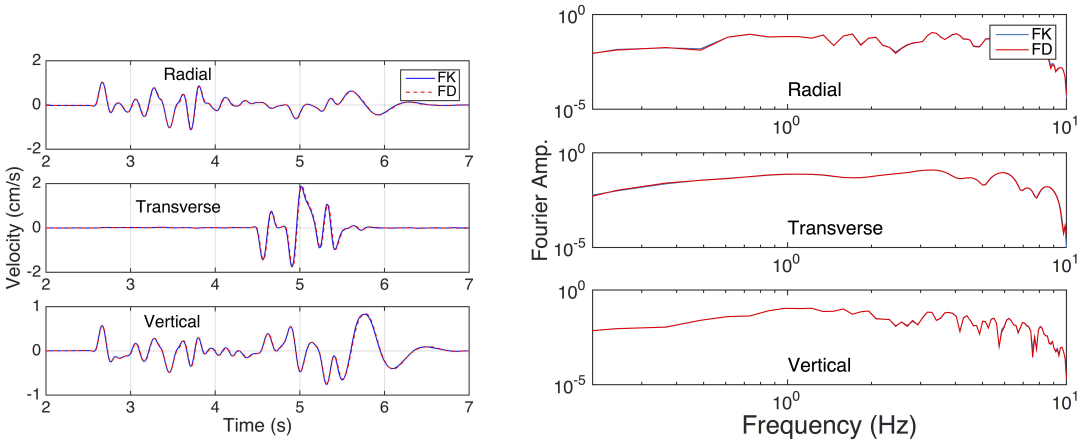

Figure 2.A.1: Layered-model point-source test: comparison of (f-k) and FD results for an elastic model for (left) velocity and (right) Fourier amplitude.

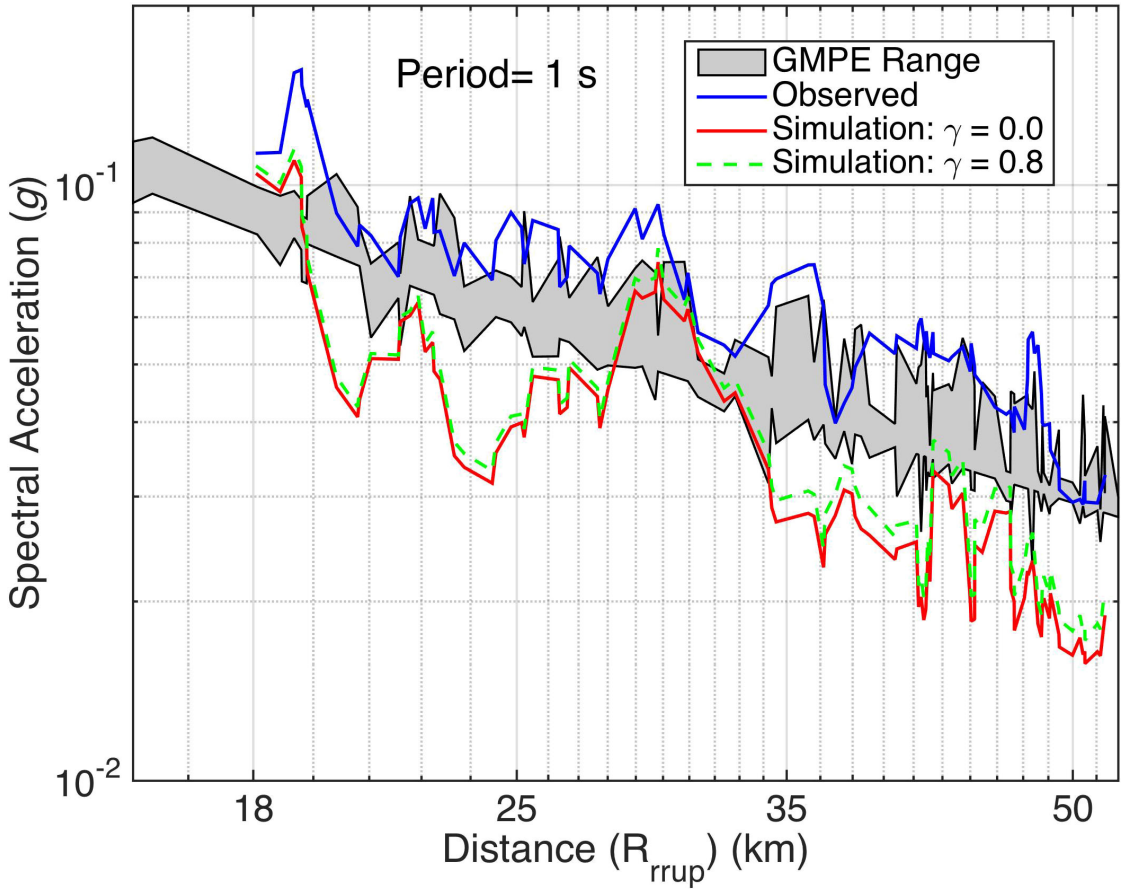

Figure 2.A.2: Median spectral acceleration (in units of gravity) as a function of distance centered at 1 s, using the strong ground motion stations in Figure 2.7 as compared to the range of several ground-motion prediction equation (GMPE) predictions. A five-point moving average was used for both synthetics and data for the strong ground motion station locations. R_{rup} indicates the closest distance to the ruptured surface of the fault plane.

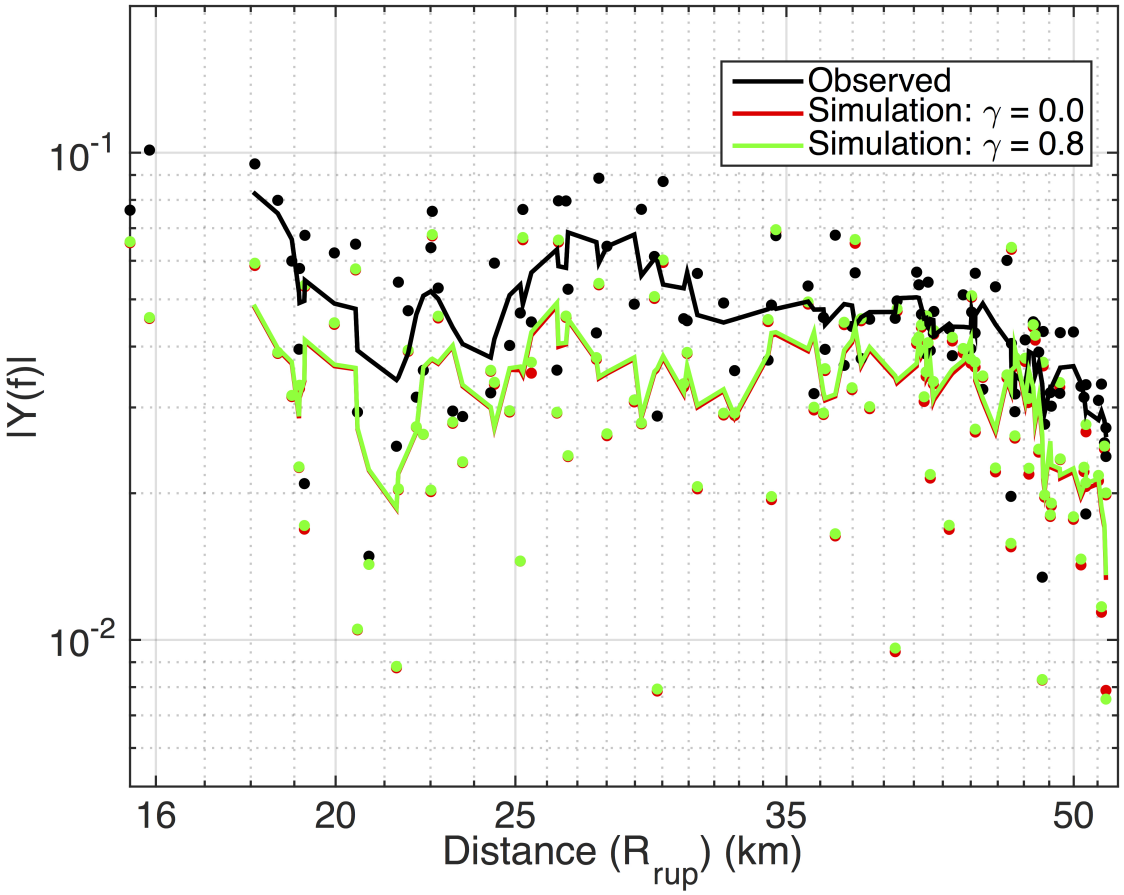

Figure 2.A.3: Fourier amplitude as a function of distance centered at 0.25 Hz, using the strong ground motion stations in Figure 2.7. Dots depict values for individual stations, and lines depict a five-point moving average. R_{rup} indicates the closest distance to the ruptured surface of the fault plane.

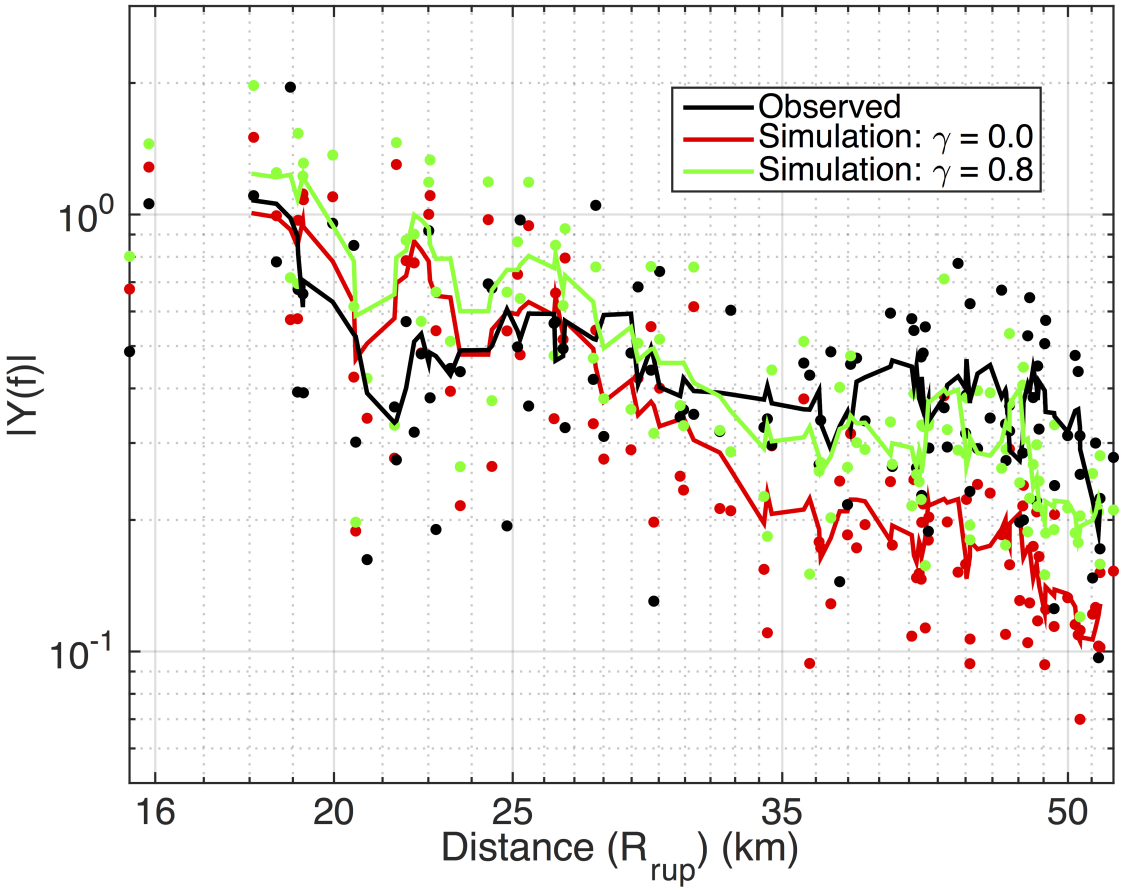

Figure 2.A.4: Fourier amplitude as a function of distance centered at 2.25 Hz using the strong ground motion stations in Figure 2.7. Dots depict values for individual stations, and lines depict a five-point moving average. R_{rup} indicates the closest distance to the ruptured surface of the fault plane.

2.12 References

References

Anderson, J. and S. Hough (1984). A model for the shape of the Fourier amplitude spectrum of acceleration at high frequencies. *Bull. Seism. Soc. Am.*, **74**, 1969–1993.

Blanch, J., J. Robertsson, and W. Symes (1995). Modeling of a Constant Q : Methodology and Algorithm for an Efficient and Optimally Inexpensive Viscoelastic Technique. *Geophysics*, **60**, 176–184.

Boore, D. M., J. Watson-Lamprey, and G.M. Atkinson (2008). Orientation-independent measures of ground motion. *Bull. Seismol. Soc. Am.*, **96**, 1502–1511.

Boore, D. M. and G.M. Atkinson (2008). Ground-motion prediction equations for the average horizontal component of PGA, PGV, and 5%- damped PSA at spectral periods between 0.01 s and 10.0 s. *Earthquake Spectra*, **24**, 99–138.

Campbell, K.W. and Y. Bozorgnia (2008). NGA ground motion model for the geometric mean horizontal component of PGA, PGV, PGD and 5% damped linear elastic response spectra for periods ranging from 0.01 to 10 s. *Earthquake Spectra*, **24**, 139–171.

Chiou, B. and R. Youngs (2008). An NGA model for the average horizontal component of peak ground motion and response spectra. *Earthquake Spectra*, **24**, 173–215.

Cui, Y., K. Olsen, T. Jordan, K. Lee, J. Zhou, P. Small, D. Roten, G. Ely, D. Panda, A. Chourasia, J. Levesque, S. Day, and P. Maechling (2010). Scalable earthquake simulation on petascale supercomputers. In *Procs. Supercomputing Conference*, November. New Orleans.

Day, S. and C. Bradley (2001). Memory-efficient simulation of anelastic wave propagation. *Bull. Seism. Soc. Am.*, **91**, 520–531.

Day, S. and J. Minster (1984). Numerical simulation of attenuated wavefields using a Pade approximant method. *Geophys. J. R. Astr. Soc*, **78**, 105–118.

Day, S. M. (1998). Efficient simulation of constant Q using coarse-grained memory variables. *Bull. Seism. Soc. Am.*, **88**, 1051–1062.

Dunham, E. M., D. Belanger, L. Cong, and J. E. Kozdon (2011). Earthquake Ruptures with Strongly Rate-Weakening Friction and Off-Fault Plasticity, Part 2: Nonplanar Faults. *Bull. Seism. Soc. Am.*, **101**, 2308–2322. ISSN 0037-1106.

Emmerich, H. and M. Korn (1987). Incorporation of attenuation into time-domain computations of seismic wave fields. *Geophysics*, **52**, 1252–1264.

Erickson, D., D. McNamara, and H. Benz (2004). Frequency-dependent Lg Q within the continental United States. *Bull. Seism. Soc. Am.*, **94**, 1630–1643.

Fitchner, A. and M. van Driel (2014). Models and Frechet kernels for frequency-(in)dependent Q. *Geophys. J. Int.*, **198**, 1878-1889.

Gottschämmer, E. and K. Olsen (2001). Accuracy of the Explicit Planar Free-Surface Boundary Condition Implemented in a Fourth-Order Staggered-Grid Velocity-Stress Finite-Difference Scheme. *Bull. Seism. Soc. Am.*, **91**, 617–623.

Graves, R. and S. Day (2003). Stability and accuracy analysis of coarse-grain viscoelastic simulations. *Bull. Seism. Soc. Am.*, **93**, 283–300.

Graves, R. W. and B. T. Aagaard (2011). Testing Long-Period Ground-Motion Simulations of Scenario Earthquakes Using the Mw 7.2 El Mayor-Cucapah Mainshock: Evaluation of Finite-Fault Rupture Characterization and 3D Seismic Velocity Models. *Bull. Seism. Soc. Am.*, **101**, 895–907. ISSN 0037-1106.

Kohler, M., H. Magistrale, and R. Clayton (2003). Mantle Heterogeneities and the SCEC Reference Three-Dimensional Seismic Velocity Model Version 3. *Bull. Seism. Soc. Am.*, **93**, 757–774.

Komatitsch, D., Q. Liu, and J. Tromp (2004). Simulations of ground motion in the Los Angeles basin based upon the spectral-element method. *Bull. Seism. Soc. Am.*, **94**, 187–206.

Kristek, J. and P. Moczo (2003). Seismic-Wave Propagation in Viscoelastic Media with Material Discontinuities: A 3D Fourth-Order Staggered-Grid Finite-Difference Modeling. *Bull. Seism. Soc. Am.*, **93**, 2273–2280.

Lee, E. and P. Chen (2014). Full-3-D tomography for crustal structure in Southern California based on the scattering-integral and the adjoint-wavefield methods. *J. Geophys. Res. Solid Earth*, **119**, 1–31.

Lindley, G. and R. Archuleta (1992). Earthquake Source Parameters and the Frequency Dependence of Attenuation at Coalinga , Mammoth Lakes , and the Santa Cruz Mountains , California. *J. Geophys.*, **97**, 14137–14154.

Liu, H., D. Anderson, and H. Kanamori (1976). Velocity dispersion due to anelasticity; implications for seismology and mantle composition. *Geophys. J. Int.*, **47**, 41–58.

Liu, P. and R. Archuleta(2006). Efficient Modeling of Q for 3D Numerical Simulation of Wave Propagation. *Bull. Seism. Soc. Am.*, **96**, 1352–1358. ISSN 0037-1106.

Ma, S. and P. Liu (2006). Modeling of the Perfectly Matched Layer Absorbing Boundaries and Intrinsic Attenuation in Explicit Finite-Element Methods. *Bull. Seism. Soc. Am.*, **96**, 1779–1794. ISSN 0037-1106.

Magistrale, H., S. Day, R. Clayton, and R. Graves (2000). The SCEC Southern California Reference Three-Dimensional Seismic Velocity Model Version 2. *Bull. Seism. Soc. Am.*, pages 65–76.

McNamara, D., M. Meremonte, J. Z. Maharrey, S.-L. Mildore, J. R. Altidore, D. Anglade, S. E. Hough, D. Given, H. Benz, L. Gee, and A. Frankel (2012). Frequency-Dependent Seismic Attenuation within the Hispaniola Island Region of the Caribbean Sea. *Bull. Seism. Soc. Am.*, **102**, 773–782. ISSN 0037-1106.

Moczo, P. (2005). On the rheological models used for time-domain methods of seismic wave propagation. *Geophys. Res. Lett.*, **32**, 1–5. ISSN 0094-8276.

Olsen, K., R. Nigbor, and T. Konno (2000). 3D viscoelastic wave propagation in the Upper Borrego Valley, California, constrained by borehole and surface data. *Bull. Seism. Soc. Am.*, **90**, 134–150.

Phillips, W. S., K. M. Mayeda, and L. Malagnini (2013). How to Invert Multi-Band, Regional Phase Amplitudes for 2-D Attenuation and Source Parameters: Tests Using the USArray. *Pure and Applied Geophysics*, **171**, 469–484. ISSN 0033-4553.

Raoof, M., R. Herrmann, and L. Malagnini (1999). Attenuation and excitation of three-component ground motion in southern California. *Bull. Seism. Soc. Am.*, **89**, 888–902.

Savage, B., D. Komatitsch, and J. Tromp (2010). Effects of 3D Attenuation on Seismic Wave Amplitude and Phase Measurements. *Bull. Seism. Soc. Am.*, **100**, 1241–1251. ISSN 0037-1106.

Savran, W. H. and K. B. Olsen (2014). Validation Exercise for Two Southern California Earthquakes. In *Procs. 2014 SCEC Annual Meeting, Poster #65*. Palm Springs, Sept. 7-10.

Shao, G., C. Ji, and E. Hauksson (2012). Rupture process and energy budget of the 29 July 2008 Mw 5.4 Chino Hills, California, earthquake. *J. Geophys.*, **117**, 1–12. ISSN 0148-0227.

Shi, Z. and S. M. Day (2013). Rupture dynamics and ground motion from 3-D rough-fault simulations. *J. Geophys.: Solid Earth*, **118**, 1122–1141. ISSN 21699313.

Kristekova, M., J. Kristek, and P. Moczo (2009). Time-frequency misfit and goodness-of-fit criteria for quantitative comparison of time signals. *Geophys. J. Int.*, **178**, 813-825.

Song, X. and T. H. Jordan (2013). Anelastic Attenuation and Elastic Scattering of Seismic Waves in the Los Angeles Region. In *American Geophysical Union Annual Meeting*. San Francisco, Dec 9-13, poster # S32B-05.

Taborda, R. and J. Bielak (2014). Ground-Motion Simulation and Validation of the 2008 Chino Hills, California, Earthquake Using Different Velocity Models. *Bull. Seism. Soc. Am.*, **104**, 1876–1898. ISSN 0037-1106.

Tape, C., Q. Liu, A. Maggi, and J. Tromp (2010). Seismic tomography of the southern California crust based on spectral-element and adjoint methods. *Geophys. J. Int.*, **180**, 433–462. ISSN 0956540X.

van Driel, M. and T. Nissen-Meyer (2014). Optimized viscoelastic wave propagation for weakly dissipative media. *Geophys. J. Int.*, **199**, 1078–1093. ISSN 0956-540X.

Xie, X.-B. (2005). Investigating Explosion Source Energy Partitioning and Lg-Wave Excitation Using a Finite-Difference plus Slowness Analysis Method. *Bull. Seism. Soc. Am.*, **95**, 2412–2427. ISSN 0037-1106.

Lekic, V., J. Matas,M. Panning, and B. Romanowicz (2009). Measurement and implications of frequency dependence of attenuation. *Earth Planet. Sci. Lett*, **282**, 285-293.

Xu, T. and G. McMechan (1998). Efficient 3-D viscoelastic modeling with application to near-surface land seismic data. *Geophysics*, **63**, 601–612.

Zhu, L. and L. Rivera (2002). A note on the dynamic and static displacements from a point source in multilayered media. *Geophys. J. Int.*, **148**, 619–627. ISSN 0956540X.

Chapter 3

Ground Motion and Intraevent Variability from 3-D Deterministic Broadband (0-7.5 Hz) Simulations along a Non-planar Strike-slip Fault

3.1 Abstract

We model deterministic broadband (0-7.5 Hz) ground motion from a M_w 7.12 strike-slip event with rough-fault topography. The synthetic ground motion is compared with that of ground motion prediction equations (GMPEs) as well as a broadband hybrid technique up to 60 km from the source. We run our simulations in varying media, progressively increasing the complexity: from a 1D-layered model to a 3D velocity model extracted from the Southern California Earthquake Center (SCEC) Community Velocity Model (CVM) including a geotechnical layer. We include frequency-dependent attenuation as a power-law above a transition frequency, and include small-scale medium heterogeneity using a range of statistical parameters. We find that for this bilateral rupture, spectral acceleration at various

periods and Arias Intensity duration lie within 1-2 interevent standard deviations above the median, with a spectral decay with distance that closely matches that of GMPEs when using a Q(f) power-law exponent between $0.6-0.8$ above 1 Hz. Scattering from small-scale heterogeneity in the medium tends to increase the median ground motion for this extended-fault rupture, but it can also serve to reduce it through scattering attenuation. The ground motion variability is strongly affected by the addition of media heterogeneity, serving to reduce otherwise large values of intraevent standard deviation to nearer that of empirical observations. We find that a 3D background velocity model influences directivity compared to a layered model, reducing the pulse period into the expected period range. Finally, we estimate κ and introduce an approach to control the high-frequency decay in energy that may be necessary as simulations continue to extend to higher frequencies.

3.2 Introduction

The strong shaking created by large magnitude earthquakes is of principal interest to structural engineers to determine the ground motion that buildings and other structures must be able to endure. Typically, a structure's response is designed to withstand a peak motion described by some metric, such as peak ground acceleration (PGA) or spectral acceleration (PSA) at a certain frequency. Ground motion prediction equations (GMPEs) seek to predict this motion by using empirical observations of events. Along with a median value for the ground motion, there is also an uncertainty associated with the GMPEs prediction; this is limited by the finite number of observations, and is currently set to be constant as a function of distance in most implementations, but varies as a function of period. At moment magnitudes > 6, there is a shortage of observations at distances close to the source (< 200 km). Thus, characteristics from empirical simulations have been used to supplement the database. This has been done successfully at low frequencies (< 1 Hz) for many years, but only recently has there been the computational ability to simulate 3D high-frequency earthquake ground motion at significant distances from the source. Small structures typically have a resonant frequency larger than

1 Hz. Thus, it is extremely important to extend earthquake ground motion prediction to higher frequencies, to determine the seismic hazard associated with these structures.

Deterministic simulations allow one to generate synthetic ground motion of both historical and hypothetical events and to perform analysis of the resulting ground motion using a user-defined station distribution. Broadband hybrid techniques have been developed by utilizing the low-frequency deterministic ground motion and combining with that of stochastically generated high-frequency components. These techniques, however, lack deterministic information that may be important in predicting strong ground motion. A recent push has been made to extend deterministic simulations to higher frequencies, using purely physics-based simulations (Taborda et al., 2016). To model these high-frequency synthetics accurately, the fault and the medium need to be modeled realistically. This includes ensuring that the source has energy content comparable to observations and implementing complex velocity structure that matches borehole studies in a statistical sense. Additionally, anelastic attenuation (energy losses due to heat and other causes) can dramatically affect the ground motions. Previous studies have been mostly limited to attenuation being constant across the bandwidth; a more realistic representation of the earth is to model attenuation as a varying function of frequency. Here, we extend 3D deterministic simulations to higher frequencies using a source that has energy consistent with that of data. We model broadband (0-7.5 Hz) ground motion of a generic strike-slip fault with rough fault topography for distances up to 60 km from the source and compare with that of GMPEs. We include frequency-dependent attenuation via a power law above a reference frequency and superimpose small-scale heterogeneity on both 1D and 3D background velocity models. The purpose is to determine if realistic ground motion is obtained compared with empirical observations (examining both the median and standard deviation of ground motion), and to investigate the effects of anelastic attenuation and scattering at high frequencies ($>$ 1 Hz) with a finite source and duration. We also compare our deterministic synthetics with that generated from a hybrid broadband approach derived from the low-frequency synthetics. Additionally, we

examine κ, the decay in high-frequency energy, as a function of distance, and introduce a shallow constant-Q zone in the top 3 km that serves to simulate the site-component of κ.

3.3 Background

3D wave propagation simulations of ground motions are already playing a role in assessment of seismic hazard and risk through prediction of ground motion for scenario earthquakes. Additionally, they are useful for planning of earthquake emergency response and public earthquake preparedness exercises, physics-based seismic hazard assessment (Graves et al., 2010), as well as complementing ground motion prediction equations in regions of poor sampling, as in Day et al. (2008), where simulated basin responses were used in the Next Generation Attenuation (NGA) project. The frequency range of engineering interest extends up to at least 10 Hz. The ability to extend deterministic ground motion predictions to higher frequencies and predict PGA and PSA is invaluable for structural engineers, as there is only a finite amount of empirical data from prior earthquakes to determine future seismic hazard.

3.3.1 Hybrid Deterministic-stochastic Broadband Approach

Ground motion time series are needed as input for more realistic nonlinear structural dynamic analysis of building and performance based earthquake engineering. Realistic ground motion synthetics may help to verify or even improve GMPEs and reliably extend them into the distance range where only few recordings exist, such as in the near field of large earthquakes. Because of the prohibitive cost of fully-deterministic broadband simulations, in recent years hybrid methodologies have been incorporated, combining a deterministic approach at low frequencies ($f < 1$ Hz) with a stochastic approach at high frequencies ($f > 1$ Hz). There are several techniques in use today; (e.g., Olsen and Takedatsu, 2015; Anderson, 2015; Graves and Pitarka, 2015; Atkinson and Assatourians, 2012; Crempien and

Archuleta, 2015). An example is BBtoolbox (Olsen and Takedatsu, 2015), derived from Mena et al. (2010), who extended the approach from Mai et al. (2010) to include large-magnitude effects by incorporating dynamically consistent source-time functions and accounting for finite-fault effects in the computation of the high-frequency (HF) waveforms. The (HF) accelerograms are generated for each component of motion based on the theory for multiple S-to-S backscattering (Zeng et al., 1993). The Fourier amplitude of the scattergram is then combined with the Fourier amplitude of the low-frequency synthetic. BBtoolbox matches the amplitude and phase spectra at a target intersection frequency, typically near 1 Hz. One drawback of hybrid techniques is that the purely stochastic methods (at least for the HF) involve little physics in terms of parameterizing the earthquake rupture and details of wave propagation. The result is that stations are completely uncorrelated even for close neighboring stations.

3.3.2 Rough Fault Topography

Faults are observed to have roughness at all scales, ranging from the map-scale (such as branching and segmentation, e.g. Ben-Zion and Sammis, 2003) to the finer scale with topographic complexity on the fault slip surfaces (e.g. Power and Tullis, 1991; Renard et al., 2006). This has been modeled by a self-similar fault-surface in deterministic simulations (Dunham et al., 2011) with a single power law. The synthetic ground motions have been shown to match the characteristics of real data, having a flat power spectrum up to some cutoff frequency (Shi and Day, 2013). This is generated because of the complex motion of the rough fault as it propagates due to the complex stress field generated by the fault topography. As the earthquake rupture propagates along a non-planar surface it creates high-frequency radiation as the rupture fronts accelerate, decelerate, or lose coherence from interaction with geometrical irregularities. With this recent addition of realistic fault topography in 3D simulations of earthquake source models, ground motion can be deterministically generated more realistically at higher frequencies.

3.3.3 Frequency Dependent Attenuation

The earthquake source is not the only source of complexity in the high-frequency ground motion; anelastic attenuation is also important in the accurate simulation of seismic wave propagation. At higher frequencies, where there are more cycles per wavelength, it has an even greater effect on the ground motion. Most previous studies have implemented constant-Q across a bandwidth; however, observations have indicated that Q seems to fall off at higher frequencies (e.g., Raoof et al., 1999; Phillips et al., 2013). Recently, Withers et al. (2015) implemented this behavior in the form of a power-law above a transition frequency:

$$Q(f) = Q_0 \cdot (f/f_0)^{\gamma}, \tag{3.1}$$

where f_0 is a reference frequency with Q_0 and γ constants that can vary. They found that a power-law model with exponent of 0.8 above 1 Hz had significantly more energy up to 4 Hz, increasing with distance from the source, compared to a constant Q model.

3.3.4 Small-scale Heterogeneity

There are also scattering effects caused by small-scale velocity and density heterogeneities in the medium that can affect the ground motion intensity. State-of-the-art Community Velocity Models (CVMs), e.g., the Southern California Earthquake Center (SCEC) CVM version 4.0 and CVM-H, resolve velocity structure on the order of kilometers. However, to be able to resolve the ground motion at frequencies > 1 Hz requires resolution on a much smaller scale. Currently, it is not possible to capture the location-specific small-scale velocity variation in the medium at this scale-length from a large region; thus statistical methods are used to depict its variability.

Previous studies have investigated these statistical parameters in wave propagation simulations (e.g. Frankel and Clayton, 1986; Hartzell et al., 2010; Imperatori and Mai, 2013; Bydlon and Dunham, 2015). The power spectrum depends on the Hurst exponent, determining the spectral decay at high-wave numbers which

changes the roughness of the medium, as well as the correlation length and standard deviation. These studies determined the appropriate ranges of the Hurst exponent, ranging from 0.0 to 0.5, and analyzed the effect of different correlation lengths. Frankel and Clayton (1986) found that a Von Karman autocorrelation function best explained two features seen in seismic records: teleseismic travel-time anomalies and the high-frequency (> 30 Hz) content of the seismic coda in microearthquake waveforms. Weak ($\sim 5\%$) standard deviations in random fractal crustal velocity variations are required to explain observed body-wave travel-time variations and high frequency coda waves. Previous studies have performed an analysis on the statistical properties of these small-scale variations in well logs and tomography in Southern California (Nakata and Beroza, 2015; Savran and Olsen, 2016) and found parameters describing the medium assuming a Von Karman autocorrelation function, defined by the Fourier transform of the correlation function. These studies found results of a vertical correlation length up to 150 meters, a Hurst exponent near 0.0 (indicating that the medium is very rough and rich in short wavelength heterogeneities), between $5 - 10\%$ bounds on the standard deviation. Additionally, Nakata and Beroza (2015) and Shaw et al. (2014) estimate a horizontal to vertical anisotropic factor near the range of $5 - 10$ (i.e. ellipsoidal anisotropy).

3.4 Method

3.4.1 Rough Fault Topography

We include complexity from a non-planar fault within our deterministic simulations. A fault roughness model is generated in the wavenumber domain and is designed to follow a self-similar fractal distribution over a specified bandwidth from a vertical mean plane, here over three orders of magnitude from 80 m to the length of the fault (~ 80 km). Shi and Day (2013) studied the effects of fault roughness on rupture propagation and resultant ground motion from a generic right-lateral strike-slip model using the Support Operator Rupture Dynamics (SORD) code. They found that this source created realistic power spectra,

having a near-flat spectrum up to 10 Hz. Here we use a similarly described dynamic model of the source from a generic Mw 7.12 strike-slip earthquake, where the initial shear stresses are applied in a right-lateral strike-slip sense of motion and the simulation uses physics to deterministically model the slip rates. The simulation uses the same fault topography as in Shi and Day (2013), but uses a 1D-layered velocity model derived from an unweathered characteristic hard rock site in southern California with a minimum shear wave velocity of 863 m/s (Vs_{30} corresponding to Class B of the National Earthquake Hazards Reduction Program [NEHRP] boundary site conditions), and rapidly increases with depth. Figure 3.1 shows the topography along the rough fault, showing a strike-slip model composed of ~ 5 million subfaults as well as the 1D-layered velocity model used in the dynamic simulations.

The details of the simulation are similar to Shi and Day (2013), where a strongly rate-weakening friction law was imposed, and the bulk material is subject to Drucker-Prager viscoplasticity. Rupture nucleation is achieved by imposing a shear traction perturbation circle with a radius of 1 km. The inclusion of Drucker-Prager viscoelasticity allows the off-fault plastic strain to relax what would otherwise be unphysical high stress concentrations in the dynamic process around the rupture tip. The rupture progresses at a generally subshear rupture velocity and low-confining pressure at shallow depth allows for a small amount of shallow slip triggered by radiated stress waves from rupture fronts at depth.

As in Shi and Day (2013), inelastic strain deformation occurs near the free surface, induced by stress waves originating from the dynamic rupture at depth. The extent of non-negligible irreversible strain extends to fault-normal distances of up to 5-10 km from the fault, with the majority of plastic yielding induced by seismic energy arriving after the hypocentral S-phase. As noted in Shi and Day (2013), PGA measurements from simulations without plasticity in a homogenous medium are, on average, 50% larger than those from simulations with plasticity. It is likely that nonlinear effects would also cause a reduction in peak ground motion in the layered model run here, at similar distances from the fault.

3.4.2 Simulations Details

The seismic source in physics-based earthquake simulations can be specified using a kinematic or dynamic representation. In a dynamic source, only the friction properties and initial stresses are prescribed on the fault and the time history of fault slip evolves spontaneously as part of the elastodynamic solution of the rupture model. In the kinematic approach, the spatial and temporal evolution of slip (slip-velocity functions and rupture velocity) is prescribed a priori on each grid point along the fault (subfault). Here, we take the dynamic rupture slip rate time histories output from the spontaneous rupture simulation along the rough fault in SORD and convert them to moment-rate time histories and input as a kinematic source into AWP-ODC-GPU, a parallel wave-propagation program (Cui et al., 2013). This is a finite difference anelastic wave-propagation code that is highly scalable, allowing us to extend the ground motions to further distances from the fault, and retain high-frequency content. Specifically, the moment-rate tensor elements are $T_{ij}^n = s^n \mu A(n_i d_j^i + n_j d_i^j)$ where n and d are unit vectors oriented normal to the fault and along the slip direction, respectively and A is the fault surface area associated with the given discretization element (i.e., subfault). We assume that there is no fault opening component. As AWP requires a regularized grid, we choose the closest subfault of the rough fault corresponding to our regularized mesh, with a maximum error of one half grid spacing in the fault-perpendicular direction. This discretized fault model approximation starts to break down at higher frequencies, but still retains sufficient accuracy in the bandwidth of interest here (< 7.5 Hz). If this approach is used in the future at at higher frequencies, an interpolation algorithm could be used to improve accuracy, if necessary. Verification of the two-step procedure showing SORD and AWP seismograms and frequency spectra comparisons can be found in Appendix 3.11.A. It is found that the misfit for both the envelope and phase is less than 5% up to 10 Hz. We deem this as acceptable, as there are inherent differences between the second-order SORD and fourth-order AWP codes that likely reduce the accuracy, in addition to the approximations used here. For example, by using this procedure, we assume that anelastic attenuation along the fault has a negligible effect on the

dynamic propagation, and that scattering from small-scale heterogeneities in the medium have little effect on the rupture process. This second assumption is reasonable, as Bydlon and Dunham (2015) found that variations in slip and rupture velocity can arise from material heterogeneity alone, but are dominantly controlled by fault roughness, and scattering effects only become applicable beyond about 3 km from the fault. Thus, one can safely neglect random material heterogeneity when solving the rupture process. The cohesive zone is large enough throughout the entire model to accurately resolve the slip-rate along the fault, which controls the accuracy of the dynamic simulations (Day et al., 2005).

Both the dynamic and kinematic simulations are run in a laterally homogeneous model characteristic of a typical southern California rock-site profile. Our model domain extends up to 60 km from the fault in all directions for a size of 204 x 124 x 41 km, allowing analysis of full azimuthal coverage of r_{rup} (the closest distance to the fault plane) to 60 km, with a grid spacing of 20 m up to a maximum of 8 Hz for a minimum of 5-6 grid points per wavelength at the lowest shear wave velocity.

In addition, we used a 3D velocity model extracted from the CVM (Magistrale et al., 2000; Kohler et al., 2003) known as CVMSi 4.26, including a near-surface geotechnical layer (GTL), as an additional background velocity model in this study. Taborda and Bielak (2014) analyzed simulations of the 2008 Chino Hills earthquake with and without the appended information of soft sedimentary deposits, or GTL near the surface, and showed that better results are obtained with its inclusion when compared with data. This algorithm uses observed values of V_p, V_s ,and ρ in the GTL, replacing information in the upper 350 m with a velocity model derived from V_{s30} maps, and interpolated at depth to merge with the background CVM. In cases where we include 3D velocity structure, we clamp the minimum shear wave velocity to be 863 m/s, and then modified V_p such that the local V_p/V_s ratio is conserved. The kinematic simulation is embedded in the heterogeneous 3D structure, which modifies the total moment of the simulation (because of the altered shear modulus) by less than 3%. We input the mean fault plane along a 80 km section along the San Andreas Fault, located northeast of the

Los Angeles Basin (see Figure 3.2), and rotate our model domain to lie along the strike of the fault.

We compare the results from the deterministic simulations to those from the SDSU Broadband Hybrid technique, (Olsen and Takedatsu, 2015) or Broadband Ground-Motion Generation Module BBtoolbox Version 1.5, which takes into account an improved merging procedure for combining deterministic and stochastic synthetics. This hybrid method uses the low-frequency deterministic synthetics with high-frequency scatterograms to generate hybrid broadband time series up to 10 Hz or higher. P and S wave arrival times are calculated from the 1D and averaged source-receiver 3D media using a 3D raytracing method, downsampled to a spatial resolution of 1 km, using a $Q(f)$ exponent of 0.8 above 1 Hz, and κ_0 value of 0.04.

3.4.3 Frequency Dependent Attenuation

We run simulations including frequency dependent attenuation, with constant-Q up to a transition frequency f_T and following a power law formulation above this threshold:

$$Q(f) = \begin{cases} Q_0 & 0 < f < f_T \\ Q_0 \cdot (f/f_T)^{\gamma} & f > f_T \end{cases} D, \tag{3.2}$$

where Q is the quality factor, Q_0 is the low-frequency value of Q, and $0 \leq \gamma \leq 1$. A γ exponent of 0 simply reduces to that of a constant Q model. We relate the shear wave velocity to the Q values: $Q_{s0} = v_s * C$ and $Q_{p0} = 2 * Q_s$, where C is a constant ranging from $0.05 - 0.1$ and v_s is in m/s. In the hybrid simulations we used $Q_0 = 150.0$, equivalent to the deterministic simulation at $V_s = 3000$ m/s when $C = 0.05$.

3.4.4 Small-scale Heterogeneity

Scattering in earth's crust is known to affect seismic ground motion, including amplitudes, travel times and spectra. Imperatori and Mai (2013) demonstrated that scattering can increase ground motion complexity at a few kilometers away

from the source. To more accurately simulate the medium, we include self-similar small-scale heterogeneity within our models by using a Von Karman distribution, which statistically models the variation in velocity and density throughout the medium. Heterogeneous 3-D velocity models can be obtained by superimposing a spatially random field to a specific deterministic model as described in Imperatori and Mai (2013). Superimposed random perturbations are scaled at each depth level to maintain the relative standard deviation. We generate several statistical models, with a vertical correlation length ranging from $150 - 1000$ meters, keeping the Hurst exponent constant at 0.05, a value close to what is predicted for Southern California (Savran and Olsen, 2016). We introduce pattern anisotropy in the model by horizontal stretching of an isotropic distribution by a factor of 5. The fractal inhomogeneities are incorporated with standard deviations of 5 or 10 percent (the range estimated by Savran and Olsen, 2016, Nakata and Beroza, 2015, and Shaw et al., 2014) for several different choices of the random seed. Figure 3.3 gives an example of the surface heterogeneity of the shear wave velocity after superimposing a statistical fractal model on the 1D-layered velocity profile. In our simulations, we clamp the velocities that extend below 750 m/s, accounting for just a few node locations in the medium (and only at the surface) for 5% σ and slightly more at 10%.

Figure 3.4 plots the media variations of the shear-wave velocity including a geotechnical layer extracted from the CVM as well as a plot of small-scale heterogeneity superimposed on this 3D background model. This causes the longer wavelengths and geologic units formed by fault boundaries and contacts between other structural units to be retained, with statistical variability of the random media at shorter wavelengths. It is evident that the GTL layer greatly reduces the surface-wave velocity; to keep our simulations accurate at high-frequencies, we first clamp the background model before adding in small-scale heterogeneity, so that we do not bias our simulations with only positive variations of heterogeneity. We choose 863 m/s as the background minimum shear wave velocity, matching that of the 1D-layered models, which greatly reduces the CVM background complexity in the top 1-2 grid points within our models. We note that we applied the 3D hetero-

geneity throughout the entire medium when using perturbed velocity models, even along the fault itself. Some authors include a homogenous region surrounding the fault; in either case, the effect should be small when dealing with several million fault elements, as we are here.

Appendix 3.11.B investigates the accuracy of 3D simulations when introducing fine-scale variations in the media by comparing AWP with a semi-analytical technique (f-k) (Zhu and Rivera, 2002) and a summation by parts approach (Sjögreen and Petersson, 2012) for purely elastic models. It is found that a high level of accuracy is still achieved when including complexity from small-scale variations, indicating that we can accurately simulate the scattering process in the medium.

3.5 Results

3.5.1 Qualitative Comparions

In this section we quantify the contributions to high-frequency ground motion from both small-scale fault geometry and media complexity and perform validation against recent GMPE relations. We compare both the median and intraevent variability of ground motion for both the synthetic data and empirical models. We analyze the ground motion simulated from both 1D and 3D background models, with small-scale medium heterogeneity using a range of statistical parameters, and different exponents of frequency dependent attenuation. First, in Figure 3.5, we qualitatively compare the ground motion with and without small-scale heterogeneity for two snapshots in time, for the fault-parallel component. One can see both the complexity originating from the rough-fault rupture, as well as the waves backscattered behind the main arrivals for the model including small-scale media heterogeneity.

Next, we compare spatial maps of the final ground motion. Typically, in dealing with empirical data, the logarithm of a peak ground-motion parameter or response spectral ordinate is used as a metric to characterize the amplitude of ground motion. Here, we compare GMRotD50 values of pseudospectral ac-

celeration (SA) at 5% damping, the orientation-independent geometric mean of the orthogonal horizontal components rotated through all possible non redundant rotation angles, which removes the sensor orientation component of aleatory uncertainty (Boore, 2006). Figure 3.6 plots SA at a period of 0.3 s for both 1D and CVM background velocity models with and without statistically-described media heterogeneity. A few observations can be made; one is that small-scale media heterogeneity serves to spatially redistribute the energy, particularly as a function of azimuth from the fault plane. This arises from the complicated multi-paths that energy takes when including small-scale complexity in the medium. Additionally, it is seen that the ground motion is much larger off the ends of the fault. Part of this is due to ground motion being highly coherent when using simple layer models, emphasizing cones of directivity, even at the higher frequencies. This is strongly reduced in 3D models that include large-scale features that can serve to scatter long-frequency waves, reducing the wave-guide effect (Figure 3.6, bottom). It is clear the ground motion is a function of both source and path effects, not just surface velocities, indicated by the lack of correlation between V_s structure seen in Figure 3.4 and the ground motion amplitude plotted here.

3.5.2 Effects of Q

We next compare the synthetic ground motion quantitively with empirical observations in a variety of ways. The ground motion is output at every 4th grid point in our model domain, allowing analysis at a resolution of 80 m. The stations are sorted by grouping them into distance bins defined by r_{rup} from the mean fault plane (which equals the Joyner-Boore distance here for a strike-slip fault) excluding the absorbing boundaries. This gives a minimum of a few thousand stations at each distance interval (at 1 km widths) for a total of just under 4 million stations. We compute the predicted ground motion from four leading recent NGA West 2 relations (Abrahamson et al., 2014; Boore et al., 2015; Chiou and Youngs, 2014; Campbell and Bozorgnia, 2014) at the same resolution of the output data, using the parameters in the NGA models computed from the simulations. These include the closest distance to the fault surface (R_{rup}), the depth to $V_s = 2.5$ km/s,

$Z_{2.5}$, the time-averaged upper 30-m shear-wave velocity, and depth to the top of the rupture as a source parameter. We compare the synthetic median SA and empirical predictions in Figure 3.7 for different anelastic attenuation models and different power-law exponents. Because the different GMPEs use different model parameters and expressions to relate the empirical observations, there is significant variation of the predictions at a specific period, particularly at distances close to the fault. The shaded region for SA indicates the range of 4 median predictions and the dashed blue lines corresponding ± 1 interevent standard deviations. For example, the 84th percent event, i.e. the median plus one standard deviation of the inter-event component of variability τ, is added onto the range of the four GMPE medians.

It is seen that there is little difference in models with varying power-law models and different $Vs - Q$ relations (unless specified, $Q_s = 0.05 * V_s$) at long periods (3.0 s). The ground motion decays generally at the level of 2 interevent standard deviations above the median. This is larger median ground motion as compared to Shi and Day (2013) for a few reasons. One, we are using a layered velocity model, with shallow low-velocity layers, that serves to increase the ground motion through an impedance effect and trap surface waves. We also are including ground motion off the ends of the fault, beyond the spatial region that the SORD simulations captured, where Figure 3.6 indicates experiences the largest ground motion. Finally, we do not incorporate nonlinear effects, that would serve to reduce the ground motion. This additional feature is included within Chapter 4 for dip-slip models.

There starts to be minor differences between power-law models at $T = 1$ s, as spectral acceleration is sensitive to a broad bandwidth. At shorter periods, for example $T = 0.2$ in Figure 3.7, it is clear that ground motion attenuates very rapidly, deviating increasingly from the GMPE median ground motion decay as a function of distance, for a constant Q model. Power-law exponents of $0.6 - 0.8$ do a much better job matching the observed decay in energy as a function of distance for both long and short periods.

Several tests were performed to ensure that the spatial selection of stations

didn't bias the results. One, spectral observations from the simulations were sorted into several different sized bin-widths, ranging from 1-20 km, calculating the log-normal mean and standard deviation for each bin. This method produced similar values of both median and standard deviation, albeit at a lower resolution. Because of the regular grid of synthetic stations, there are many more stations at azimuths near the fault-strike, compared with perpendicular to it. We analyzed for spatial bias by choosing a random selection of points within the medium and found that this had little effect on both the median and sigma values. Additionally, assigning the same number of receivers in both the forward and backward directivity regions as described in Somerville et al. (1997) and Spudich et al. (2013) (see Appendix 3.11.C for more a spatial map of the predicted directivity coefficient) produced no bias; the medians remained indistinguishable within the epistemic uncertainty.

We also compute the intra-event variability, or ϕ, of our synthetic simulations considering a lognormal distribution, calculated from the standard deviations of the residuals. Here we assume that sigma represents only aleatoric ground-motion variability. Appendix 3.11.C plots histograms and q-q plots comparing the log-normality of residuals, showing that the distribution becomes more normally distributed when including more complexity in the velocity model. The within event residuals represent azimuthal variations in source, path and site effects that aren't captured by a simple distance metric and a site-classification based on the average shear-wave velocity. The lower row of Figure 3.7 plots the within-event standard deviation in logarithmic units and shows the range predicted from the 4 GMPE models. It is clear that when the ground motion amplitude increases from either adjusting the $Vs - Q$ relation or power-law exponent, there is greater variability at a particular distance, from the increased deviations as a function of azimuth. The values are seen to increase at long periods from distances near the source up to the edge of our model domain, where they are near the expected level. At shorter periods (higher frequencies) it is clear that the variability is much higher than that of observations, generally increasing as a function of distance, due to the large contrasts in ground motion in azimuthal regions along and perpendicular to the strike of the fault.

3.5.3 Effects of Heterogeneity

Here we compare models including heterogeneity at both small and long wavelengths. Previous work has looked at the effects of small-scale heterogeneity, particularly for simple source models, such as point sources (e.g. Frankel and Clayton, 1986). Hartzell et al. (2010) looked at the effects of random correlated velocity perturbations on predicted ground motions and the effect of different correlation lengths and standard deviations up to 1 Hz. He found that there was a significant increase in the variability of motions compared to the non-perturbed case. Imperatori and Mai (2013) also looked at the influence of heterogeneity in several earthquake source models, including one-dimensional models of earth structure, and found a loss of radiation pattern and directivity breakdown at higher frequencies in elastic models including heterogeneities. They also found that coda wave generation is very sensitive to the spectral properties of the medium, both the correlation length and Hurst exponent. Additionally, they showed that scattering can affect ground motions and variability even at short distances from the source. Takemura et al. (2009) showed the distortion in the S-wave radiation pattern as frequency increases from 2 to 5 Hz when including small-scale heterogeneities.

Figure 3.8 plots both spectral acceleration and within event standard deviation for periods of 1 and 0.2 seconds for a background 1D layered model. Unless specified in the legend, all models use a power-law exponent of 0.8, deemed the most appropriate from the distance decay observed in Figure 3.7. A variety of models are superimposed here, comparing differing correlation lengths, random seeds, varying σ of small-scale heterogeneity, as well as a comparison with the hybrid approach. In the case of models with media heterogeneity, we used adjustment factors from Boore et al. (2015) to correct the spectral accelerations from a common reference value of V_{s30}, referred to as V_{ref}, here at 863 m/s, using ln $Y - S_{BJ}(V_{s30}) + S_{BJ}(V_{ref})$, where Y is the value of spectral acceleration at some period, $S_{BJ}(V_{s30})$ is the log amplification of the site V_{s30} value and $S_{BJ}(V_{ref})$ is the log amplification of the reference velocity at 760 m/s. Correcting the spectral accelerations had negligible effect on the medians and sigma values obtained, with the corrected values lying almost identically on top of the unmodified ones. We

chose not to consider the variation in $Z_{2.5}$, which would likely average out as well.

We find that the features we observe are consistent across differing periods, but with amplified effects as period decreases. For example, at a period of 1 second, all models of median spectral acceleration are clustered around the model with no small-scale heterogeneity, with only small differences between one another. At a period of 0.2 seconds, however, there are significantly larger differences between models with and without small-scale heterogeneity, and values of σ. Some general observations follow; one is that there is no significant difference in the effects of two different random seeds used here in modeling the heterogeneity. The method of binning a large number of stations together averages out any differences that may be seen from different small-scale media structure. However, if we choose to look at individual stations, a suite of random velocity models should be used to determine the range of ground motion expected from variations in velocity structure.

The effect of adding in heterogeneity tends to increase the median ground motions, but only significantly so at higher frequencies for large σ, and increasing as a function of r_{rup}. The effect of correlation length on spectral acceleration medians has little dependence here at a specific period, but as shown in Chapter 4, can vary as a function of frequency. We also include a gradient model, that has large σ (10%) near the surface, and linearly decreasing down to 2% at 7.5 km depth, and thereby set to a constant below this. This is a more realistic representation of the real earth, where the normal stress increasing as a function of depth from increasing lithostatic pressure likely reduces the amplitude variations at the same correlation length. Figure 3.8 shows that the gradient model produces similar ground motion to large σ near the source, and similar to models with no heterogeneity farther away. From this, we deduce that near surface heterogeneity largely affects areas near the source, while deeper variations determine ground motion at distances farther from the fault.

The hybrid technique shows very similar median values at longer periods, as it is derived from the low-frequency synthetics. At shorter periods, a significant discrepancy is seen; the hybrid median is much lower than that of the empirical simulations. This could be due to a variety of reasons. One, as already mentioned,

nonlinear effects such as plasticity, will reduce the ground-motion at higher frequencies, where Figure 3.8 shows it as being upwards of $2-3$ g's near the fault. This near fault reduction will likely also affect the ground motion further from the source. Additionally, we have not specifically included κ as the hybrid technique does. The Discussion section (3.6) delves into this aspect further. The Q_0 values also differ in the two techniques, but this is likely not that significant, and would actually produce an increase in the deterministic ground motion as Q_0 is, in general, smaller than in the hybrid technique, particularly in the near surface region where V_s is smaller. And finally, the hybrid approach could potentially be biased, as it is designed to fit the GMPEs.

Looking at the standard deviation, we find there are oscillations at long periods, but the general trend, as in Figure 3.7, is to increase as a function of distance. Here the largest variation in standard deviation comes from models including heterogeneity, which serves to reduce the variability. This is particularly evident at higher frequencies, where the energy redistribution due to scattering favors less variation as a function of azimuth. Both the hybrid approach and 5% σ in small-scale heterogeneity in the deterministic simulation show that models are fairly constant as a function of distance and very near that of empirical observations, with an average of about 0.45 logarithmic units. Atkinson (2006) found that sigma for individual stations (ϕ_{ss}, known as the event-corrected single-station standard deviation or single-station ϕ) is less than that of the overall sigma, and was reduced even further if only looking a fixed azimuth from a single fault. Lin et al. (2011) found that single-site standard deviations are about 10 % smaller than the total standard deviation, whereas single-path standard deviation is about 50 percent smaller. Rodriguez-marek et al. (2013) found that ϕ_{ss} is largely region independent, with an average value of $\phi_{ss} = 0.45$ fitting the data across all periods, with little trend with V_{s30}. They find larger value of ϕ_{ss} at shorter distances, but this is possibly due to limitations of the data. The lack of available records near the source for $> M_w$ 6 events produces an interest to the values of single-station sigma obtained from simulations. Here, we argue that our sigma values are lower than expected from the ergodic assumption since we have no site effects, and at

large distances from the source, path effects are minimal in a 1-D layered model.

Imtiaz et al. (2015) looked at the distance variability of ground-motion for bilateral faults, finding that the variability tends to increase with distance up to about 20 km for PGV (up to 3 Hz), and then increases more gradually from the source. This agrees with our simulations, where at short distances ϕ is controlled mainly by source parameters and increases up to about 20 km, where it remains fairly constant in the distance range considered here. At farther distances, extended sources behave like point sources and ϕ is likely controlled by the radiation pattern shape of S and Love waves. Imtiaz et al. (2015) also showed that for unilateral ruptures, higher ϕ values at shorter distance are due to presence of directivity effects and pointed out that most stations at short distances are in the low azimuth region (from strike), and have strong amplification due to forward directivity effects. In our model, at short distances most stations are along the fault, while further away there are more stations off the ends of the fault. As mentioned previously, however, no spatial bias is seen to exist when using an equal distribution of the number of stations in forward and backward directivity zones.

Vyas et al. (2016) also analyzed the distance dependence of variability and introduced a power-law decay of standard deviation with increasing distance for unilateral ruptures. They argued that large near-field sigma is due to the presence of strong directivity and rupture complexity. When analyzing variability as a function of azimuth, they found that sigma is highest in the forward directivity region and lowest in backward directivity region. They found that slip heterogeneity is the controlling parameter for the power-law decay of ground-motion variability at low frequencies (< 0.5 Hz). Here, we find that at short distances from the earthquake source, ground motion amplitudes vary by almost an order of magnitude. This reflects the large variability of ground motions when wave propagation from a finite fault is characterized by distances closest to a point on the fault rupture. The distance to asperities could be a more representative parameter that the closest distance from the entire fault plane, at least at low-frequencies. Prior knowledge about rupture directivity could also help to determine ϕ, and azimuth may help as an additional parameter at low frequencies.

Next we analyze results from simulations using a 3D background CVM model, for our rough-fault model input along an 80 km section of the San Andreas Fault. Figure 3.9 plots SA and intraevent variability in the same format in Figure 3.8 for a subset of models that span the end member cases of heterogeneity. Here, we extracted the GMPE relations including the variation in V_{s30} and depths to 1 and 2.5 km values of V_s. The corresponding range in GMPE medians is slightly increased. We immediately see that differences in the 3D results compared to the 1D layered models. As seen in Figure 3.6, ground motion is significantly reduced at all distances from the fault, consistent at all frequencies. This is due to the reduction in broadband directivity from the scattering that occurs at long wavelengths from the 3D background structure. No longer is the energy coherently directed outward from the hypocenter, but is redistributed and scattered at depth. The absence of sharp velocity discontinuities also prevents important wave conversion and reverberation phenomena, potentially able to reduce peak amplitudes.

The value of σ of small-scale heterogeneity is seen to make a change in the behavior at high frequencies. At 5% σ we find similar results as in Figure 3.8 for 1D layered models: energy is increased. At 10% σ, however, we see that ground motion is reduced, particularly at larger distances from the source. We attribute this to scattering attenuation overpowering the lateral azimuthal redistribution effect we see for lower σ values. As energy travels from the source to the surface, it is scattered when meeting an impedance contrast. A larger σ value produces a larger impedance contrast, thus changing the angle of reflection. This energy is scattered in multiple directions, with some being lost to downward propagating waves that will attenuate within the upper mantle (the deepest portion of our model). Korn (1993) found that coda decay is dominated by leaking of scattered energy into the mantle and not by inelastic effects (diffusion energy). This effect is clearly seen at large distances, where SA falls off rapidly. The gradient model where σ varies with depth agrees with this explanation, as the near-surface region is identical, showing that energy is increased compared to the model without heterogeneity. Energy coming from a deeper source does not develop a large coda wave amplitude, as some of the energy reflected at the free surface leaks back into the deeper crust.

To better explain this, we have plotted horizontal components of seismograms for homogenous, and 5 and 10% σ models in Figure 3.10 and 3.11 extracted along a profile perpendicular to the fault, for 1D and 3D background models, respectively. We plot acceleration records, where the scattering is most apparent. The 5% σ model for both 1 and 3D background velocity models shows the characteristic loss of energy from the main arrivals, due to scattering, and the increase in coda energy. This is seen to both increase and decrease the PGA, but on average increases it. At higher σ in the 3D background model, we still see the same features as compared to the model without small-scale heterogeneity, but with a significantly reduced coda amplitude. Complexities from source finiteness and potential rupture complexity in our 3D simulations may help explain why this result is different from that of previous studies showing that σ scales the energy in the coda in 2D (e.g. Frankel and Clayton, 1986 and Bydlon and Dunham, 2015). We hypothesize that a point-source would have more typical effects, i.e. scattering causing mainly attenuation because of the lack of directivity from the source.

3.5.4 Duration

Parameters related solely to the amplitude of the ground motion, such as PGA, are often insufficient indicators of damage. Metrics that incorporate the amplitude, frequency content, and duration of the ground motion across a broad frequency bandwidth are likely to be more reliable predictors of damage than ones only relating to ground motion amplitude. Arias Intensity (AI) is a scalar parameter that captures the potential destructiveness of an earthquake as the integral of the acceleration time history. It is a duration-related ground motion parameter of cumulative energy per unit weight absorbed by an infinite set of single degree of freedom oscillators having fundamental frequencies uniformly distributed from $0 - \infty$ with zero damping. AI is mathematically defined by the equation $AI = \pi/(2g) \int_0^{t_{max}} a(t)^2 dt$ where $a(t)$ is the amplitude of the acceleration at time t, g is the acceleration due to gravity, and t_{max} is the total duration of the time series. As it is an acceleration based parameter, AI is not very sensitive to long periods and is not significantly affected by forward rupture directivity.

Afshari and Stewart (2016) used the NGA-West2 data set to build a model for the duration dependence of $5-95\%$ normalized AI, D_{5-95}. They used additive path terms with distance breaks at 10 and 50 km, and a site term that increases duration for decreasing V_{s30} and increasing basin depth. They found residuals to be log-normally distributed at confidence intervals $> 95\%$. Figure 3.12 plots median values of duration of $5-95\%$ AI and intraevent standard deviation for 1D-layered model medians and variability. It is seen that the the complex source model combined with 1D scattering has a significant duration, rapidly increasing as a function of distance. The addition of small-scale heterogeneity strongly increases the duration, matching that of 1 interevent standard deviation above ~ 5 km using a 5% σ model of small-scale heterogeneity, and at about 2 interevent standard deviations at 10% σ. The hybrid model seems to have a relatively accurate source effect, indicated by the close agreement at near distances, but increases a little too rapidly at larger distances, indicating the path effect is deviating from the GMPE for this specific realization. We again find that heterogenous structure tends to reduce the variability, decreasing as a function of distance. It is interesting to note that the 10% σ models of heterogeneity best agree with that of the hybrid approach used here, much lower than that of GMPE observations. Figure 3.13 plots the results for a background 3D model. Similar characteristics are seen, but as in the case for high-frequency SA, there is seen to be a decrease in AI at large σ, as well as well as at a long correlation length (500 m). All the intraevent values that include small-scale heterogeneity hover around the expected range of variability, with the model without over-predicting the empirical result.

3.5.5 Pulse Period

Double-sided velocity pulses caused by constructive interference of seismic waves as a rupture propagates along a fault tend to occur far from the epicenter but close to the fault, amplifying the structural response at long periods. Forward directivity occurs when both the rupture propagates toward the site and the direction of slip is aligned with the rupture direction. This leads to a significant increase in the amplitude and a reduction in the duration of the ground motion, mainly

expressed in the long period range of the strong ground motion. As frequency and distance from the source increase, rupture front incoherence and scattering in the propagation media gradually weaken the directivity signature.A transition occurs between $1 - 4$ Hz for directivity effects and where scattered wave energy becomes dominant. Somerville et al. (1997) reported directivity effects from large events are found to be erased at short period.

Graves (2016) used a generalized hard-rock velocity structure and analyzed the fault-normal to fault-parallel acceleration response spectral ratio, finding it to be > 1 for long periods. Their goal was to reduce the coherence of radiated higher frequency (> 1 Hz) ground motion in the forward rupture directivity direction, to match observations which see that the FN/FP ratio decreases steadily with frequency until reaching a level value of about 1 at 1 Hz.

There is a group of proxy metrics of engineering relevance that a wide range of data has been shown to be consistent with. Chapter 4 analyzes a few of these proxies in comparison with deterministic simulations. Here, we look at a secondary parameter, less precisely constrained by an empirical model, known as the directivity pulse period. There are few records at short distances where directivity is most likely to occur. Simulations may be able to provide a more accurate characterization of directivity pulses and near fault ground motions. We use the wavelet analysis technique to extract the largest velocity pulse from the fault-normal ground motion to isolate directivity effects (Baker, 2007). It is ensured that the pulse has a high peak velocity, and has a high pulse indicator greater than 0.85 (chosen by Baker, 2007 to be the best way to discriminate between directivity pulses), which limits the pulses to be early in the time history, where directivity pulses are more likely to occur.

Figure 3.14 plots the pulse period extracted from the fault-normal component records for both 1D and 3D background models. Components such as small-scale heterogeneity and attenuation have little effect on this proxy, as it is primarily influenced by low frequencies. It is seen that the regions where a pulse exists are constrained to be near the fault rupture, extending out from the hypocenter, as expected. Interestingly, there are few pulses extracted off the ends of the

fault, particularly for the 1D simulation, where from our spatial ground motion maps, directivity would seem to be quite large. The 3D background model introduces a lobe of directivity off the left end of the fault, with fairly short periods, decreasing away from the fault. This may be related to the velocity structure at depth. Theses results are averaged as a function of distance and plotted in Figure 3.15, along with the predictive relationship, and the standard deviation, ln T_p. It is seen that the 3D background structure reduces the directivity down into the range predicted by observations. The distance dependence of the pulse period also agrees with observations, finding few stations$>$ 30 km that are found to have a pulse period, as shown in the histogram of Figure 3.15.

3.6 Discussion

3.6.1 κ

To ensure that synthetic ground motion is realistic at high frequencies, it is necessary that the ground motion records have a spectral decay similar to that of observations. Anderson and Hough (1984), first described this trend as κ, by modeling it as an exponential decay. This decay is measured from above the corner frequency, f_c, up to to the noise level or Nyquist frequency. They found consistent values for southern California records in the range $\kappa = 0.04 - 0.06$ for hard rock sites. Here our seismograms are band-pass filtered to the resolution of our finite difference grid, < 7.5 Hz, and we measure κ from the synthetic simulations. Since the source is approximately flat up to 8 Hz, there is no κ contribution from the source (on average). κ is calculated using a linear least-squares fit to spectra at high frequencies (in frequency/log-amplitude space), determining the average horizontal κ value from the two perpendicular components. We first choose a narrow window ($5 - 7$ Hz) where the Fourier energy starts to deviate from a flat spectrum. We find that the window length has little influence on determination of κ as long as the strong energetic part of S waves is encapsulated in the selected window. At individual stations, site amplification effects leave peaks in the spectra, making it more difficult to accurately pick the slope, and there is significant variation in κ

from source directivity effects. Thus, as the results are very inconsistent across the confined bandwidth, we stacked Fourier Spectra as a function of r_{rup} to average out individual site response and reduce the high-frequency oscillations: see Figure 3.16. We find, that in general, the measured κ from using a power-law exponent of Q of 0.8 and $C = 0.05$ for $Q_0 = C * V_s$ (with Vs in m/s) in our attenuation relationship is similar to the trend found in Anderson and Hough (1984).

κ is primarily a high-frequency effect, having the most influence on spectral content for frequencies greater than $5 - 10$ Hz. As κ values may be inconsistently calculated across a narrow bandwidth (as performed in Figure 3.16), we introduce an alternative approach to model a target κ_0, the site effect, that may be necessary to include as simulations extend to higher frequencies. This approach employs a frequency independent attenuation zone at the near surface to simulate κ_0. κ_0 is taken to be primarily site attenuation from local geological conditions down to a few hundred of meters or a few kilometers beneath the site under study (Anderson and Hough, 1984). Hough et al. (1988) also hypothesized that there exists a shallow attenuation layer present along the near surface, overlying a less attenuating medium. Abercrombie (1997) conjecture that 90% of total seismic attenuation in bedrock occurs in the upper 3 km of the earth's crust. Q is observed to be low $(15 - 50)$ even for Class B V_{s30} values in the shallow crust (Assimaki et al., 2008). Anderson (2015) also used low Q values in the shallow sediments (3 km) to model κ_0.

The κ_0 value corresponds to the attenuation that S-waves encounter when traveling vertically thorough the geologic structure beneath the station. Site lithology, stratification, and randomness significantly affect attenuation estimates in the near surface. Houtte et al. (2011) also found that the superficial layers of the soil predominantly influence κ_0, but there remains a component with a deeper origin as well. It is possible to estimate the contribution from the site effect by relating $\exp(-\pi f \kappa_0)$ and $Q_s = \exp(\frac{-\pi f R}{V_s Q(f)})$, giving $\kappa_0 = \frac{R}{V_s Q_s}$, where R is distance, Q_s the shear attenuation, and V_s the shear wave velocity in that layer. We can sum up the contributions from each layer and assuming a constant Q model at the level of Q found at 5 Hz (as an approximation) in $Q = Q_0 f^{\gamma}$, we find κ_0 in the top 3

km to be an order of magnitude smaller than the expected value near 0.04 s for western North America. Thus, it is possible that we may be not including sufficient attenuation to model the high-frequency decay in our models.

As we previously showed that a Q(f) model with a power-law exponent of 0.8 matches the decay in energy as a function of distance, we introduce a shallow (3 km) region where Q follows a constant Q model along the surface, approximating the depth to bedrock. This constant Q layer in the near surface should have a nearly common attenuating effect at all stations. We use the relation $Q_s = 0.025 * Vs$ to obtain a κ_0 value of ~ 0.03 for both the 1D layered and 3D velocity model. Thus, the shallow region introduces a site effect on κ, while the path effect is derived from the underlying region of Q(f), with path attenuation from higher quality factor in the deeper crust. Figure 3.17 plots the corresponding value of κ as a function of distance, for both the 1D and 3D models. Instead of picking the frequency at which the spectra starts to decrease linearly with frequency (f_E), we set the bandwidth of our calculation from $1-7$ Hz to calculate κ. It is seen that by adding in $\kappa = 0.03$ corresponds to an increase in the calculated κ very near that value. We note that the values are smaller (sometimes negative in the unmodified approach) for models with small-scale heterogeneity , as it tends to increase the high-frequency energy, reducing the decay in the spectrum. This is in contrast to an increase in κ when including small-scale heterogeneity from site attenuation (stratigraphic filtering) as seen in Ktenidou et al. (2015). This may be due to the complicated influence from laterally-propagating waves (e.g., surface waves), as well as 3D heterogeneity changing the ray paths to form multiples.

Figure 3.18 shows the results for SA and intraevent variability (comparable to Figure 3.9) for models with and without the κ implementation for 1D layered models. It is observed that the effect is to reduce the ground motion medians, with significant effects at higher frequencies, as expected. This new method drops the median values for both models with and without heterogeneity to near the range of the hybrid technique, and with a distance dependence near that of a median event above about $r_{rup} = 5km$ or so. The effect of kappa is seen to reduce the variability at high frequencies for this 1D layered simulation to align near that of

empirical observations.

Figure 3.19 shows the corresponding results for a 3D background model. Again, the high-frequency energy reduction causes a decrease in spectral response values, to lie near that of GMPE median precautions. The intraevent variability here is actually increased for models that include the κ_0 approach, however; it is thus still necessary to have small-scale heterogeneity to match variability in our models. This brings the model including heterogeneity to be right in the range of expected values for a distance above 30 km or so.

3.6.2 Future Work

As the next step, there are a variety of routes to continue to advance ground motion simulations. One approach is to conduct a wide range of scenario earthquake simulations from the information gained in this study, with a focus on specific source-receiver geometries; this would help ascertain the range of ground motion expected at a given station. Additionally, simulations could be performed to homogenize the radiation pattern effects that we see here from just one bilateral event. Running events with different stress drops would help to determine the correlation with median ground motion and impact of the source on sigma.

Graves et al. (2010) used physics-based 3D ground motion simulations to generate synthetic ground motion data. Using many earthquake cycles (rupture scenarios) alleviates the need for the ergodic assumption. With more events and simulations, a mixed effect regression could be used to develop a GMPE based on the synthetic dataset, similar to that of Villani and Abrahamson (2015). More specific simulations should be performed to isolate the influence of heterogeneity on intraevent variability, particularly on path effects which arise from both attenuation and scattering, that would lead to a nonergodic PSHA. Empirical GMPEs can thus potentially be improved by supplementing direct observations of ground motions with simulation data that use the physics of wave propagation to extrapolate to areas of insufficient data..

An additional validation technique could be to compare with precariously balanced rock (PBR) observations. Brune (1996) found that the presence of pre-

carious rocks in Southern California is not consistent with the large value of ground motion predicted by PSHA studies; simulations could be run along the San Andreas and other major faults and compared with PBRs using the additional high-frequency content.

There are many additional features that can be included in future ground motion simulations to further increase their agreement with data. For example, Graves (2016) introduced a near fault damage zone in a 1D plane layered structure. Although it was found that this zone has little impact on the overall amplitude level of ground motion over a broad frequency range, future simulations could include such a damage zone in 3D background velocity structure to determine its importance.

More simulations are needed to fine tune our κ_0 approach, if it is deemed necessary as simulations extend to higher frequencies. Constraining the constant Q region to be set to less than 3 km would decrease the decay seen as a function of distance. Q(f) may vary with depth; introducing a gradient model where the attenuation exponent gradually increases at larger depths may better fit observations. This allows for a large potential area of research to be performed on the components influencing κ. Some of these would be to analyze the V_{s30} dependence, the correlation with basin depth, and further investigate the significance of scattering from near-surface heterogeneities.

In this paper, we ignore the nonlinear effects from plasticity in the wave-propagation that may strongly damp ground motions near the fault, as the dynamic simulation already includes Drucker-Prager plasticity along the fault. Including them in the kinematic simulation would cause a double-counting of plasticity, unless the fault boundary condition of Roten et al. (2016) is used. In Chapter 4, we neglect plastic effects in the dynamic simulation, but include them in the kinematic runs, which is shown to be important in regions of low shear wave velocities.

To develop a region and station specific estimate of ground-shaking levels for future earthquakes, it is likely that components such as topography will need to be included, causing additional diffraction and scattering. The shaking amplitude at the top of hills can be larger than that based on level surfaces. Takemura et al.

(2015) showed that topography distorts P-wave polarization, transferring energy to the transverse motion, but is only significant at locations near the station, accounting for only 12% of the high-frequency wavefield. Mai and Imperatori (2015) also analyzed topographic effects, finding that they can be significant, especially in the proximity of the source. Future simulations should continue to evaluate the effects of irregular topography in combination with the effects of velocity inhomogeneity.

Takemura and Furumura (2013) showed that different regions have different velocity fluctuations; this will become important when working with different locations. Here, we ran models with the heterogeneity spectrum of the crust changing with depth, particularly in the near surface where open joints and fractures present can change the correlation structure. Multiscale models may also be appropriate, with a depth dependence.

Many studies have looked at contributions from scattering and attenuation (e.g. Mayeda and Koyanagai, 1992) and the separation of the two (e.g. Fehler et al., 1992). The total apparent attenuation, Q_{app}, comes from the combined effect of both intrinsic (Q_i) and scattering attenuation (Q_s): $\frac{1}{Q_{app}} = \frac{1}{Q_i} + \frac{1}{Q_s}$ (Parolai et al. (2015)). Scattering Q is a measure of apparent attenuation and causes more energy to be distributed into the coda from the direct pulse with increasing time. Waves are attenuated along the paths from the source to the scatterer and from the scatterer to the receiver. Thus, the energy reduction from scattering depends largely on the part of the record used. As we have shown, small-scale inhomogeneities can cause additional high-frequency attenuation through scattering. This is explained from two mechanisms: multiple reflections cause part of the energy in the up-going waves to be diverted downwards into the Earth and forward scattering of energy causes a redistribution of energy in the time history. Higher σ in the small-scale heterogeneity model should mean more attenuation in the direct waves, and more energy in the late coda due to strong multiple scattering. We observed that a waveguide effect, in which surface waves propagate across the basin, generating enhanced long-period motion amplitudes and shaking duration, exists in our 1D models. The ground motion distance attenuation here is controlled by geometric spreading of the wave field, anelastic attenuation, scattering effects, and the gener-

ation of surface waves, and body to surface wave conversion at low frequencies. A 3D background model with σ of 10% adjusts the media at depth and changes the path rays travel, thus modifying its amplification and complicating the predicted attenuating behavior.

Larger intrinsic attenuation entails greater loss of elastic energy with time from both the coda and the direct wave. We find that intrinsic attenuation dominates over the scattering attenuation above 1 Hz for our layered models, but being more equal for a background CVM structure. Equivalent Q estimates may be made by a loss of energy from the primary waves or presence of energy in the coda (Kang and McMechan, 1994). A better method to separate scattering and anelastic attenuation would be to use the method of Frankel and Wennerberg (1987), who introduced an energy flux model that assumes a spatially uniform distribution of coda wave energy, applied in Jemberie and Nyblade (2009). More investigation should be performed to determine the details and significance of scattering on coda energy as well as the contribution between scattering and intrinsic Q, and their separation.

Future work could analyze coda Q, which is measured simply from the coda at different lapse times to determine depth dependence (Parvez et al., 2008). Coda Q measured from synthetic seismograms should match observations. However, many studies have shown that coda Q is close to intrinsic Q (e.g. Jin et al., 1994). Frankel and Clayton (1986) compared observed and predicted coda decay up to the time corresponding to the travel time from the source to the edge of the grid and back to the receivers. Comparisons of simulated time series are not appropriate for times greater than this, because the initial wave front has been absorbed along the edge of the grid. We ignore any discrepancies due to this approximation within this study. The separation of scattering Q from Coda Q is based on the single scattering assumption, which is valid when sigma is small. Multiple scattering occurs when sigma is large: as we have seen comparing 1D and 3D background velocity models, scattering from sharp discontinues in the media can play a major role in the attenuation process of seismic waves.

3.7 Conclusions

The ability to extend deterministic ground motion predictions to higher frequencies and predict PGA and PSA is invaluable for building engineers. Recordings in the near field of large earthquakes are sparse, so earthquake simulations become important for seismic hazard assessment. As simulations advance, we become better at constraining seismic hazard in the bandwidth important for engineering applications by deterministically modeling broadband seismic ground motion, particularly with application to regions with poor data coverage. Information inferred from simulations may have significant impact on seismic hazard estimation. A goal is to use ground motion simulations to complement the strong motion database for use in engineering applications. Before this can be done we need to compare physics-based 3D ground-motion simulations with that of empirical ground motions to ensure the decay of energy at high frequencies, decay as a function of distance, and the source model. Whereas previous deterministic ground motion studies have been severely limited by computational limitations, here we use the Titan supercomputer utilizing GPUs to extend ground motion prediction to higher frequencies using a fourth-order staggered-grid finite difference method (AWP-ODC) with a grid spacing of 20 m using geometrical fault complexity.

Here, we quantify the contributions of small-scale fault geometric complexity and small-scale velocity and density inhomogeneities in the medium that can affect the ground motion intensity included within our deterministic simulations, and validate against recent Next Generation Attenuation (NGA) relations (empirical observations). We bin stations as a function of distance and compare several metrics with empirical predictions, including spectral acceleration at different periods and duration of Arias Intensity. The slip-rates from a dynamic simulation along a rough-fault topography that follows an omega-squared spectrum are used as the input to our wave propagation code. We include frequency-dependent attenuation via a power law above a reference frequency for both 1D layered and 3D velocity structures as background models, and superimpose small-scale heterogeneity in the entire domain using a range of statistical parameters. We find that for this particular rupture model, ground motion lies within $\sim\ 1-2$ interevent

standard deviation above the median, with a spectral decay that closely matches that of the GMPEs when using a power-law exponent between $0.6 - 0.8$ above 1 Hz. Ground motion attenuates faster with distance than is predicted by GMPEs for constant Q. We found that 3D structure strongly affects azimuthal distribution of radiated energy and rupture directivity by increasing the path complexity by low-wavelength scattering.

The primary effect of both anelastic attention and scattering is to reduce amplitudes of the first propagation impulse, but scattering leads to redistribution of seismic-wave energy from low to high frequencies from the main arrivals to later in the signal. For full time-series metrics such as SA used here, there can be both an increase and decrease in the ground motion with a complicated source model that has finite length and duration. There are complementary features between scattering and apparent attenuation with heterogeneous Earth structure. We have seen that small-scale heterogeneity tends to increase median ground motion for 1D layered models, but can be strongly reduced with 3D CVM that have reduced directivity; the σ parameter doesn't seem to directly control the scattering intensity as a simple scaling factor. More simulations are needed to fine-tune the relationship between source size and apparent attenuation. Low-velocity layers acts as a wave guide, in which energy is trapped and continued scattering occurs, to create complex propagation effects. Synthetics associated with this particular medium are characterized by multiple reflections and important coda waves which counterbalance the expected decay of peak parameters. Each simulation method matches empirical models for some parameters and not others, indicating that all relevant parameters need to be carefully validated. Parameters that incorporate amplitude as well as frequency content, and duration of the ground motion are likely to be more reliable predictors of its damage potential. We find that the duration median is strongly related to the scattering energy, where both long and short scale media variations tend to increase the signal duration.

Larger intrinsic attenuation can serve to decrease the standard deviation, as a result of drop in amplitude of seismic waves. We show that small-scale heterogeneity can significantly reduce the intra-event variability at frequencies greater

than ~ 1 Hz, becoming increasingly important at larger distances from the source. This suggests the need for a highly complex velocity model to fit ground motion variability, at least when considering a bilateral strike-slip event. Scattering can be distance dependent, as a decreasing gradient model of σ in small-scale heterogeneity with depth shows reduced expected peak attenuation at larger distances from the source. This systematic path effect variability can be used to reduce uncertainty in ground motion prediction. Site and path effects will become even more significant at higher frequencies. For path effects, heterogeneity at both large and small scales is important for reducing uncertainty, depending on the frequency bandwidth of interest.

We also compared our deterministic results with that of a hybrid method generated using the low-frequency deterministic synthetics and found significant differences in both spectral acceleration median and variability at high frequencies. Part of this may be due to the stochastic part of the hybrid technique not including surface wave scattering, but specifically modeling κ_0 and a nonlinear effect. More simulations are needed to quantity the source of the discrepancies.

We examined the the decay of energy both as a function of frequency and distance, and find that our simulations are comparable to observations across a narrow bandwidth. We also introduced a technique to modify the high-frequency energy decay that relates to κ. We showed that the new approach has a significant effect at the high frequencies, while still retaining the appropriate distance decay. Heterogeneity is seen to consistently reduce the κ values. Including this approach reduced the differences between the deterministic and hybrid approaches.

3.8 Data and Resources

The southern California velocity model CVM-S 4.26 can be obtained from SCEC at http://scec.usc.edu/scecpedia/. Most of the data-processing work was done using MATLAB (http://www.mathworks.com/products/matlab/). Figures were prepared using MATLAB and the Generic Mapping Tools package (http://www.soest.hawaii.edu/gmt/). All electronic addresses referenced here were

last accessed October 2014. All other data used in this paper came from published sources listed in the references.

3.9 Acknowledgments

This research was supported through the Southern California Earthquake Center (SCEC) by the NSF Cooperative Agreement EAR-0529922 and USGS Cooperative Agreement 07HQAG0008, by USGS award G15AP00077, and by NSF awards EAR-1135455, OCI-114849, EAR-1349180, and ACI-1450451. The simulations were generated on the Titan Cray XK7 at the Oak Ridge Leadership Computing Facility in Tennessee. Thanks to Rumi Takedatsu for help in generating the hybrid broadband synthetics.

Chapter 3, in full, is a reformatted version of a paper currently being prepared for submission for publication to *Bull. Seism. Soc. Am.*: Withers, K. K. Olsen, and S. Day. Ground Motion and Intraevent Variability from 3-D Deterministic Broadband (0-8 Hz) Simulations along a Non-planar Strike-slip Fault. (2016). I was the primary investigator and author of this paper.

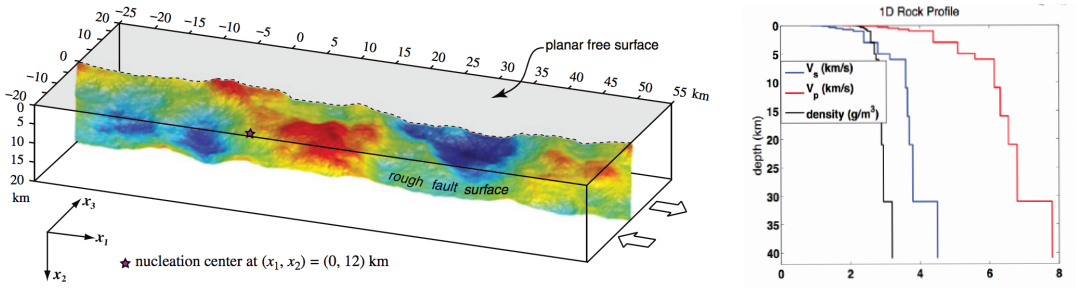

Figure 3.1: (Left) Model geometry and dimensions of the strike-slip rough fault used in this study. The rupture surface uses 4.7 million subfaults that follows a self-similar fractal distribution with wavelengths ranging from 80 meters to 80 kilometers. The strike slip fault is 80 kilometers in length, and 16 km in width. Reproduced in full from Shi and Day (2013). (Right) 1D layered velocity used in the dynamic simulation derived from the SCEC broadband platform validation exercise for southern California.

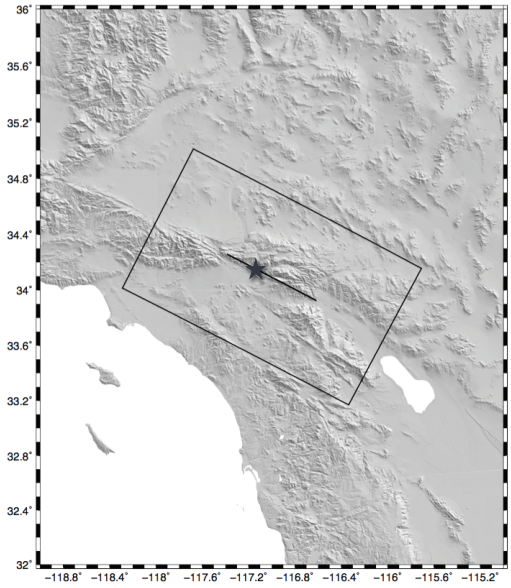

Figure 3.2: Model domain (rectangle) used in our 3D models with the same dimensions as the 1D simulations $(204, 124, 41$ km). The intersection of fault plane along surface is shown by the line, input along a 80 km segment of the San Andreas Fault. The star depicts the epicenter.

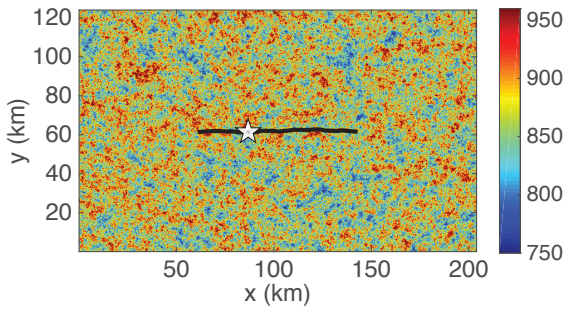

Figure 3.3: Example of small-scale heterogeneity of V_s (m/s) along the free surface with a correlation length of 150 m, anisotropy factor (vertical-to-horizontal stretch) of 5, and a standard deviation of 5% across the model domain. The black line indicates the surface intersection of the rough fault and the star depicts the epicenter.

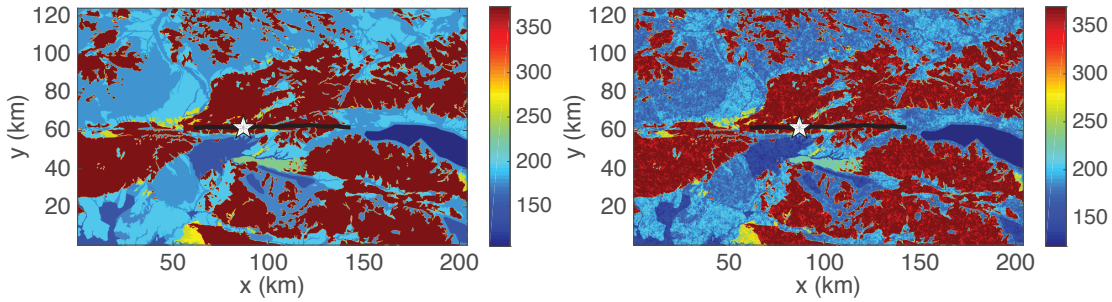

Figure 3.4: (Left) Surface view of shear wave velocity (m/s) extracted from the CVM including the GTL. (Right) Same as the left, with the addition of a statical model of heterogeneity superimposed on the background 3D model, here before clamping the minimum V_s in the background CVM.

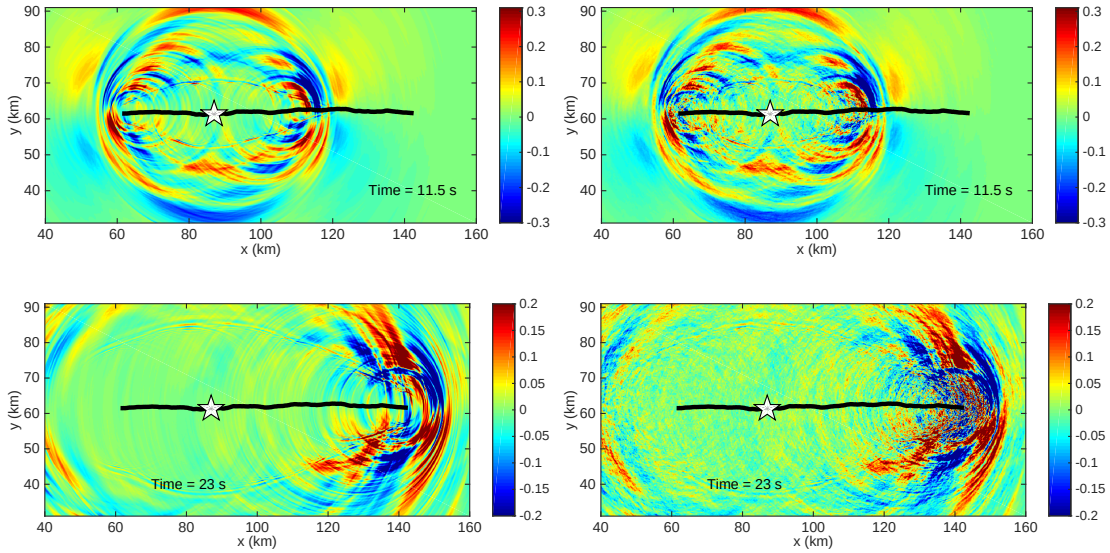

Figure 3.5: Snapshots of the fault-parallel velocity at the surface at two moments in time using a 1D layered background model (m/s). (Left) No small-scale media heterogeneity is included. (Right) Small-scale media heterogeneity with vertical correlation length of 150 m, $H = 0.05$, and $\sigma = 5\%$.

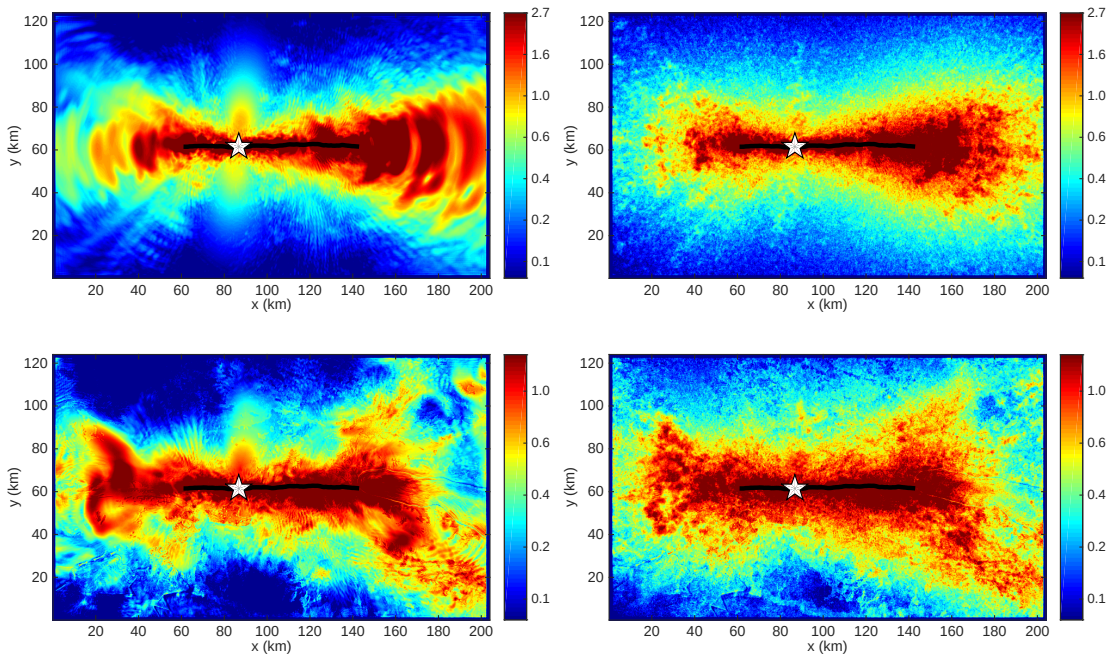

Figure 3.6: GMRotD50 maps of spectral acceleration in units of g at T = 0.3 s. (Left) Models without statistically-described media heterogeneity. (Right) Models with statistically-described media heterogeneity using a vertical correlation length of 150 m, $H = 0.05$, and $\sigma = 5\%$. (Top Row) 1D layered models. (Bottom row) 3D models extracted from the CVM.

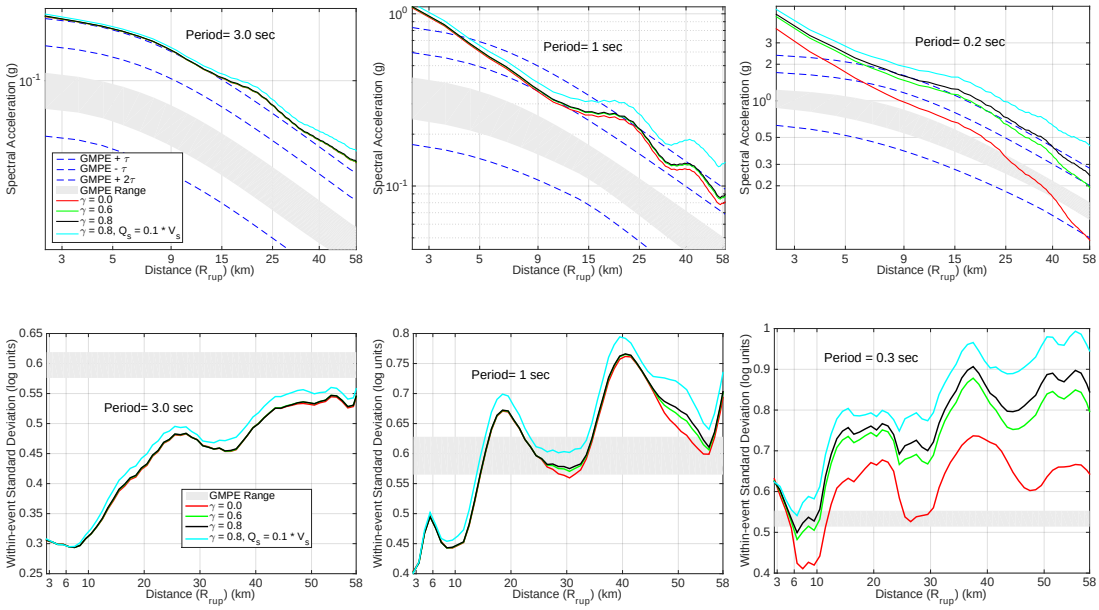

Figure 3.7: (Top) The spectral acceleration median (GMRotD50) for 3 periods as a function of distance. The shaded region indicates the range of the GMPE medians, where the dashed blue lines are the $\pm$ 1 and +2 interevent standard deviation. Unless specified, $Q_s = 0.05 * V_s$. (Bottom) Intraevent standard deviations as a function of distance, with the shaded area indicating the 2014 intra-event standard deviation range of 4 GMPE models.

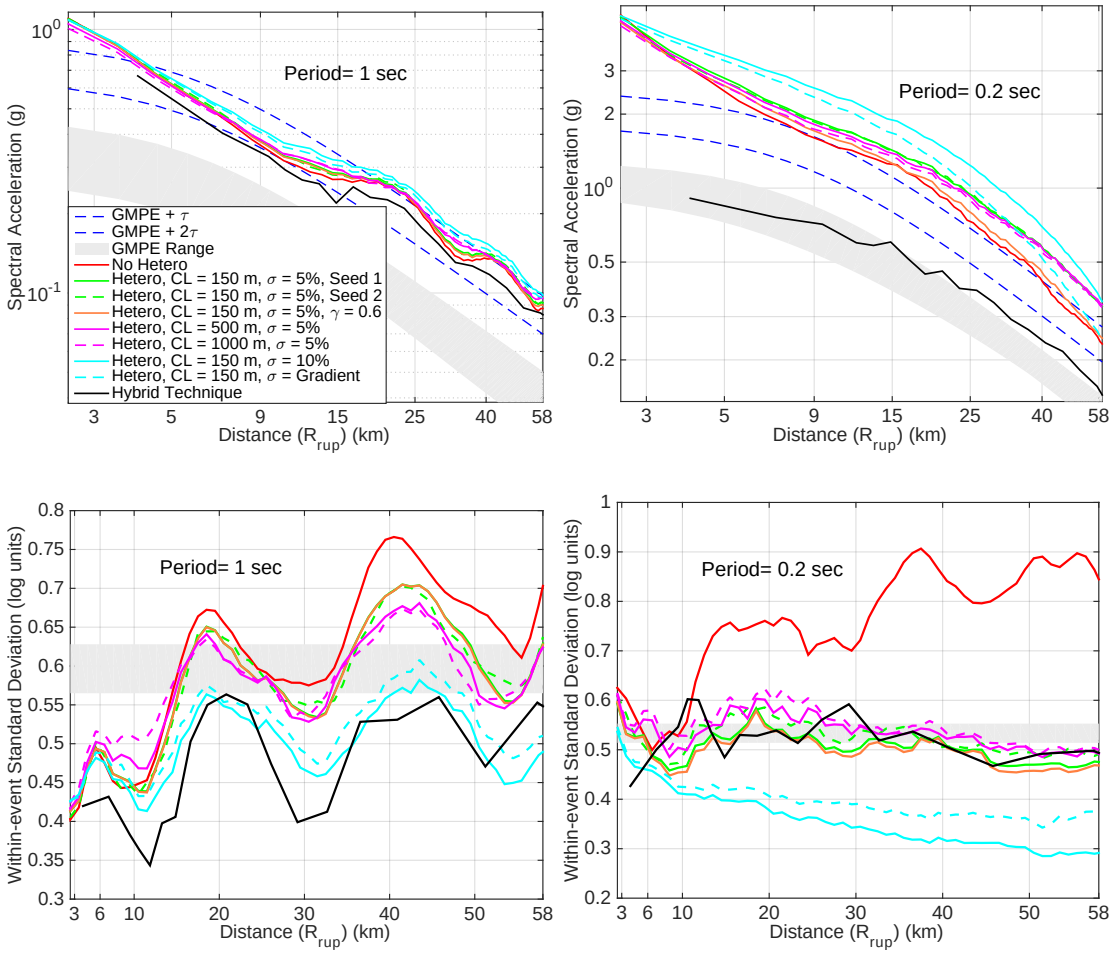

Figure 3.8: SA and intraevent variability for a characteristic long and short period showing the influence of several models of heterogeneity compared with GMPE predictions and a hybrid technique using a 1D background layered velocity model. 'Hetero' refers to small-scale heterogeneity.

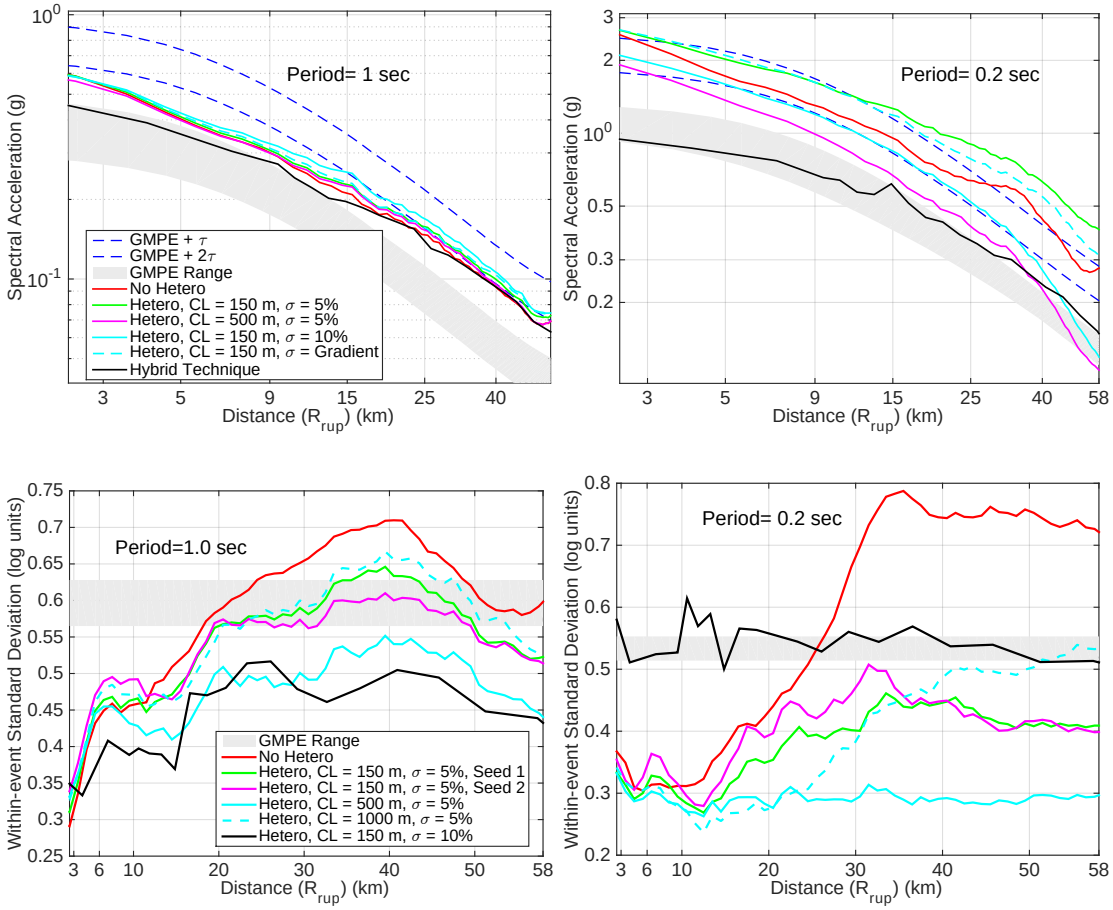

Figure 3.9: Similar to Figure 3.7, but using a 3D background model extracted from the CVM.

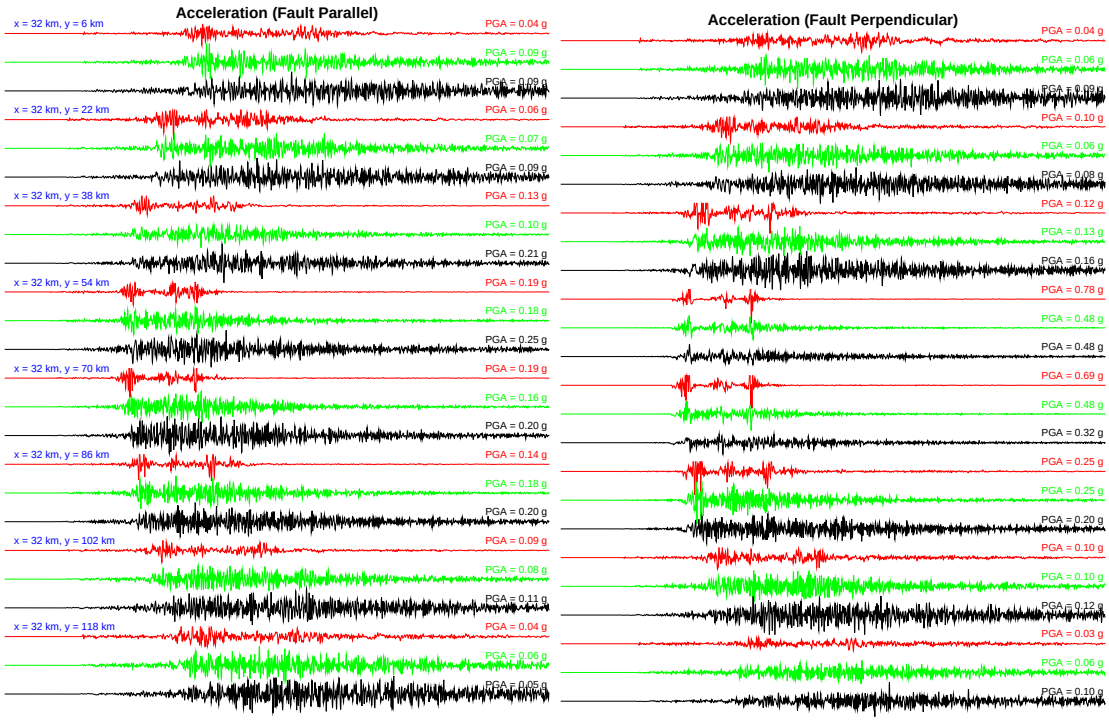

Figure 3.10: Accelerograms extracted from a profile perpendicular to the fault for a background 1D layered model, with coordinates as given in Figure 3.6 for models with 0 (red), 5 (green) and 10% (black) value of σ in heterogeneity shown in Figure 3.8.

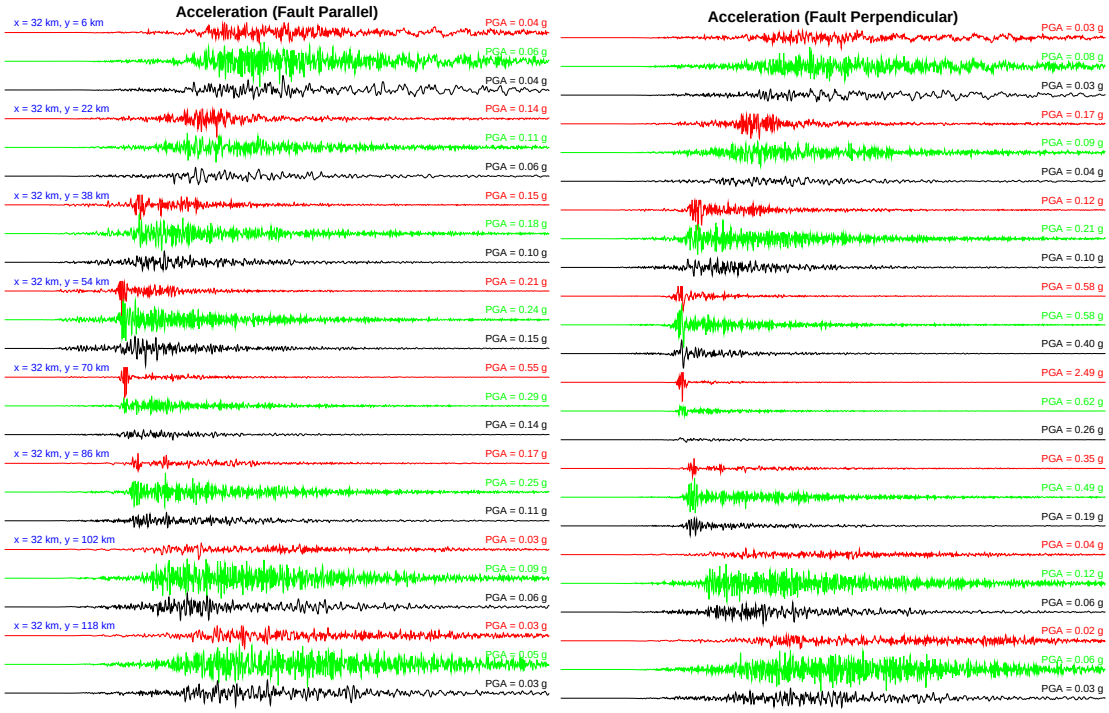

Figure 3.11: Accelerograms extracted from a profile perpendicular to the fault for a background 3D CVM, with coordinates as given in Figure 3.6 for models with 0 (red), 5 (green) and 10% (black) value of σ in heterogeneity shown in Figure 3.9.

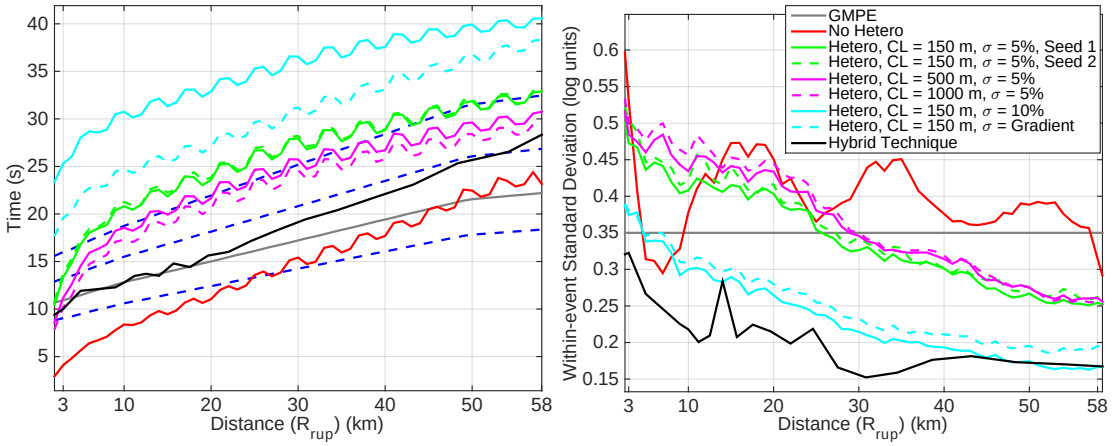

Figure 3.12: Median and intraevent variability for $5 - 95\%$ duration of Arias Intensity for a 1D background layered structure.

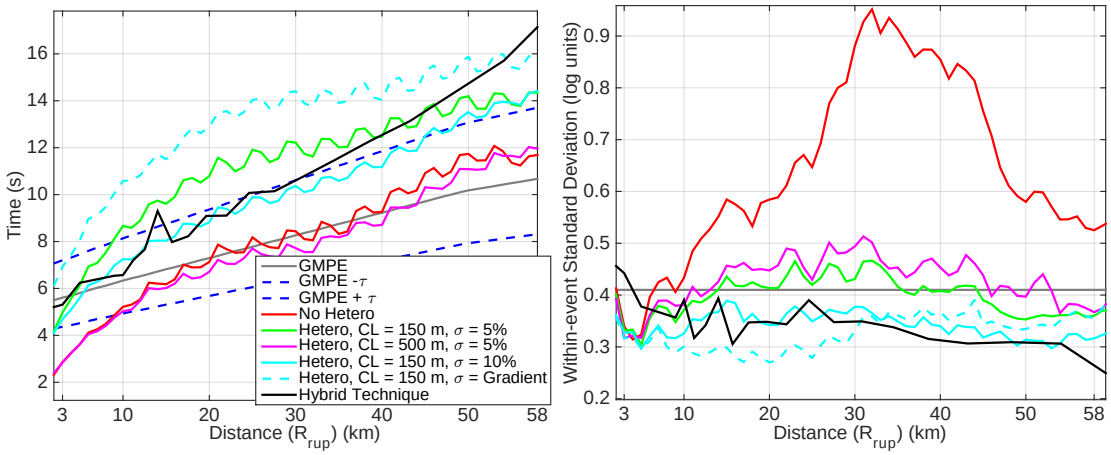

Figure 3.13: Similar to Figure 3.11, but using a 3D background model extracted from the CVM.

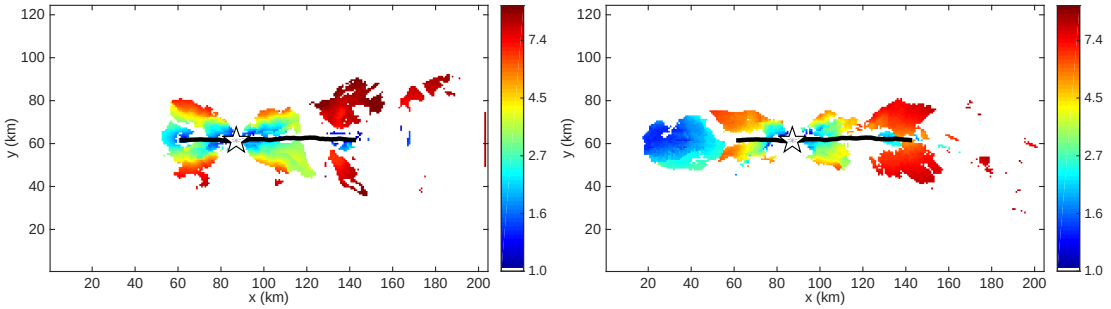

Figure 3.14: Regions where a directivity pulse occurs and its corresponding pulse period (s) for (left) 1D and (right) 3D background models.

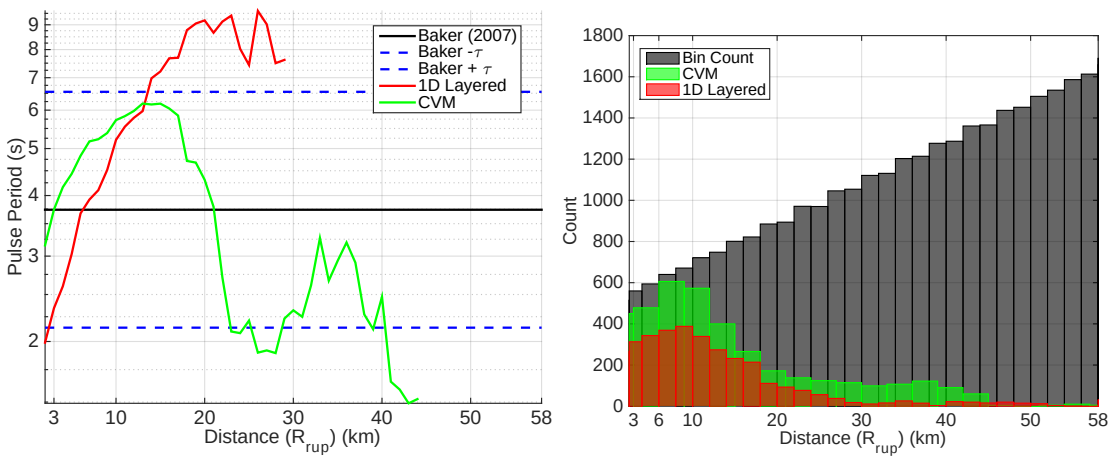

Figure 3.15: (Left) Pulse Period as a function of distance. (Right) Gray bins are the number of stations as each distance, with red and green colored bins the number of stations observed to have a pulse period.

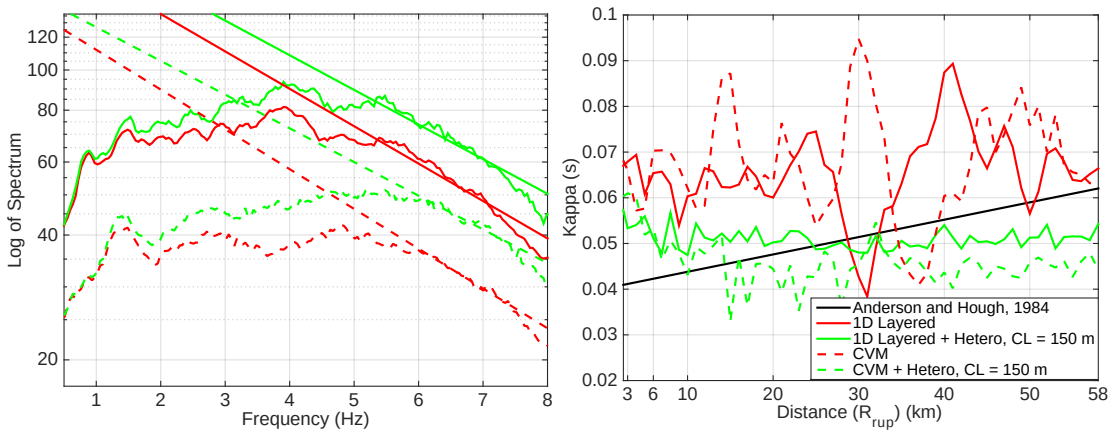

Figure 3.16: We calculate κ for both 1D and 3D background models, with and without heterogeneity over the relatively narrow bandwidth 5-7 Hz. (Left) Plot of stacked energy for stations at a distance of $r_{rup} = 5$km with corresponding sloping lines used to calculate κ. (Right) Plot of κ compared with the Anderson and Hough (1984) empirical relation for hard rock sites.

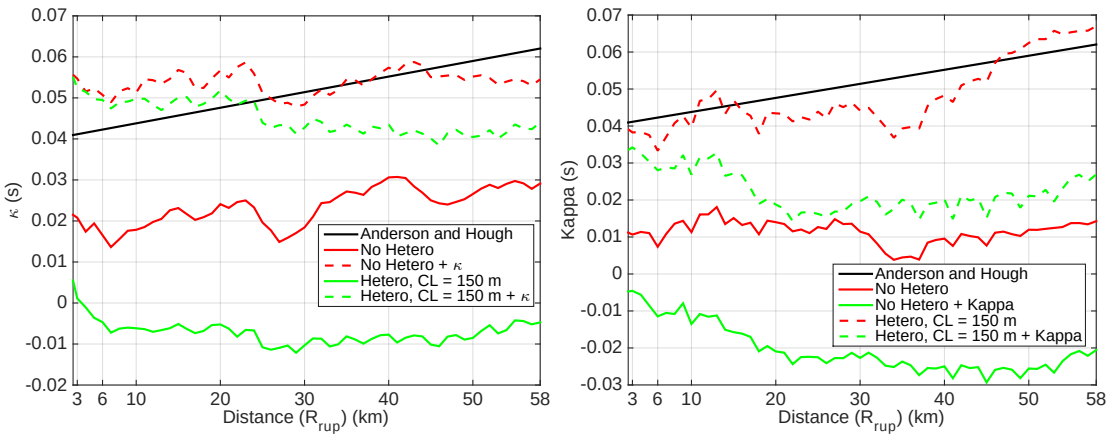

Figure 3.17: κ values calculated over the bandwidth 2-7 Hz, using the new approach, described in the text for (Left) 1D and (Right) 3D background models.

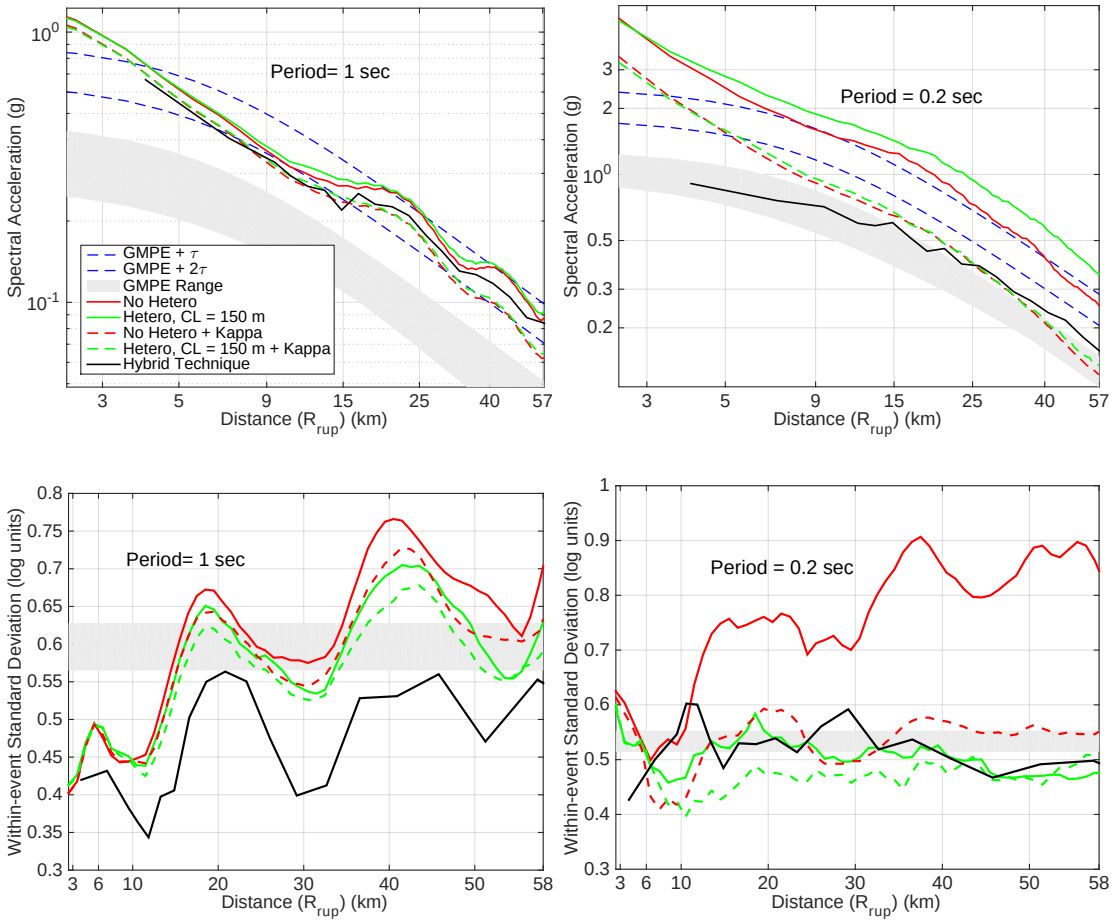

Figure 3.18: (Top) Spectral acceleration at a long and short period and (bottom) corresponding intraevent variability, using a 1D layered background velocity model. We also include the comparison with a hybrid broadband approach (SDSU) that is generated from the low-frequency deterministic synthetics.

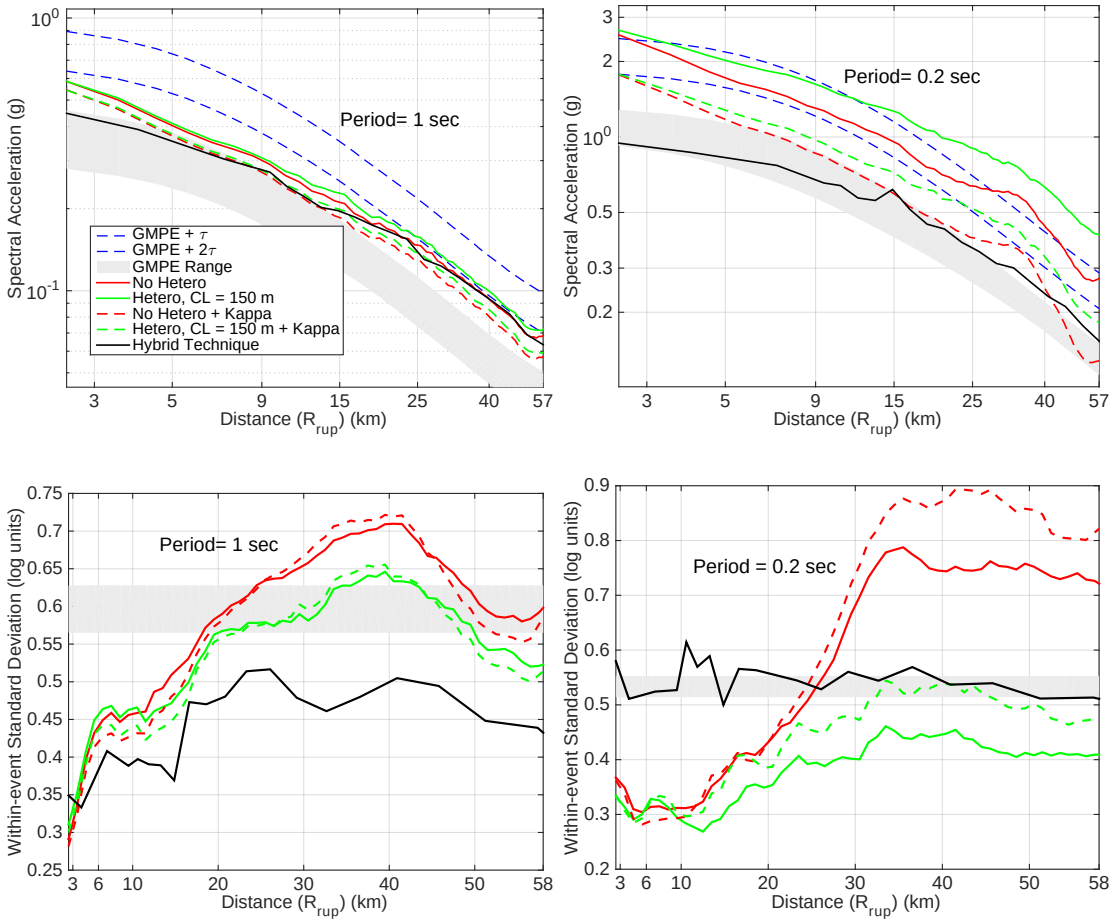

Figure 3.19: Same as Figure 3.18, but using a 3D background velocity model.

3.10 Author Addresses

Withers, K. B., San Diego State University, Dept. of Geol. Sci., 5500 Campanile Dr, San Diego, CA 92182 and University of California, San Diego, Institute of Geophysics and Planetary Physics, 9500 Gilman Dr, La Jolla, CA 92093, withers@rohan.sdsu.edu

OLSEN, K. B., San Diego State University, Dept. of Geol. Sci., 5500 Campanile Dr, San Diego, CA 92182, kbolsen@mail.sdsu.edu

DAY, S. M., San Diego State University, Dept. of Geol. Sci., 5500 Campanile Dr, San Diego, CA 92182, sday@mail.sdsu.edu

3.11 Appendix

3.11.A Verification of the Two-step Procedure

Here, we compare the accuracy of the two-step procedure, using the slip-rate time series and normal vectors output from SORD to convert to a moment-rate time-series for each subfault as the input into AWP. Figure 3.A.1 compares the SORD and AWP seismograms and frequency, using > 10 points per wavelength for both AWP and SORD approaches (SORD requires at least this value for accurate wave propagation). We used the Kristekova et al. (2009) approach (a time-frequency representation) to calculate the envelope and phase misfit between our models. Envelope misfit (EM) and phase misfit (PM) in the bandwidth $0.2-10$ Hz are within 5% and 2%, respectively, and the corresponding goodness-of-fit values are above 9 in the scale used in Kristekova et al. (2009), classified as an excellent fit. This demonstrates that the 2-step procedure for the dynamic-kinematic simulations has sufficient accuracy for our purposes here.

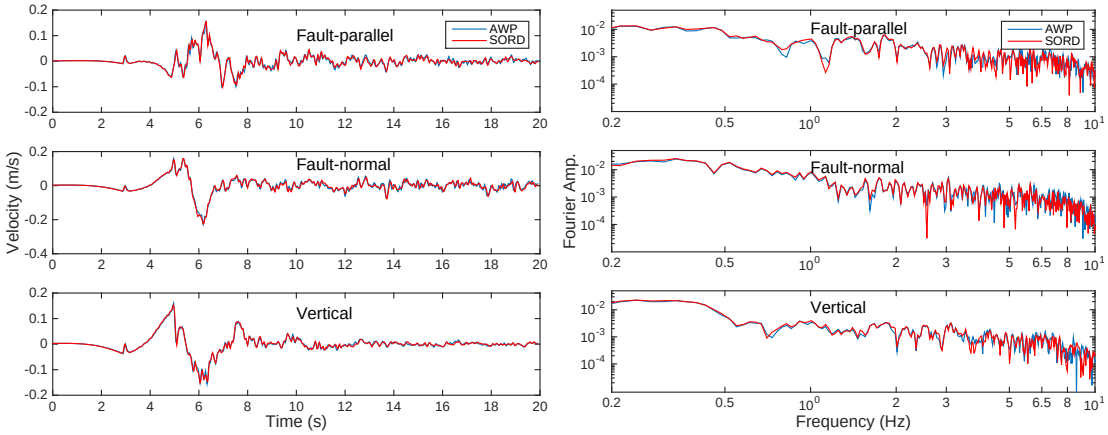

Figure 3.A.1: (a) Comparison of fits obtained between dynamic and wave-propagation codes, SORD and AWP respectively, for (a) 3-component time-series low-passed to 10 Hz and (b) Fourier spectra. This station is 9 km along the fault-parallel direction and 9 km perpendicular from the hypocenter in an elastic homogeneous background model.

3.11.B Accuracy of Small-scale Heterogeneity Implementation

With the continued movement towards higher resolution and modeling of higher frequencies, it is important to verify that the accuracy of 3D simulations is still acceptable. Galis et al. (2013) found that similarities decrease with frequency and epicentral distance between several codes, including AWP. They found that significant variability in both phase and amplitude as the standard deviation of velocity perturbations increase, suggesting that the numerical representation of material heterogeneity in different codes exerts non-neglible effects on ground motion simulations in heterogenous media. Here, we compare our staggered-grid finite-difference wave-propagation code (AWP) with that of a semi-analytical technique (FK) (Zhu and Rivera, 2002) and a summation by parts approach (SW4) that uses local material properties, where unlike with staggered grid methods, no averaging is required (Sjögreen and Petersson, 2012). We start with simple models (homogenous and layered velocity structures) to develop a baseline value for the fits, and move toward a fully 3D model including small-scale heterogeneity. We analyze ground motion that extends up to 7-8 Hz (depending on the minimum shear wave velocity) and compare synthetic waveforms at a station at 25 km from the source. We design our simulation domain to be sufficiently large to have minimal reflections from the boundary during the simulated time.

We use a double-couple point source equivalent to right-lateral slip with a strike = 90°, dip = 90°, and rake = 0° at a depth of 1.8 km, using the cosine-bell moment-rate function:

$$\dot{M}(t) = \begin{cases} M_0(1 - \cos(2\pi t/T) & 0 < t < T \\ 0 & \text{otherwise} \end{cases}, \tag{3.3}$$

with $T = 0.2$ sec and $M_0 = 10^{16}$ N m, equating to a $M_w = 4.6$ earthquake. The source is averaged across two depth points in AWP, since the shear stress σ_{xy} in our scheme is located one-half grid point below the target grid location. As the horizontal components of the staggered-grid are located 1/2 point below the free surface, we also average the horizontal components of the receiver stations to be

closer to the target geometry (Gottschämmer and Olsen, 2001). Neither of these approaches need to be used in either SW4 or the FK technique, as they either interpolate the source or station location on the fly, or can compute the solution at the target location.

First, we compare the computed time histories obtained with a purely elastic (infinite Q) homogenous model to determine the accuracy of the FD solutions for the prescribed model parameters. Here we set v_p = 6000 m/s, v_s = 3464 m/s, and $\rho = 2700$ kg/m^3. For all models we use a vertical correlation length of 150 m and a Hurst exponent of 0.05. Figure 3.B.1 shows seismograms and the Fourier spectra for each component of a surface station located at a horizontal distance of 25 km from the source with an azimuth of 53.13° from North. The seismograms have been band-passed between 0.2 and 10 Hz using a fourth-order, zero-phase Butterworth filter. We used the time-frequency representations of misfit between two seismograms classified as envelope misfit (EM) and phase misfit (PM) as in Kristekova et al. (2009) to determine the fits quantitatively. Figure 3.B.2 compiles the results comparing the 3 models, showing that both the arrival times of all major phases are reproduced with phase error and peak amplitudes are matched with relative error less than 2%. Fourier spectral amplitudes are nearly identical in the two solutions. The Rayleigh wave (7-8.5 s, radial and vertical components), is free of visible spurious oscillations and reproduces the wavenumber-integration solution with considerable precision.

Next, we use the layered model profile plotted in Figure 3.1 as the medium and compare the seismograms in Figure 3.B.3. Figure 3.B.4 shows that the fits, again, are very good, with small values of misfit, even with the low velocity layers near the surface. The level of misfit is only significantly larger within the transverse component for AWP compared to the FK solution. Next, we use the same background layered velocity model, and superimpose small-scale heterogeneity, constrained to lie within only the vertical direction. This is done so that the FK solution can still be calculated, now complicated by heterogeneity at every depth point, and including narrow velocity inversions. Figure 3.B.5 shows that the seismograms are even more complicated, but the solutions are still very similar.

Figure 3.B.6 finds EM and PM values only slightly larger than that of a simple layered model. Finally, we include 3D small-scale heterogeneity, superimposed on a homogenous background model. We cannot compare with an analytical solution here, but since both SW4 and AWP had similar levels of fit in the simpler models, we deem it appropriate to compare them to one another as a proxy for solution accuracy. Figure 3.B.7 and 3.B.8 show the corresponding results, indicating very comparable fits, and EM and PM within a 6-7% level of agreement. Figure 3.B.9 and 3.B.10 plot the envelope and phase misfits, respectively, as a function of time and frequency. The misfit is only slightly larger than the values found in the simpler models, indicating that we are accurately modeling small-scale heterogeneity.

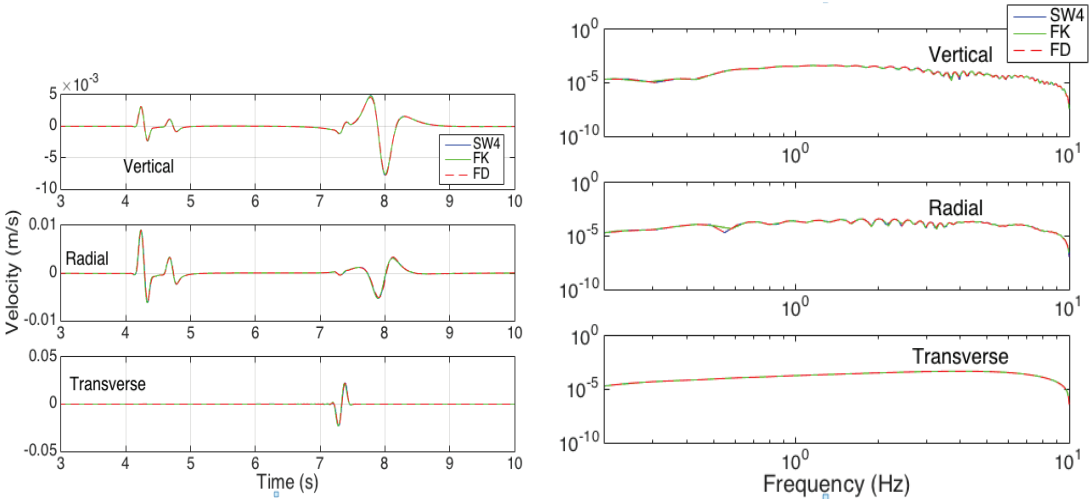

Figure 3.B.1: 3-component seismograms and spectra for a homogenous model comparing the FK, AWP, and SW4 approaches.

	FK vs. AWP		FK vs. SW4	
	EM	PM	EM	PM
Radial	1.41E-02	8.13E-03	8.27E-03	4.76E-03
Transverse	1.05E-02	8.31E-03	7.31E-03	5.72E-03
Vertical	1.35E-02	2.06E-02	1.83E-02	2.05E-02

Figure 3.B.2: Envelope and phase misfits for a homogenous model comparing the FK, AWP, and SW4 approaches, corresponding to Figure 3.B.1.

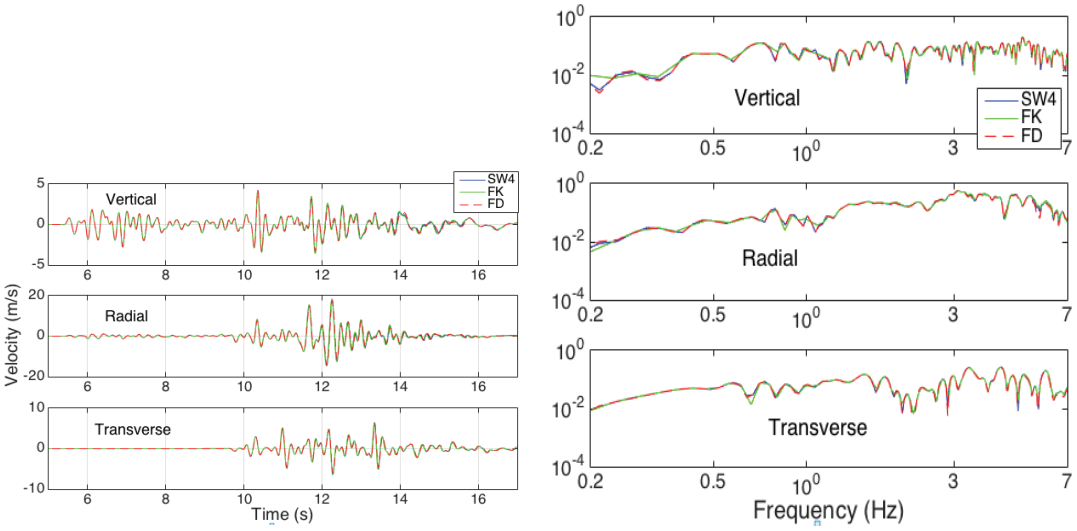

Figure 3.B.3: Same as Figure 3.B.1, but using a layered model plotted in Figure 3.1.

	FK vs. AWP		FK vs. SW4	
	EM	PM	EM	PM
Radial	1.73E-02	1.59E-02	7.10E-03	6.32E-03
Transverse	5.73E-02	4.75E-02	2.27E-02	2.35E-02
Vertical	1.89E-02	1.24E-02	5.82E-03	4.69E-03

Figure 3.B.4: Envelope and phase misfits for a layered model comparing the FK, AWP, and SW4 approaches, corresponding to Figure 3.B.3.

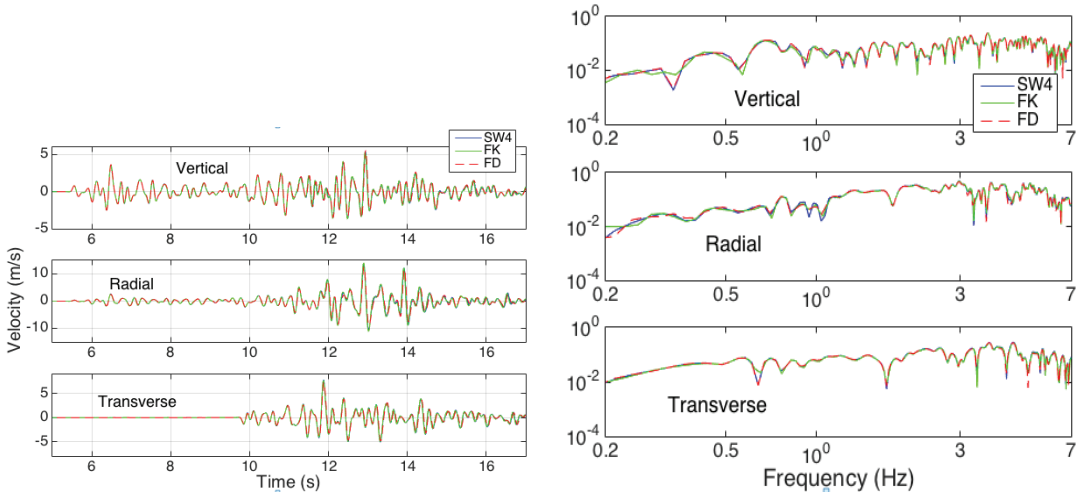

Figure 3.B.5: Same as Figure 3.B.1, but using a layered model with superimposed 1D (vertical) small-scale heterogeneity.

	FK vs. AWP		FK vs. SW4	
	EM	PM	EM	PM
Radial	2.54E-02	2.02E-02	1.11E-02	1.49E-02
Transverse	7.86E-02	5.07E-02	3.24E-02	4.21E-02
Vertical	2.93E-02	2.54E-02	7.87E-03	1.37E-02

Figure 3.B.6: Envelope and phase misfits for 1D (vertical) small-scale heterogeneity superimposed on a layered model comparing the FK, AWP, and SW4 approaches, corresponding to Figure 3.B.5.

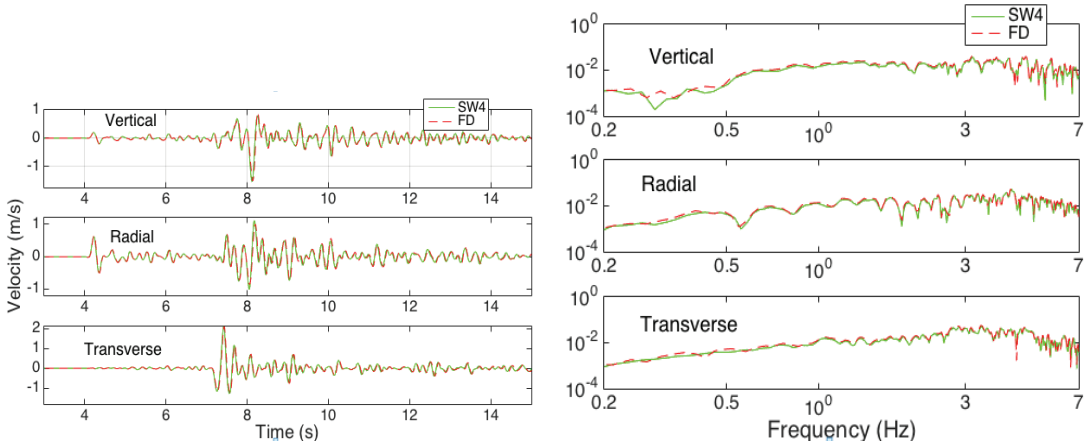

Figure 3.B.7: Same as Figure 3.B.1, but using a homogenous model with 3D small-scale heterogeneity superimposed, comparing just the AWP and SW4 techniques.

	AWP vs. SW4	
	EM	PM
Radial	6.34E-02	6.38E-02
Transverse	7.60E-02	6.08E-02
Vertical	5.65E-02	7.89E-02

Figure 3.B.8: Envelope and phase misfits for 3D small-scale heterogeneities superimposed on a background homogenous model comparing the FK, AWP, and SW4 approaches, corresponding to Figure 3.B.7.

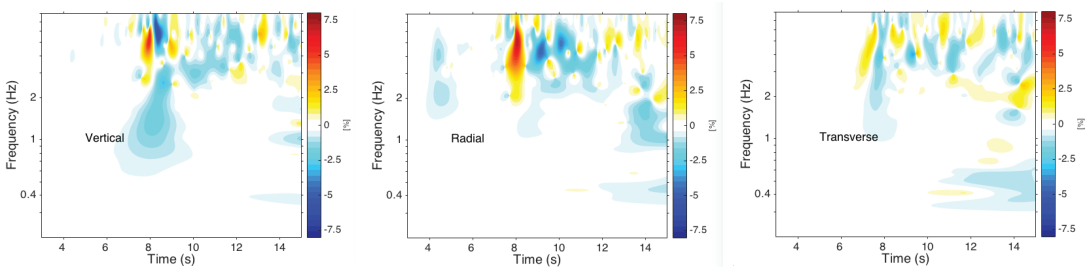

Figure 3.B.9: Envelope misfit plots for the 3D models shown in Figure 3.B.7.

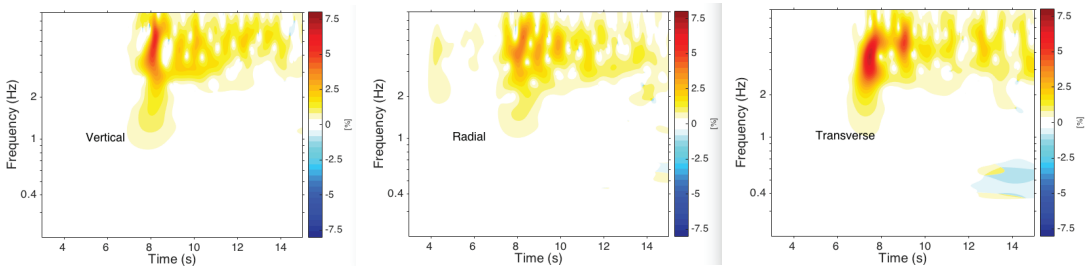

Figure 3.B.10: Phase misfit plots for the 3D models shown in Figure 3.B.7.

3.11.C Log-normality of Residuals

A common assumption in ground motion studies using empirical data is that the residuals follow a lognormal distribution. Intraevent residuals of spectral acceleration have been shown to follow a lognormal distribution, e.g. (Jayaram and Baker, 2008), using residuals from a large collection of earthquakes. Hartzell et al. (2010) found that their synthetic ground motion amplitudes followed a lognormal distribution very closely at low frequency. O'Connell (1999) showed that stochastic variation of velocity various in the upper curst can reproduce the observed lognormal dispersion of peak ground motions. In determining the coefficients of the GMPEs, the residuals (differences in logarithms) from the prediction are assumed to be normally distributed.

Several recent studies have found that both synthetic and empirical residuals are not distributed according to a lognormal distribution. For example,Yagoda-Biran and Anderson (2015) found that the deviations were in the central part of the distribution, where the effect on PSHA shouldn't be to large. Mcbean et al. (2015) also found that PGA and PGV from ruptures along a foam rubber stick-slip model do not following a log-normal PDF. They used the sum of multiple lognormal CDFS to model PGA and PGV.

Here we analyze the synthetic data to determine if the residuals follow a lognormal distribution, using just an individual event. After binning the stations as a function of distance, we calculate the intraevent logarithmic residuals from the median for each distance bin. By construction, the mean of each distrubution is zero. We use both histograms and q-q plots to determine the lognormality of the distribution. The q-q (or quantile-quantile) plot is obtained by plotting quantiles of the data set against the corresponding quantiles of a theoretical normal distribution. The data set follows a normal distribution if the normal q-q plot has a straight line with a slope of 45 degrees, passing through the origin. We also add on confidence bands to the q-q plot by using the Kolmogorov-Smirnov test for the null hypothesis, given the size of the data sample. A derivation in the q-q-plot outside this interval indicates a significant deviation from a normal distribution.

After grouping the bins together, we plot histograms and q-q plots that

compare quantiles to the standard normal distribution. Figure 3.C.1 shows this for a spectral acceleration of 3.33 Hz using the 1D layered model with small-scale heterogeneity superimposed. The number of stations in the analysis used here was decimated for computational reasons by choosing a random selection of 50,000 stations. It is evident that the residuals do not closely follow a lognormal distribution, both by analyzing the histogram and the departure from the straight line in the q-q plot. The confidence bands show that it fails the KS test at the 95% confidence levels. We note that the inclusion of small-scale heterogeneity slightly increases the agreement with a log-normal distributution at spectral accelerations above 1 Hz.

Figure 3.C.2 plots the same quantities, but using the 3D CVM model including small-scale heterogeneity. We see that the distribution is very close to that of a lognormal distribution at 3-4 standard deviations, as well as lying within the 95% confidence bands. Values of 3 standard deviations and above has little effect on hazard curves for return periods generally used in engineering design or at the 10,000-year level employed in the nuclear industry (Huyse et al., 2010). It seems that the 3D background structure serves to redistribute the ground motion at both the low and the high frequencies (as seen in Figure 3.6). This may be due to both the reduction in polarization (as shown in Chapter 4) as well as the loss of coherence in the wave-guide effect from surface waves generated within the 1D layered velocity model.

Looking closer at Figure 3.C.1, and comparing with Figure 3.6, we observe that there appear to be two distinct zones of ground motion, showing up as two distributions within the histogram, and the departure from the mean value at the origin in the q-q plot. One way to characterize this would be with a mixture model, the sum of two normal distributions with different standard deviations. Previous models have derived amplification factors for ground motion metrics at low frequencies to explain this azimuthal dependency and distance dependence, related to the directivity (Somerville et al., 1997, Spudich et al., 2013). We use the Bayless and Somerville approach published within the PEER 2013 report using the specifics of our strike-slip fault and plot the directivity amplitude correction

factor in Figure 3.C.3. Values > 1 correspond to the region of forward directivity, and < 1, backward directivity. This shows a similar spatial pattern to that observed in Figure 3.6. We hypothesize that if we ran a suite of ruptures, with varying hypocenter locations, that the directivity effect in 1D layered models would average out, and the residuals would more closely follow that of a lognormal distribution, as in Jayaram and Baker (2008). To test this, we separated the stations spatially into two groups: forward and backward directivity, corresponding to > 1 or < 1, respectively, as shown in Figure 3.C.3. Figure 3.C.4 plots the corresponding residual distribution in the backward directivity region, and Figure 3.C.5 the forward region, both using the 1D layered model. It is clear that both distributions are much closer to the lognormal distribution than in Figure 3.C.1, particularly for the backward directivity region. As more deterministic models are run in the future, it will be informative to see if the log-normal assumption holds, potentially important for determining if bias exists from statistical measures derived from 1D simulations at high frequencies.

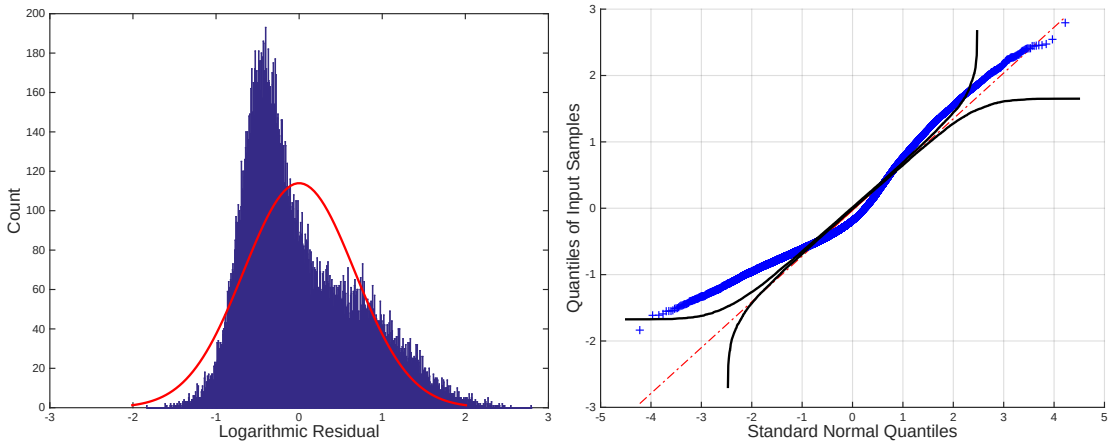

Figure 3.C.1: (Left) Histogram of spectral acceleration residuals at 3.33 Hz with corresponding normal distribution and (right) q-q plot for the 1D layered model with small-scale heterogeneity (5 % σ and $CL = 150$ m). The blue points map the normal distribution and the black lines show the 95% confidence interval of the normal distribution residuals given the size of the data sample.

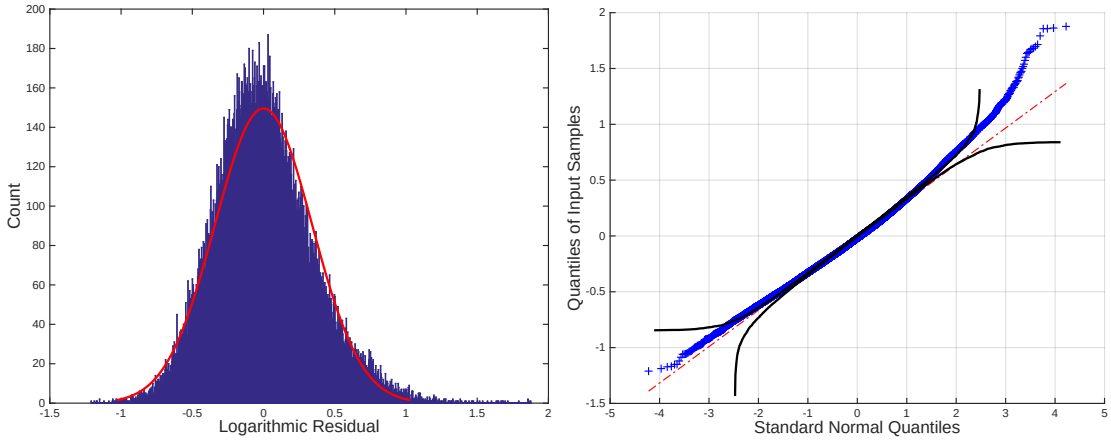

Figure 3.C.2: Same as Figure 3.C.1 but using a 3D background model with small-scale heterogeneity superimposed.

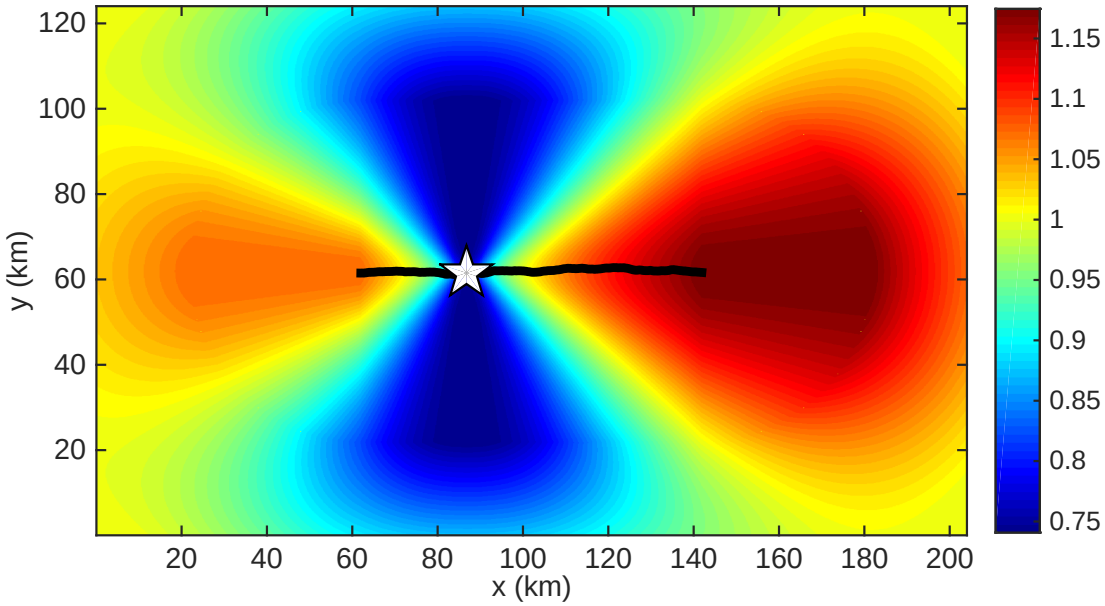

Figure 3.C.3: Directivity amplitude correction factor from Spudich et al. (2013) to distinguish regions of forward and backward directivity for the 1D layered strike-slip model.

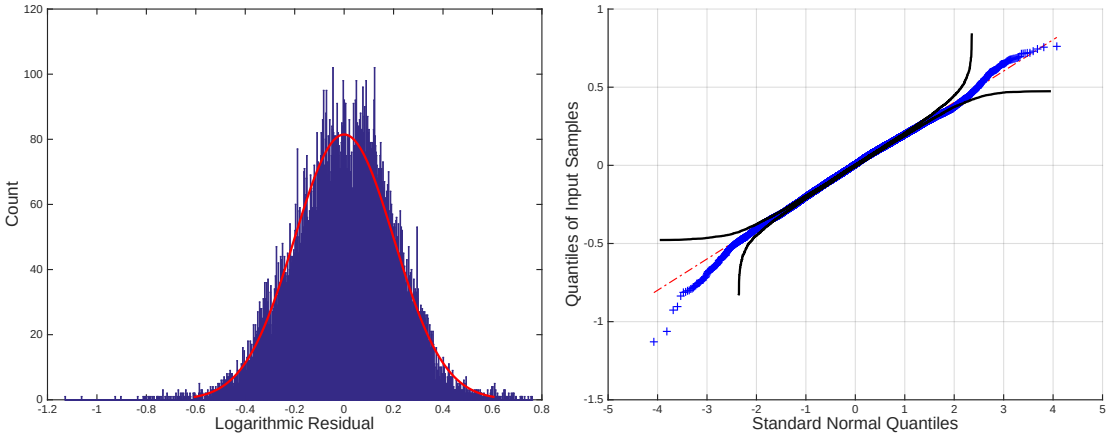

Figure 3.C.4: Same as Figure 3.C.1, but using only the stations located in the backward directivity regions.

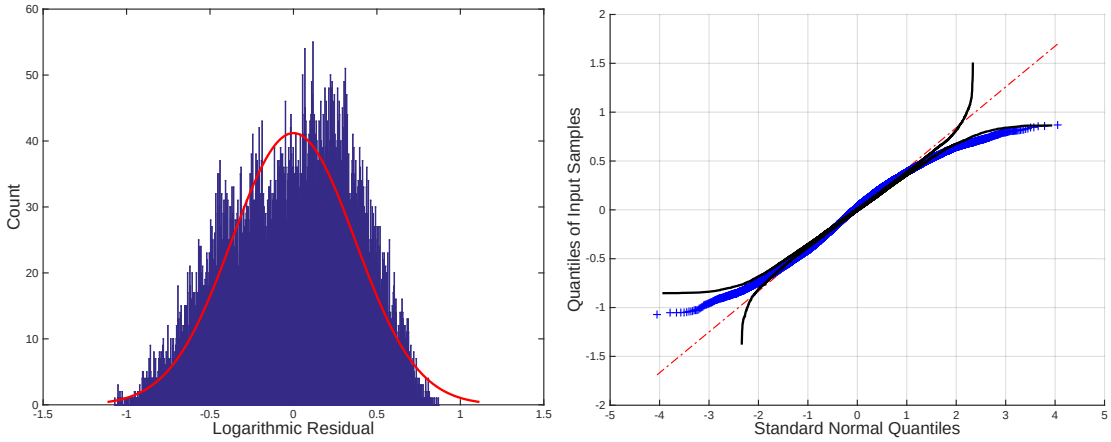

Figure 3.C.5: Same as Figure 3.C.1, but using only the stations located in the forward directivity regions.

3.12 References

References

Abercrombie, R. E. (1997). Near-Surface Attenuation and Site Effects from Comparison of Surface and Deep Borehole Recordings. *Bull. Seism. Soc. Am.*, **87**, 731–744.

Abrahamson, N. a., W. J. Silva, and R. Kamai (2014). Summary of the ASK14 Ground Motion Relation for Active Crustal Regions. *Earthquake Spectra*, **30**, 1025–1055. ISSN 8755-2930.

Afshari, K. and J. P. Stewart (2016). Physically Parameterized Prediction Equations for Significant Duration in Active Crustal Regions. *Earthquake Spectra*, **22**, 985–1003.

Anderson, J. and S. Hough (1984). A model for the shape of the fourier amplitude spectrum of acceleration at high frequencies. *Bull. Seism. Soc. Am.*, **74**, 1969–1993.

Anderson, J. G. (2015). The Composite Source Model for Broadband Simulations of Strong Ground Motions. *Seismological Research Letters*, **86**, 68–74.

Assimaki, D., W. Li, J. H. Steidl, and K. Tsuda (2008). Site Amplification and Attenuation via Downhole Array Seismogram Inversion: A Comparative Study of the 2003 Miyagi-Oki Aftershock Sequence. *Bull. Seism. Soc. Am.*, **98**, 301–330.

Atkinson, G. M. (2006). Single-Station Sigma. *Bull. Seism. Soc. Am.*, **96**, 446–455.

Atkinson, G. M. and K. Assatourians (2012). Implementation and Validation of EXSIM (A Stochastic Finite-Fault Ground-Motion Simulation Algorithm) on the SCEC Broadband Platform. *Seismological Research Letters*, **86**, 48–60.

Baker, J. W. (2007). Quantitative Classification of Near-Fault Ground Motions Using Wavelet Analysis. *Bull. Seism. Soc. Am.*, **97**, 1486–1501.

Ben-Zion, Y. and C. Sammis (2003). Characterization of fault zones. *Pure and Applied Geophysics*, **160**, 677–715.

Boore, D., J. Stewart, E. Seyhan, and G. Atkinson (2015). NGA-West 2 Equations for Predicting PGA, PGV, and 5%-Damped PSA for Shallow Crustal Earthquakes. *Earthquake Spectra*, **30**, 1057–1085.

Boore, D. M. (2006). Orientation-Independent Measures of Ground Motion. *Bull. Seism. Soc. Am.*, **96**, 1502–1511. ISSN 0037-1106.

Brune, J. N. (1996). Precariously Balanced Rocks and Ground-Motion Maps for Southern California. *Bull. Seism. Soc. Am.*, **86**, 43–54.

Bydlon, S. A. and E. M. Dunham (2015). Rupture dynamics and ground motions from earthquakes in 2-D heterogeneous media. *Geophys. Res. Lett.*, **42**, 1701–1709.

Campbell, K. and Y. Bozorgnia (2014). NGA-West2 Ground Motion Model for the Average Horizontal Components of PGA, PGV, and 5%-Damped Linear Acceleration Response Spectra. *Earthquake Spectra*, **30**, 1087–1115.

Chiou, B. and R. Youngs (2014). Update of the Chiou and Youngs NGA model for the average horizontal component of peak ground motion and response spectra. *Earthquake Spectra*, **30**, 1117–1153.

Crempien, J. G. F. and R. J. Archuleta (2015). UCSB Method for Simulation of Broadband Ground Motion from Kinematic Earthquake Sources. *Seismological Research Letters*, **86**, 61–67.

Cui, Y., E. Poyraz, K. B. Olsen, J. Zhou, K. Withers, S. Callaghan, J. Larkin, C. Guest, D. Choi, A. Chourasia, Z. Shi, S. M. Day, J. P. Maechling, and T. H. Jordan (2013). Physics-based Seismic Hazard Analysis on Petascale Heterogeneous Supercomputers. In *Procs. Supercomputing Conference*.

Day, S. M., L. A. Dalguer, and N. Lapusta (2005). Comparison of finite difference and boundary integral solutions to three-dimensional spontaneous rupture. *J. Geophys. Res.*, **110**, 1–23.

Day, S. M., R. Graves, J. Bielak, D. Dreger, S. Larsen, K. B. Olsen, A. Pitarka, and L. Ramirez-guzman (2008). Model for Basin Effects on Long-Period Response Spectra in Southern California. *Earthquake Spectra*, **24**, 257–277.

Dunham, E. M., D. Belanger, L. Cong, and J. E. Kozdon (2011). Earthquake Ruptures with Strongly Rate-Weakening Friction and Off-Fault Plasticity, Part 2: Nonplanar Faults. *Bull. Seism. Soc. Am.*, **101**, 2308–2322. ISSN 0037-1106.

Fehler, M., M. Hoshiba, H. Sato, and K. Obara (1992). Separation of scattering and intrinsic attenuation for the Kanto- Tokai region, Japan, using measurements of S-wave energy versus hypocentral distance. *Geophys. J. Int.*, **108**, 787–800.

Frankel, A. and R. W. Clayton (1986). Finite Difference Simulations of Seismic Scattering: Implications for the Propagation of Short-Period Seismic Waves in the Crust and Models of Crustal Heterogeneity. *J. Geophys. Res.*, **91**, 6465–6489.

Frankel, A. and L. Wennerberg (1987). Energy-flux model of seismic coda: separation of scattering and intrinsic attenuation. *Bull. Seism. Soc. Am.*, **77**, 1223–1251.

Galis, M., W. Imperatori, and P. M. Mai (2013). Quantitative analysis of accuracy of seismic wave-propagation codes in 3D random scattering media. In *European Geosciences Union General Assembly*, April, page 2013.

Gottschämmer, E. and K. Olsen (2001). Accuracy of the Explicit Planar Free-Surface Boundary Condition Implemented in a Fourth-Order Staggered-Grid Velocity-Stress Finite-Difference Scheme. *Bull. Seism. Soc. Am.*, **91**, 617–623.

Graves, R. (2016). Kinematic Ground Motion Simulations on Rough Faults Including Effects of 3D Stochastic Velocity Perturbations. *Bull. Seism. Soc. Am.*, **submitted**.

Graves, R., T. Jordan, S. Callaghan, E. Deelman, E. Field, G. Juve, C. Kesselman, P. Maechling, G. Mehta, K. Milner, D. Okaya, P. Small, , and K. Vahi (2010). CyberShake: A Physics-Based Seismic Hazard Model for Southern California. *Pure Appl. Geophys.*, **168**, 367–381.

Graves, R. and A. Pitarka (2015). Refinements to the Graves and Pitarka (2010) Broadband Ground-Motion Simulation Method. *Seismological Research Letters*, **86**, 75–80.

Hartzell, S., S. Harmsen, and A. Frankel (2010). Effects of 3D Random Correlated Velocity Perturbations on Predicted Ground Motions. *Bull. Seism. Soc. Am.*, **100**, 1415–1426. ISSN 0037-1106.

Hough, S., J. Anderson, J. Brune, F. Vernon, J. Berger, J. Fletcher, L. Haar, T. Hanks, and L. Baker (1988). Attenuation Near Anza California. *Bull. Seism. Soc. Am.*, **78**, 672–691.

Houtte, C. V., S. Drouet, and F. Cotton (2011). Analysis of the Origins of κ (Kappa) to Compute Hard Rock to Rock Adjustment Factors for GMPEs. *Bull. Seism. Soc. Am.*, **101**, 2926–2941.

Huyse, L., R. Chen, and J. A. Stamatakos (2010). Application of Generalized Pareto Distribution to Constrain Uncertainty in Peak Ground Accelerations. *Bull. Seism. Soc. Am.*, **100**, 87–101.

Imperatori, W. and P. M. Mai (2013). Broadband Near-Field Ground Motion Simulations in 3D Scattering Media. *Geophys. J. Int.*, **192**, 725–744.

Imtiaz, A., M. Causse, E. Chaljub, and F. Cotton (2015). Is Ground-Motion Variability Distance Dependent? Insight from Finite-Source Rupture Simulations. *Bull. Seism. Soc. Am.*, **105**.

Jayaram, N. and J. W. Baker (2008). Statistical Tests of the Joint Distribution of Spectral Acceleration Values. *Bull. Seism. Soc. Am.*, **98**, 2231–2243.

Jemberie, A. L. and A. A. Nyblade (2009). Intrinsic and Scattering Q near 1 Hz across the East African Plateau. *Bull. Seism. Soc. Am.*, **99**, 3516–3524.

Jin, A., K. Mayeda, D. Adams, and K. Aki (1994). Separation of intrinsic and scattering attenuation in southern California using TERRAscope data. *J. Geophys. Res.*, **99**, 17835–17848.

Kang, I. B. and G. A. McMechan (1994). Separation of intrinsic and scattering Q based on frequency-dependent amplitude ratios of transmitted waves. *J. Geophys. Res.*, **99**, 875–885.

Kohler, M. D., H. Magistrale, and R. W. Clayton (2003). Mantle Heterogeneities and the SCEC Reference Three-Dimensional Seismic Velocity Model Version 3. *Bull. Seism. Soc. Am.*, **93**, 757–774.

Korn, M. (1993). Determination of site-dependent scattering Q from P-wave coda analysis with an energy-flux model. *Geophys. J. Int.*, **113**, 54–72.

Kristekova, M., J. Kristek, and P. Moczo (2009). Time-frequency misfit and goodness-of-fit criteria for quantitative comparison of time signals. *J. Geophys.*, **178**, 813–825.

Ktenidou, O.-j., N. A. Abrahamson, S. . Drouet, and F. Cotton (2015). Understanding the physics of kappa (κ): insights from a downhole array. *Geophys. J. Int.*, **203**, 678–691.

Lin, P.-s., B. Chiou, N. Abrahamson, M. Walling, C. Lee, and C. Cheng (2011). Repeatable Source, Site, and Path Effects on the Standard Deviation for Empirical Ground-Motion Prediction Models. *Bull. Seism. Soc. Am.*, **101**, 2281–2295.

Magistrale, H., S. Day, R. W. Clayton, and R. Graves (2000). The SCEC Southern California Reference Three-Dimensional Seismic Velocity Model Version 2. *Bull. Seism. Soc. Am.*, **90**, 65–76.

Mai, M. and W. Imperatori (2015). The role of topography and lateral velocity heterogeneities on near-source scattering and ground-motion variability. *Bull. Seism. Soc. Am.*, **202**, 2163–2181.

Mai, P. M., W. Imperatori, and K. B. Olsen (2010). Hybrid Broadband Ground-Motion Simulations : Combining Long-Period Deterministic Synthetics with High-Frequency Multiple S-to-S Backscattering. *Bull. Seism. Soc. Am.*, **100**, 2124–2142.

Mayeda, K. and S. Koyanagai (1992). A Comparative Study of Scattering, Intrinsic, and Coda Q-1 for Hawaii, Long Valley, and Central California between 1.5 and 15.0 Hz. *J. Geophys. Res.*, **97**, 6643–6659.

Mcbean, K. M., J. G. Anderson, J. N. Brune, and R. Anooshehpoor (2015). Statistics of Ground Motions in a Foam Rubber Model of a Strike-Slip Fault. *Bull. Seism. Soc. Am.*, **105**, 1456–1467.

Mena, B., P. M. Mai, K. B. Olsen, M. D. Purvance, and J. N. Brune (2010). Hybrid Broadband Ground-Motion Simulation Using Scattering Green s Functions : Application to Large-Magnitude Events. *Bull. Seism. Soc. Am.*, **100**, 2143–2162.

Nakata, N. and G. C. Beroza (2015). Stochastic characterization of mesoscale seismic velocity heterogeneity in Long Beach, California. *Geophys. J. Int.*, **203**, 2049–2054.

O'Connell, D. (1999). Replication of Apparent Nonlinear Seismic Response with Linear Wave Propagation Models. *Science*, **283**, 2045–50.

Olsen, K. and R. Takedatsu (2015). The SDSU Broadband Ground-Motion Generation Module BBtoolbox Version 1. 5. *Seismological Research Letters*, **86**, 81–88.

Parolai, S., D. Bindi, and M. Pilz (2015). k0: The role of Intrinsic and Scattering Attenuation. *Bull. Seism. Soc. Am.*, **105**, 2–5.

Parvez, I. M. A. P., A. N. U. P. K. S. Satar, M. M. Mridula, S. K. M. Mishra, and S. S. R. Rai (2008). Coda Q Estimates in the Andaman Islands Using Local Earthquakes. *Pure Appl. Geophys.*, **165**, 1861–1878.

Phillips, W. S., K. M. Mayeda, and L. Malagnini (2013). How to Invert Multi-Band, Regional Phase Amplitudes for 2-D Attenuation and Source Parameters: Tests Using the USArray. *Pure and Applied Geophysics*, **171**, 469–484. ISSN 0033-4553.

Power, W. and T. Tullis (1991). Euclidean and Fractal Models for the Description of Rock Surface Roughness. *J. Geophys.: Solid Earth*, **96**, 415–424.

Raoof, M., R. Herrmann, and L. Malagnini (1999). Attenuation and excitation of three-component ground motion in southern California. *Bull. Seism. Soc. Am.*, **89**, 888–902.

Renard, F., C. Voisin, D. Marsan, and J. Schmittbuhl (2006). High resolution 3D laser scanner measurements of a strike-slip fault quantify its morphological anisotropy at all scales. *Geophys. Res. Lett.*, **33**, L04305. ISSN 0094-8276.

Rodriguez-marek, A., F. Cotton, N. A. Abrahamson, S. Akkar, L. A. Atik, B. Edwards, G. A. Montalva, and H. M. Dawood (2013). A Model for Single-Station Standard Deviation Using Data from Various Tectonic Regions. *Bull. Seism. Soc. Am.*, **103**, 3149–3163.

Roten, D., Y. Cui, K. Olsen, K. Withers, W. Savran, P. Wang, and M. Dawei (2016). High-Frequency Nonlinear Earthquake Simulations on Petascale Heterogeneous Supercomputers. In *SC16*, pages 1–14. Salt Lake City.

Savran, W. H. and K. B. Olsen (2016). Model for small-scale crustal heterogeneity in Los Angeles basin based on inversion of sonic log data. *Geophys. J. Int.*, **205**, 856–863.

Shaw, J., T. Jordan, and A. Pleasch (2014). Toward implementation of a stochastic description of fine scale basin velocity structure in the SCEC Community Velocity Model (CVM-H). Technical report, Tech. Rep., SCEC report 14176.

Shi, Z. and S. M. Day (2013). Rupture dynamics and ground motion from 3-D rough-fault simulations. *J. Geophys.: Solid Earth*, **118**, 1122–1141. ISSN 21699313.

Sjögreen, B. and N. A. Petersson (2012). A Fourth Order Accurate Finite Difference Scheme for the Elastic Wave Equation in Second Order Formulation. *J. Sc. Computing*, **52**, 17–48.

Somerville, P. G., N. F. Smith, R. W. Graves, and N. A. Abrahamson (1997). Modification of Empirical Strong Ground Motion Attenuation Relations to Include the Amplitude and Duration Effects of Rupture Directivity. *Seismological Research Letters*, **68**, 199–222.

Spudich, P., J. Bayless, J. Baker, B. Chiou, B. Rowshandel, S. Shahi, and P. Somerville (2013). Final Report of the NGA-West2 Directivity Working Group. Technical report.

Taborda, R. and J. Bielak (2014). Ground-Motion Simulation and Validation of the 2008 Chino Hills, California, Earthquake Using Different Velocity Models. *Bull. Seism. Soc. Am.*, **104**, 1876–1898. ISSN 0037-1106.

Taborda, R., K. Olsen, R. Graves, F. Silva, N. Khoshnevis, W. Savran, D. Roten, Z. Shi, C. Goulet, J. Bielak, P. Maechling, Y. Cui, and T. Jordan (2016). Verification and Validation of High-Frequency (fmax = 5 Hz) Ground Motion Simulations of the 2014 M 5.1 La Habra, California, earthquake. In *SCEC Annual Meeting*. Palm Springs.

Takemura, S. and T. Furumura (2013). Scattering of high-frequency P wavefield derived by dense Hi-net array observations in Japan and computer simulations of seismic wave propagations. *Geophys. J. Int.*, **193**, 421–436.

Takemura, S., T. Furumura, and T. Maeda (2015). Scattering of high-frequency seismic waves caused by irregular surface topography and small-scale velocity inhomogeneity. *Geophys. J. Int.*, **201**, 459–474.

Takemura, S., T. Furumura, and T. Saito (2009). Distortion of the apparent S -wave radiation pattern in the high-frequency wavefield: Tottori-Ken Seibu, Japan, earthquake of 2000. *Geophys. J. Int.*, **178**, 950–961.

Villani, M. and N. A. Abrahamson (2015). Repeatable Site and Path Effects on the Ground-Motion Sigma Based on Empirical Data from Southern California and Simulated Waveforms from the CyberShake Platform. *Bull. Seism. Soc. Am.*, **105**, 2681–2695.

Vyas, C., P. M. Mai, and M. Galis (2016). Distance and Azimuthal Dependence of Ground-Motion Variability for Unilateral Strike-Slip Ruptures. *Bull. Seism. Soc. Am.*, **106**, 1584–1599.

Withers, K. B., K. B. Olsen, and S. M. Day (2015). Memory-Efficient Simulation of Frequency-Dependent Q. *Bull. Seism. Soc. Am.*, **105**, 3129–3142.

Yagoda-Biran, G. and J. G. Anderson (2015). Investigation of the Ground-Motion Variability Associated with Site Response for Sites with V S 30 over 500 m = s. *Bull. Seism. Soc. Am.*, **105**, 1011–1028.

Zeng, Y., K. Aki, and T.-l. Teng (1993). Mapping of the High-Frequency Source Radiation for the Loma Prieta Earthquake, California. *J. Geophys. Res.*, **98**, 11981–11993.

Zhu, L. and L. Rivera (2002). A note on the dynamic and static displacements from a point source in multilayered media. *Geophys. J. Int.*, **148**, 619–627. ISSN 0956540X.

Chapter 4

Validation of Deterministic Broadband (0-8 Hz) Ground Motion and Variability from Ensemble Simulations of Buried Thrust Earthquakes

4.1 Abstract

We numerically model broadband ground motion (< 7.5 Hz) from blind thrust scenario earthquakes matching the fault geometry of the 1994 Mw 6.7 Northridge earthquake. Several realizations are modeled by varying the hypocenter location to generate an ensemble of earthquakes and investigate the variability and characteristics of the ground motion up to 50 km from the fault. We compare with that of ground motion prediction equations, simple proxy metrics, as well as strong ground motion records. Our models include small-scale medium complexity, Q(f), as well as nonlinear effects by incorporating Drucker-Prager plasticity, and using both a 1D layered and a 3D CVM as the background medium. We find that ground motion generally lies within 1 interevent standard deviation from

the median GMPEs and is strongly affected by nonlinear effects in regions of low shear wave velocity. As a result, intraevent variability is significantly reduced at distances near the source and above > 0.5 Hz. We find that both heterogeneity on the regional and small-scale is needed to match proxy metrics, such as the correlation of spectral acceleration with period, and ratio of maximum-to-median spectral acceleration. Small-scale heterogeneity has a negligible effect on spectral accelerations, but significantly increases the cumulative absolute velocity, better agreeing with observations. Additionally, we find our deterministic simulations have similar bias when comparing with strong motion data from the Northridge earthquake, and that 3D structure can have a large impact at both short and long periods. We also compare our synthetic ground motion at both footwall and hanging wall sites, but find no clear dependence on R_x.

4.2 Introduction

Earthquake simulations have become quite accurate at modeling ground motion at low frequencies, up to 1 Hz or so (e.g. Olsen, 2000; Roten et al., 2011). Only recently has there been the computational ability to deterministically model ground motion at significant distances from the source at higher frequencies. The importance is due to the fact that a building's response is related to its height; a rough approximation is 0.1 second period per individual story. Thus, it is extremely important to model earthquake ground motion prediction at the higher frequencies, to determine the seismic hazard for short buildings ($<$ 10 stories) and other structures. To extend ground motion simulation to higher frequencies, the source and medium need to be modeled in a realistic way. Here, we do this by incorporating small-scale fault geometry and media complexity, as well as frequency-dependent anelastic attenuation in deterministic earthquake models. In addition, we incorporate nonlinear effects via Drucker-Prager plasticity.

We previously modeled the ground motion experienced from 3D simulations incorporating rough-fault topography along a generic strike-slip fault (Chapter 3). Here, we use a similar approach to study a blind-thrust fault with dimensions modeled off that of the 1994 Mw 6.7 Northridge earthquake. We use moment-rate time-series derived from dynamic rupture models simulated using the support operator method (SORD) as the kinematic source in a finite difference anelastic wave propagation code (AWP-ODC) with Q(f). We model several realizations of buried thrust faults with similar moment magnitudes by varying the hypocenter location. We analyze the ground motion and intraevent variability influenced by scattering and nonlinear effects up to 50 km from the fault. These simulations are performed in both a 1D layered model characteristic of a southern California rock site and a 3D medium extracted from the Southern California Earthquake Center (SCEC) Community Velocity Model (CVM) version 4.0 including a surface geotechnical layer (GTL). We validate our simulations with empirical observations such as Next Generation Attenuation relations (GMPEs), simple proxy metrics, as well as strong-motion data from the Northridge earthquake up to 7.5 Hz.

4.3 Background

The 1994 Northridge reverse-faulting event struck San Fernando valley, about 20 miles northwest of downtown Los Angeles, 17 January, 1994, and was the most costly American earthquake since 1906. The mainshock was 30 km West-Northwest of downtown Los Angeles at a focal depth of 19 km, beginning at the southeastern corner of a dipping fault plane and rupturing up to the Northwest for about 15 km. It experienced 3 meters of reverse slip along a concealed thrust fault, with the maximum slip occurring $5 - 10$ km Northwest of the hypocenter, with an estimated seismic moment of $1.2 \pm 0.2\ 10^{19}$ Nm corresponding to Mw 6.7, with about 10-20 seconds of duration. The ground motion experienced large shaking, with the ground acceleration being one of the highest ever instrumentally recorded in an urban area of North America (1.8 g), and had large directivity updip towards the North. It was a particularly well-recorded earthquake with near-field stations on both hard-rock and soft-soil sites, including ones experiencing deamplification at sediment sites.

Ground motion prediction equations (GMPEs) provide the foundation on which seismic design and construction of the built environments rests, as well as seismic safety. There are sparse ground motion data for Mw > 6.7 earthquakes on reverse faults. To supplement empirical observations, simulations provide an approach to study certain features, that may be rarely observed, due to lack of data and spatial coverage. Before simulations can be used for engineering applications, validation is required to demonstrate that simulations have similar characteristics to real ground motions. This requires that simulations agree with preexisting relations, in terms of both their median and variability behavior, both as a function of distance and frequency. The simulations in this study are not meant to give the all possible ground motion by trying every permutation of parameters, but rather to highlight the range of behavior that is experienced by including different components that can become important at frequencies > 1 Hz.

In addition, there are a group of proxy metrics outlined in Burks and Baker (2014) that are relatively stable for many recorded ground motions. They have been shown to have little variation in model predictions across a range of tec-

tonic regimes, magnitude, distance, and site conditions, and among models from multiple regions or data sets. One of these is $SA_{RotD100}/SA_{RotD50}$, the ratio of maximum to median spectral acceleration measured across period. This is a measure of the amplitude polarization and is consistent for both dip-slip and strike-slip earthquakes. Another complementary proxy metric is ϵ, the correlation of spectral acceleration residuals at varying periods. It is defined as the normalized difference between an observed spectral acceleration and the mean predicted natural log of spectral acceleration from a GMPE. Baker and Jayaram (2008) looked at spectral acceleration values at multiple periods and orientations. They fit the NGA ground motion database for $\epsilon(T)$ at differing periods, using the Pearson product-moment correlation coefficient, finding that intraevent residuals have essentially identical correlation structure to the total residuals. This correlation, ρ, is related to the width of peaks and troughs in the spectra, and has been shown to be very consistent in the frequency range $0.3 - 10$ Hz (there are fewer records at longer periods).

4.4 Method

4.4.1 Dynamic Simulations

We dynamically model the source based on parameters pf the 1994 Mw 6.7 Northridge earthquake using the Support Operator Rupture Dynamics (SORD) code up to 8 Hz. The rupture geometry is specified in Figure 4.1. Following Wald et al. (1996), the dimensions of the fault follow that of the Northridge rupture: a width of 17.5 km and down-dip length of 24.5 km, with a strike of 122 and dip of 40 degrees. The fault is composed of 1.7 million subfaults that follow a self-similar fractal distribution from wavelengths of 80 meters up to the length of the fault, similar to the method in Shi and Day (2013). It used an average rake of 105 degrees with the depth to top of the rupture of 5 km. This was run in a characteristic hard rock site profile, similar to Chapter 3.

We model additional realizations of dip-slip scenarios by varying the hypocenter location and fault topography to generate an ensemble of earthquakes. The

hypocenter locations are varied and selected from plausible nucleation points on the fault, at depths near the base of the fault. Figure 4.2 plots the final slip for the three rupture models, and Figure 4.3 shows the three hypocenter locations and corresponding peak slip rates. We will refer to these throughout the chapter as Events 1, 2, and 3.

4.4.2 Kinematic Simulations

We use the slip-rates from the dynamic simulations and convert them to double-couple point sources to generate broadband moment-rate time series for input into our wave-propagation code, AWP-ODC. This allows an extension of ground motion to much further distances from the fault because of the increased computationally efficiency. Additionally, we can include complexities within the media that currently SORD doesn't support. More details about this approach are discussed in Chapter 3. Figure 4.A.1 shows a figure of the comparison of the wave-propagation between SORD and AWP, showing that this technique remains accurate for a dipping fault and layered velocity structure. Figure 4.4 plots the model domain chosen for this study, including nearby strong ground motion stations located within and near the study area.

We ran simulations in both 1D and 3D background velocity models both with and without small-scale medium complexity, with varying statistical parameters, based on the approach outlined in Chapter 3. Figure 4.5 plots an example of the media heterogeneity at the surface for one choice of a random seed for the background 1D-layered model, using a grid spacing of 20 m. We simulate 100-140 s (depending on the velocity model) of ground motion and store time series over a regular grid of points on the free surface at a resolution of 80 m. Our 3D background velocity models are extracted from the CVMSi.426, where the 3D velocity structure of the Los Angeles basin is relatively well known. In geotechnical engineering, it is generally accepted that the major part of ground-shaking is related to the upward propagating body waves, because of the bending of seismic rays towards the surface. We ran tests with and without a geotechnical layer (GTL), and found that the GTL significantly increased the ground motion response outside valleys

and basins with respect to the original CVMSi4.26 model, due to the reduction in otherwise unrealistic high velocities. Figure 4.6 plots the shear-wave structure at the surface with and without the superposition of small-scale media heterogeneity for the 3D model including the GTL. We set the minimum shear velocity to 500 m/s, which allows analysis up to 5 Hz in our 3D models. We clamp the velocities after adding the heterogeneities; this produces a small bias in the heterogeneities to only be positive near the surface in the shear-wave velocity. However, this is not likely significantly affecting the ground motion, as it is typically only the top 1-2 grid points that are affected.

Roten et al. (2012) showed the overprediction of near-fault GMPE values is largely eliminated after a correction of the broadband synthetics for nonlinear soil effects is applied, reducing SAs from the simulations by up to 70%. Here, in addition to media complexity and anelastic attenuation structure, we run nonlinear simulations that include plasticity. Roten et al. (2014) found that larger strains induced by long-period waves emitted from the San Andreas Fault may give rise to nonlinear behavior from the shallow sedimentary rock underlying the basins. Recent simulations of the ShakeOut scenario for an elasto-plastic medium predict long-period ground motions that are $30 - 70\%$ lower compared to viscoelastic solutions in the Los Angeles Basin. This reduction probably becomes even more important at higher frequencies.

We combined our $Q(f)$ code (Withers et al., 2015) with that of a medium governed by Drucker-Prager plasticity (Roten et al., 2014) to obtain viscoelasto-plasticity, where yielding occurs in shear via a return map algorithm. The off-fault material responds elastically until stresses exceed a Drucker-Prager yield condition, after which viscoplastic deformation occurs. We included this as an additional component within our CVM simulations, assuming a NNE-SSW direction of the major principal stress for computation of the initial stress tensor (representative of regional stress fields in central and southern California) and assuming fluid pressure at all depths. This approach uses the Hoek-Brown criterion for fracture rock mass based on the Geological Strength Index (GSI), where we set the cohesion and friction angle values based on a sandstone. We store the quantity η which represents

the accumulated inelastic strain due to yielding.

4.5 Results

We validate our synthetic ground motion by first looking at spectral acceleration as a function of periods and cumulative absolute velocity, comparing with with that of GMPEs derived from empirical observations. We then investigate the consistency of our simulations compared with that of simple proxy metrics, to highlight the importance of different components within our models. Finally, even though our simulations are not designed to fit the specific slip asperities of the Northridge earthquake, we compare our forward simulations to strong ground motion records.

4.5.1 Spectral Acceleration

We extract spectral acceleration medians and variability information from leading recent Next Generation Attenuation (NGA) West 2 relations (Abrahamson et al., 2014; Boore et al., 2015; Chiou and Youngs, 2014; Campbell and Bozorgnia, 2014) for both 1D and 3D background velocity models. The most important factor controlling the amount of strong shaking in one event is the distance of the site from the fault plane. Different GMPE models rely on one or more parameters used to describe this, to name a few: r_{rup}, the closest distance to rupture plane, r_x, the horizontal distance to top of rupture, and r_{JB}, the horizontal distance to the surface projection of the rupture. We calculate these parameters, in addition to the others needed for the GMPE relations, at a resolution of a 80 m grid in our model. The averaged value for the 4 GMPEs is plotted in Figure 4.7 for both a 1D and 3D background model for a spectral acceleration at a period of 0.3 s. The Boore et al. (2015) model is only dependent on the Joyner-Boore distance, so it is symmetric about the projection of the fault rupture plane. The other models are dependent on r_{rup} and r_x, so they have more asymmetric patterns, with higher responses towards the upper region of the simulation domain.

Next, we analyze the ground motion from simulations for each hypocenter

location. Figure 4.8 plots the GMRotD50 (Boore, 2006) at a period of 0.3 s for all three hypocenter locations as well as their average using 1D layered models, both with and without small-scale heterogeneity. We have set $Q_{s0} = v_s * 0.05$ and $Q_{p0} = 2 * Q_{s0}$, where v_s is in m/s, and a $Q(f)$ model with a power-law exponent of 0.8, with a transition frequency of 1 Hz, as deemed appropriate in Chapter 3 for Southern California. We use a vertical correlation length of 150, Hurst exponent of 0.05, horizontal to vertical stretching factor or 5, and a $\sigma = 5\%$. It is evident that there are some qualitative similarities to the spatial patterns in Figure 4.7, but significant differences as well. It is clear that because the hypocenters are located at depth, there is significantly larger ground motion updip, peaked near the intersection of the projection of the fault to the surface. This is not too surprising, as the 1D models don't include the 3D long wavelength structure that can serve to break up the directivity at high frequencies. This is analyzed further in the Discussion, as a function of R_x, the distance perpendicular to strike. There are differences between the three hypocenter locations, particularly evident in the favored direction of ground motion. For example, Event 1, with a hypocenter location in the bottom-right corner of the fault has strong amplitude directed up dip and left of the fault, while the opposite pattern is evident for Event 2 with a hypocenter located in the bottom-left corner. The average of the three models smooths out some of the peaks and troughs observed in the spatial patterns. Presumably, if hypocenters were distributed more equally along the fault, ground motion patterns would be similar to Figure 4.7. The addition of small-scale heterogeneity serves to redistribute the energy on the local scale, shifting regions of low and high ground motion. This is in contrast to the bilateral strike-slip event, seen in Chapter 3, due to the style of faulting. Here, the rupture propagates updip to the surface with a shorter path (and thus scattering plays less of a role) and is distributed in narrow lobes around the fault.

We ran multiple simulations with varying correlation lengths for each model. Some of these simulations are highlighted in Figure 4.9, where we compare the ground motion in a quantitative way by analyzing spectral acceleration and intraevent variability for three distance bins within our model. We have chosen to

use R_{rup} to group stations as a function of distance from the fault, as it is a better predictor of the ground motion and allows for more variability near the fault (R_{rup} and r_x allowing for more asymmetric patterns) than the r_{JB} distance (which is symmetric about the projection to the surface of the fault rupture plane). The average ± 1 interevent standard deviations are included as well, by using the range of GMPEs as the median ground motion. We plot each event separately, to isolate the influence of including multiple rupture models. We find that the median ground motion changes very little across all rupture models, with and without small-scale media heterogeneity, with the exception of some small differences at high frequencies farthest from the fault. Any features that are noticed on the spatial maps plotted in Figure 4.8 are lost here when binning multiple stations together as a function of distance. As mentioned in Chapter 3 adjusting for V_{s30} values when adding in heterogeneity makes almost no difference when binning a large number of stations, as we do here. We note that the simulated SAs are generally within one standard deviation from those predicted by the NGA relations, and are generally within the variability of the 4 GMPE medians. The power-law exponent of 0.8 performs well, as the level of ground motion is fairly constant across period and the distance range studied here. The largest deviation from the GMPE trends is seen at the higher periods, in the range of $3-10$ seconds, but this is also the region where there are few observational constraints for dip-slip ruptures.

We see that the variability is fairly constant between events for distances near the source, but increases at larger distances. Event 1 has variability very near that of the GMPE range as a function of period, and only a slight reduction at larger distances when including small-scale heterogeneity. The correlation length has only a limited effect on both the ground motion or variability, becoming most significant above 1 Hz. Events 2 and 3 have reduced variability at the larger distances, lower than that of the empirical observations. This is as expected from Figure 4.7, where there is much smaller ground motion in the lower-right corner of the model domain for Event 1, causing the variability at that range of R_{up} to be higher than that of Events 2 and 3. The average of the three simulations is somewhat lower than predicted by the GMPEs; this could be partly due to the

simplified velocity structure used in a 1D layered model, where we expect similar values to single-station standard deviation.

Next, we compare ground motion from a medium including a 3D velocity structure extracted from the CVM as the background velocity model. Figure 4.10 plots the spectral acceleration at 0.3 s for Event 1, comparing models with and without small-scale media heterogeneity, as well as plasticity. It is seen that a much more complex pattern of ground motion is generated form the 3D background structure, which causes additional scattering and distribution of seismic waves. It is evident that ground motion is still favorably generated towards the top-left corner of the model. Reduced source directivity is evident, along with likely basin-edge amplification. Figure 4.10 shows that heterogeneity slightly reduces the bands of energy located along velocity interfaces, and smears out energy across small spatial domains. We note that there are relatively large regions of high SA that are largely reduced when plastic effects are included, more similar to the level recorded in the event. Figure 4.11 plots the reduction in SA at 0.3 s experienced for a model with and without plasticity, showing that at this high frequency, ground motion is reduced by as much of 70%. This region is mainly in the area located near the surface projection of the fault, but also exits in a lobe extending perpendicular to the strike on the footwall. Comparing the reduction plots with the total accumulated strain also in Figure 4.11, points out the distance significance of models including plasticity. Permanent deformation decreases with increasing distance from the rupture. Even though there is still significant reduction at 30-40 km from the fault, there is little or no strain accumulation in these regions. This indicates that nonlinear effects on ground motion can cause significant reductions at distances beyond where ground motion is reduced directly due to damping.

Figure 4.12 plots results for models using the 3D background CVM, for stations located within the basin, defined as where the depth to $Z_{1.0}$ (the depth where V_s reaches 1 km/s) is less than 100 m. This results in a somewhat biased spatial pattern of stations, having more stations located on the hanging wall than the footwall (see Figure 4.6). Thus, even though ground motion is expected to be

higher because of low velocity sediments, the distinction between median ground motion is small, as seen from the ground motion pattern in Figure 4.10. We observe similar levels of median ground motion as compared to GMPEs, again with small-scale heterogeneity playing a small role. The biggest difference between models is at the closest distance, where nonlinear effects strongly reduce the ground motion, particularly at shorter periods, to lie within the median GMPE range. We can only look up to 5 Hz here, due to the accuracy of our finite difference algorithm based on the minimum shear wave velocity in our model. The differences between events are more noticeable at distances near the fault, where changes in the sources slip-rate patterns are more significant.

The variability in the 3D models has similar characteristics as seen in the 1D models: there is a reduction at shorter distances moving from shorter to longer periods, and Event 1 tends to have the highest variability at distances far from the source. A key feature to point out is that because of the reduced ground motion at distances near the fault with nonlinear models, the variability is significantly reduced, from above 0.8 logarithmic units, down to 0.5 and below. It is in this distance range that strong ground motion stations are lacking significant observations. Features such as this will become very important as simulations continue to advance and describe the predictable behavior of faulting.

Figure 4.13 plots median and variability as a function of period similar to Figure 4.12, but for rock sites, where $Z_{1.0} > 100$ m. We note the constant trend that the medians are slightly underpredicted at larger distances from the source. This is due to the spatial bias mentioned earlier, where there are fewer stations on the hanging wall where ground motion is lower. The variability remains near that of GMPEs, due to the large variation of points on the hanging wall and footwall of the fault.

4.5.2 Cumulative Absolute Velocity

Looking at metrics besides spectral acceleration can emphasize different components both in terms of median values and variability levels. Here we choose the cumulative absolute velocity (CAV), defined as the integral of the absolute

value of the acceleration time series, as a metric to compare with ground motion data. Campbell and Bozorgnia (2012) developed a GMPE for both Arias Intensity (AI) and CAV, based on their previous 2008 GMPE model form. CAV includes the cumulative effects of ground motion duration, and has a smaller standard deviation than AI due to the difference in the square rather than absolute value of acceleration, thus having a higher predictability (Campbell and Bozorgnia, 2010). The model takes into account amplification due to basin structure; here we compute the geometric mean of the two as-recorded horizontal components of the synthetic simulations, and compare with the GMPE model predictions. Figure 4.14 plots CAV for 1D-layered model medians and variability. It is evident that models without small-scale heterogeneity underpredict the GMPE models, here by over two interevent standard deviations. This is because scattering greatly increases the energy in the later parts of the time series at high frequencies, which influences the acceleration. It is observed that the correlation length can have an impact on the level of CAV, with shorter values causing a higher median CAV. The best value for heterogeneity from this figure indicates that small-scale heterogeneity superimposed on a 1D layered velocity model performs best with a correlation length of 150 m. The variability is seen to be fairly similar between models with and without small-scale structure and different events, with the trend slowly increasing as a function of distance at a level below that of the empirical observations.

Figure 4.15 and 4.16 plots predicted and synthetic CAV for basin and rock sites, respectively, defined again based on $Z_{1.0}$. The 3D CVM structure has significantly increased the median values of CAV, and small-scale heterogeneity increases it even further. While plasticity decreases median values, incorporating both plasticity and small-scale heterogeneity is seen to best match the decay as a function of distance. There are no large clear systematic differences in the intraevent variability; it is seen to fluctuate around the expected range for basin sites, while being event-dependent for rock sites.

4.5.3 $SA_{RotD100}/SA_{RotD50}$

We analyze the ratio of maximum to median response across orientations for both 1D and 3D models, superimposing each component separately to determine its importance. Figure 4.17 plots both $SA_{RotD100}/SA_{RotD50}$ and its intraevent variability compared with the predicted values from Shahi and Baker (2014). It is seen that the median value for 1D models with no complexity is roughly constant, around a 1.32 ratio for the entire range of periods studied here. Adding in small-scale heterogeneity significantly reduces the short period range, above 2 s, but is still much larger than that of empirical observations. When using a 3D CVM, however, the 2-10 s period range lies right along that expected from data. Adding in small-scale heterogeneity further reduces the shorter periods into the expected range as well, indicating that both small-scale and large-scale media variation is needed to match that of this proxy metric. We found that 1D simulations with 1000m vertical and 5000 m horizontal correlation lengths did not reduce the ratio at longer periods, as the CVM model does here. The reason is likely that both sharp interfaces interacting with long wavelengths in the 3D background model, and statistical variations at shorter wavelengths combine to reduce the polarization of waves to be more equally distributed, reducing the ratio. It is seen that plasticity decreases the fit at short periods, but still lies within the expected range when small-wavelength heterogeneity is included.

We find that 1D models have lower variability than that expected from observations. 3D CVM simulations find better agreement with data, with little variations among different components included within the simulations. The results here are consistent across multiple source models, showing very little variation across the three events used in this study.

4.5.4 ϵ

Here we analyze another proxy metric, the correlation of ϵ across multiple periods, seen to be very stable for varying reference GMPEs. ϵ is defined as the normalized difference between an observed spectral acceleration and the mean predicted natural log of spectral acceleration of a GMPE. Here, between-event

variations average out because all ground motion is from the same event. Figure 4.18 plots ρ for both a long and short reference period. We analyze the results in the same progression as $SA_{RotD100}/SA_{RotD50}$, from 1D models up to more complicated 3D models. We find that at both short and long periods, the correlation in a narrow bandwidth is near that of predicted observations. As frequency increases from the reference frequency however, 1D models have significantly higher values of ρ than predicted. Moving to 3D models, we find that nearby frequencies now have reduced correlation, bringing them closer to observations. There is a large reduction in correlation when including small-scale heterogeneity. This is not surprising, as random velocity structure serve to rid neighboring frequencies of large correlations. The trends have an upward trend starting at about 3 s period, however, for a short reference period. This is likely due to the overlap of deterministic and stochastic structure thats needs to be more carefully defined, since the correlation agrees at the longer reference period. The correlation would likely reduce even further if lower values of velocity were included in the simulations, allowing more variation in the shear-wave velocity in the near surface.

4.5.5 Bias

We can also compare our synthetic results with that of observed ground motions for a specific event. Even though our simulation was not designed to match the Northridge earthquake specifically, there are many similarities that make it useful to compare the synthetics with the response spectrum of strong-motion data recorded within our model domain, corrected for the minimum V_s of 863 m/s. We used a scaling factor of 1.34 to decrease the size of Event 1 to that of the estimated moment of the Northridge earthquake (1.3 x 10^{19}Nm), and plot the psuedospectral acceleration bias versus distance for stations located within our model region, as shown in Figure 4.2. Figure 4.19 plots the bias (ln[data/model]), depicting the median, 95% confidence interval, and standard deviation for both 1D models with and without heterogeneity, and a 3D CVM model run with clamping performed at 863 m/s, to match the corrected data. We see that 1D layered models have positive residuals indicating an underprediction with respect to the empirical

model. The addition of small-scale heterogeneity makes little effect on the bias, but including 3D structure reduces this considerably, reducing the zero-bias level to lie within or near the $\pm$ 1 σ interval of the recorded motions. This potentially has important implications for the limitation of using 1D layered velocity models when trying to model specific earthquakes.

4.6 Discussion

The simulations along the blind thrust fault here represented only a small subset of potential rupture scenarios and velocity structures that need to be examined to more fully vet our approach. We found similar trends with period for the range of models used here, which is expected because they share common slip distributions, rupture areas, rupture speeds, and rise times. The interevent standard deviation of ground motion from the ensemble of earthquakes with different hypocenter locations here is very small, but will increase when using different rough fault topographies and a more distributed set of hypocenter locations. Additional dynamic rupture models should cover a range of different magnitudes and faulting mechanisms, as well as different fault topographies and varying hypocenter locations. These would help better determine the accuracy limit of high-frequency simulations, as well as the interevent variability of our models. A continued study to look into the significance of the $Q - Vs$ relation as well as the effect of media heterogeneity (varying the Hurst number and standard deviations) may be needed to help determine questions such as to whether σ is lower for soil rock sites. Deep soil sites are generally located in basins, and therefore 3D-geometric effects might be increasing the variability more than soil nonlinearity decreases it. It may be helpful to look at vertical components as well, which here are high or of similar amplitude to horizontal motion due to the motion from thrust-faulting scenarios.

4.6.1 R_x Dependence

Another aspect that can be continued to be studied is the hanging wall (HW) effect, where there is increased ground motion on the hanging wall side of

the rupture compared to the footwall (Donahue and Abrahamson, 2014). This is mainly a geometrical effect due to the closest distance metric, and was observed in the 1994 Northridge earthquake (Abrahamson and Somerville, 1996). Figure 4.20 plots GMPEs and synthetics for low and high frequency SA for both 1D and 3D models along a cross-section perpendicular to the strike, R_x, averaged along traces lying within the fault. R_x is the horizontal distance from the top of the rupture to the site, with positive values of R_x defined as on the hanging wall side. The hanging wall effect reaches the maximum value over the bottom edge of the rupture. Here the amplitude of the HW effect is smaller at $Z_{TOR} = 5$ km (depth to the top of the fault) than for a surface rupturing fault. We see that the ground motion predicted by GMPEs is sightly higher above $R_x = 0$ for both low and high frequencies. Our 1D layered synthetic simulations lie within the GMPE bounds for a period of 3s, but have a large pulse for 0.3 s in the $-5 - 0$ range of R_x, where the ground motion projects from the dipping fault to the surface. This feature was averaged out when looking at ground motion as a function of R_{rup} since the ground motion is lower for positive R_x. We see similar trends for the 3D CVM models, and note a significant reduction at higher frequencies when including plasticity. We don't see a strong characteristic hanging wall effect, as seen in the literature. More simulations should be performed to isolate whether this remains a consistent feature among rough-fault simulations.

4.7 Conclusions

We have modeled deterministic broadband ground motion along buried dip-slip events incorporating rough faults. We compared ground motions experienced in both 1D and 3D background models, including features such as small-scale media heterogeneity, plasticity via the Drucker-Prager yield condition, and frequency-dependent attenuation. For our models to be useful for engineering purposes, it is important that synthetic predictions match that of empirical observations. Here we found that that the spectral acceleration at various periods from our models match the distance decay similar to GMPEs. We observe that while the ground

motion pattern changes, the median ground motion is not affected significantly when including small-scale heterogeneity, when binned as a function of distance. We perform a parameter space study by varying statistical parameters and find that the variability is fairly independent of the correlation length. Heterogeneity serves to significantly increase the cumulative acceleration velocity, however, bringing it closer to that GMPEs, particularly when modeling 1D layered velocity models. We found that unconsolidated deposits may significant amplify the seismic ground motion during large earthquake, especially at higher frequencies ($>$ 1 Hz), and ignoring nonlinear effects could result in costly misguidance in earthquake-prone regions. Additionally, we compare several proxy metrics with our simulations using the ensemble average, and find that 3D heterogeneity at both the long and short scalelengths is necessary to agree with data. Specifically, small-scale media complexity decreases the polarization ratio and correlation across period to that of similar of observations, indicating the importance of including stochastic-based media heterogeneity as ground motion prediction extends to higher frequencies. These components should be included in future simulations to best model the ground motion from earthquakes. It is shown that broadband simulations are strongly influenced by source parameters such as the hypocenter, rupture diversity and extent; more simulations should be performed to determine the extent of predictability of strong ground motion for both specific and generic events.

4.8 Data and Resources

The southern California velocity model CVM-S 4.26 can be obtained from SCEC at http://scec.usc.edu/scecpedia/. Most of the data-processing work was done using MATLAB (http://www.mathworks.com/products/matlab/). Figures were prepared using MATLAB and the Generic Mapping Tools package (http://www.soest.hawaii.edu/gmt/). All electronic addresses referenced here were last accessed October 2014. All other data used in this paper came from published sources listed in the references.

4.9 Acknowledgments

This research was supported through the Southern California Earthquake Center (SCEC) by the NSF Cooperative Agreement EAR-0529922 and USGS Cooperative Agreement 07HQAG0008, by USGS award G15AP00077, and by NSF awards EAR-1135455, OCI-114849, EAR-1349180, and ACI-1450451. The simulations performed here were generated on the Titan Cray XK7 at the Oak Ridge Leadership Computing Facility in Tennessee.

Chapter 4, in full, is a reformatted version of a paper currently being prepared for submission for publication to *Bull. Seism. Soc. Am.*: Withers, K. K. Olsen, Z. Shi, and S. Day. Validation of Deterministic Broadband (0-8 Hz) Ground Motion and Variability from Ensemble Simulations of Buried Thrust Earthquakes. (2016). I was the primary investigator and author of this paper.

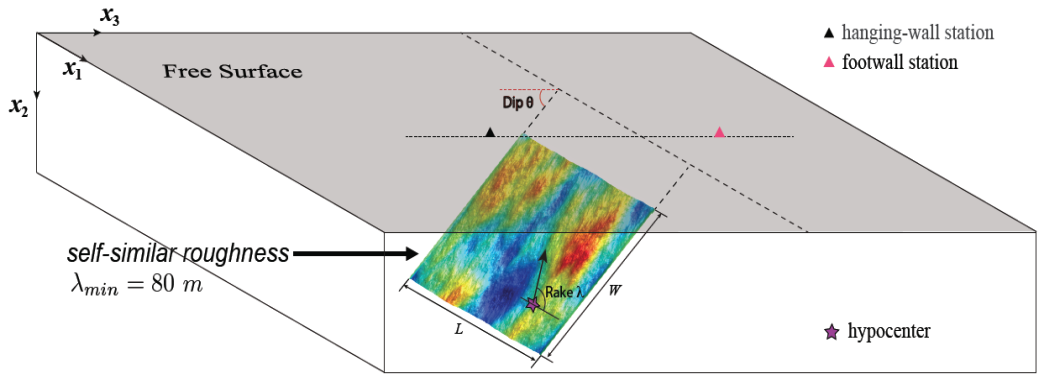

Figure 4.1: Rough fault geometry of dip-slip fault with complex geometry modeled off the dimensions of the 1994 Northridge earthquake.

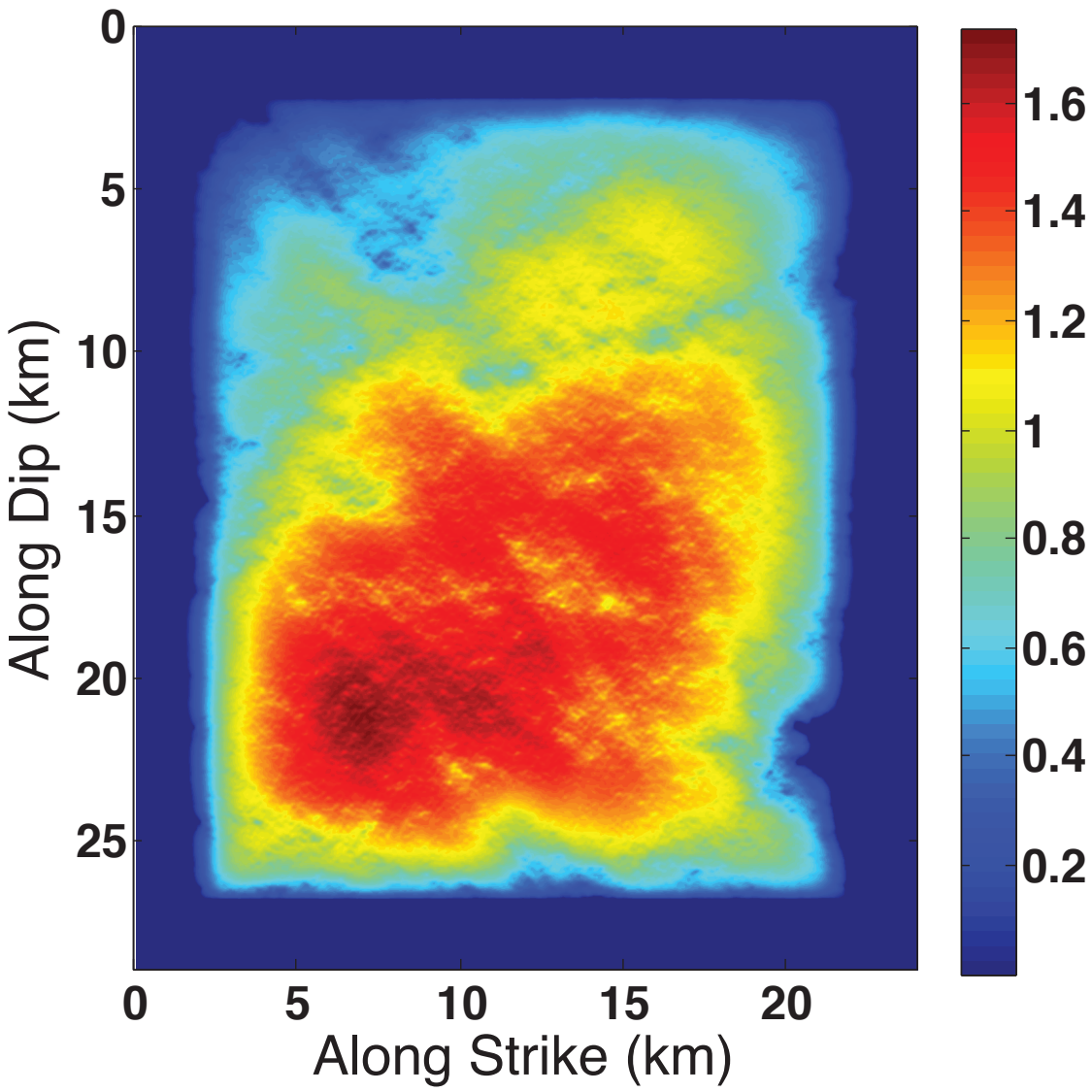

Figure 4.2: Final slip along the fault (m).

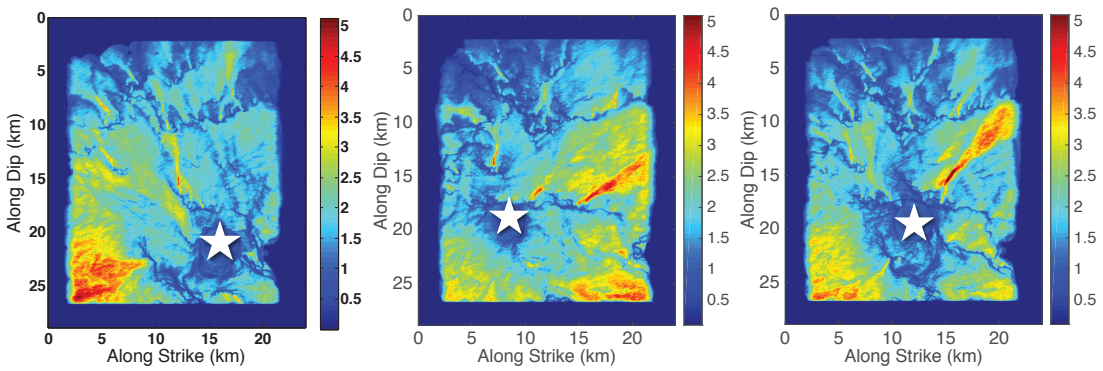

Figure 4.3: (Top) Maximum slip-rate (m/s) along the 3 different rupture models.

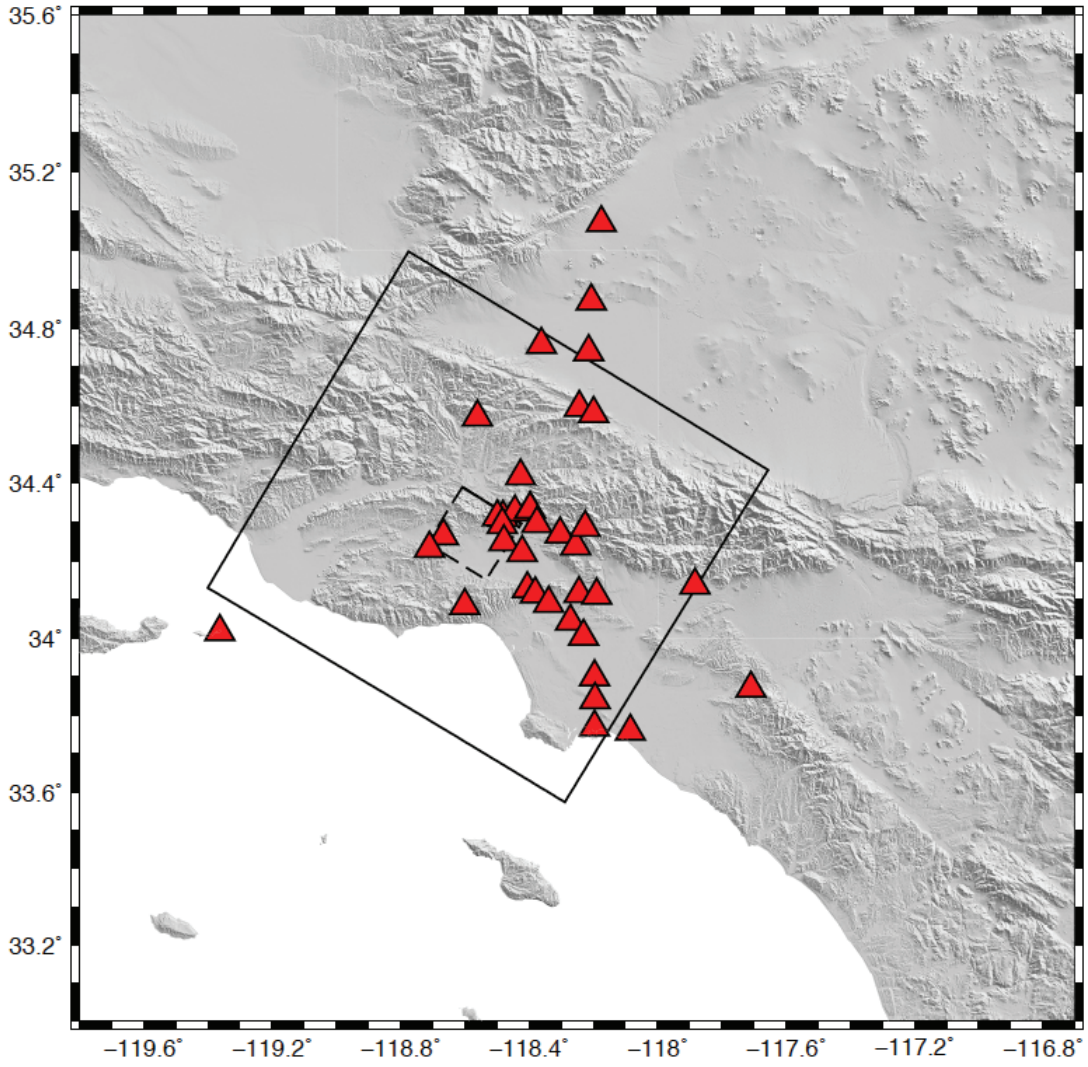

Figure 4.4: Simulation region location (large rectangle) with strong ground motion stations indicated by triangles. Small box indicates vertical projection of rupture plane to surface.

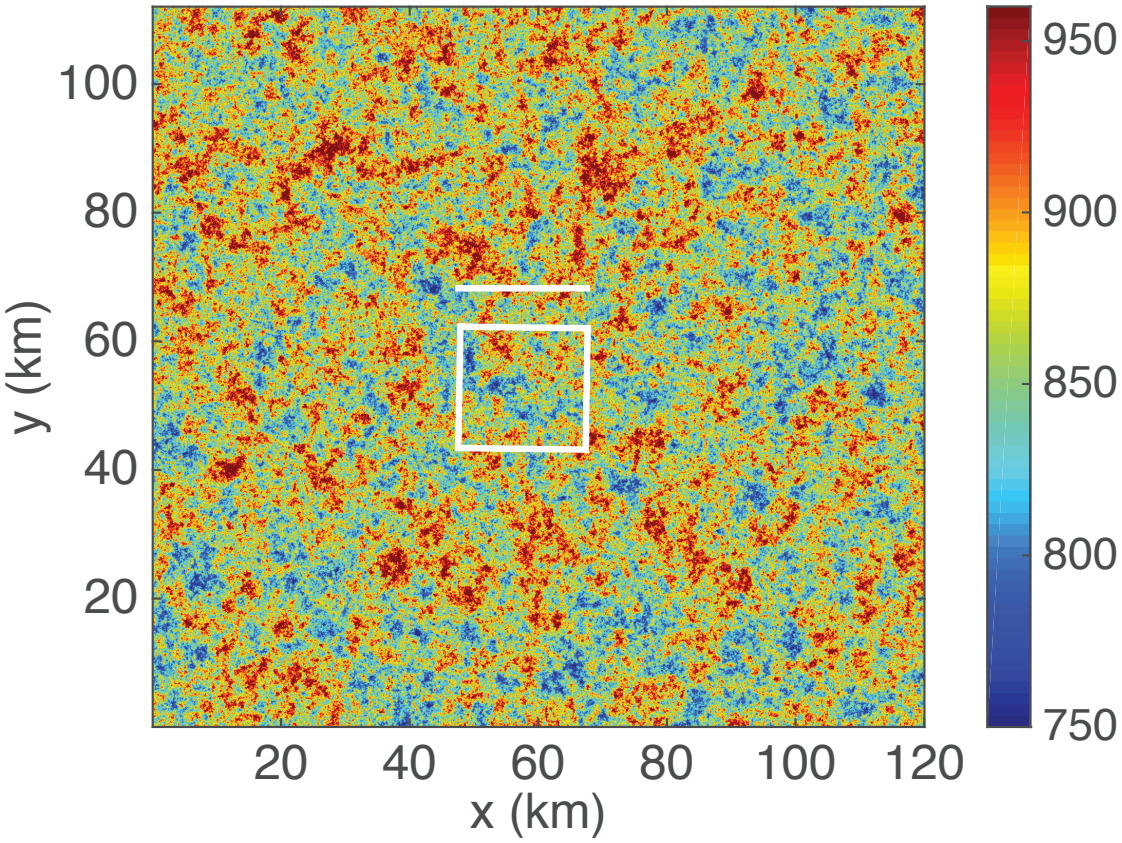

Figure 4.5: Plot of small-scale media heterogeneity of shear wave velocity at surface for a background velocity model with minimum V_s of 863 m/s. The correlation length = 150 m, with $H = 0.05$, and $\sigma = 5\%$.

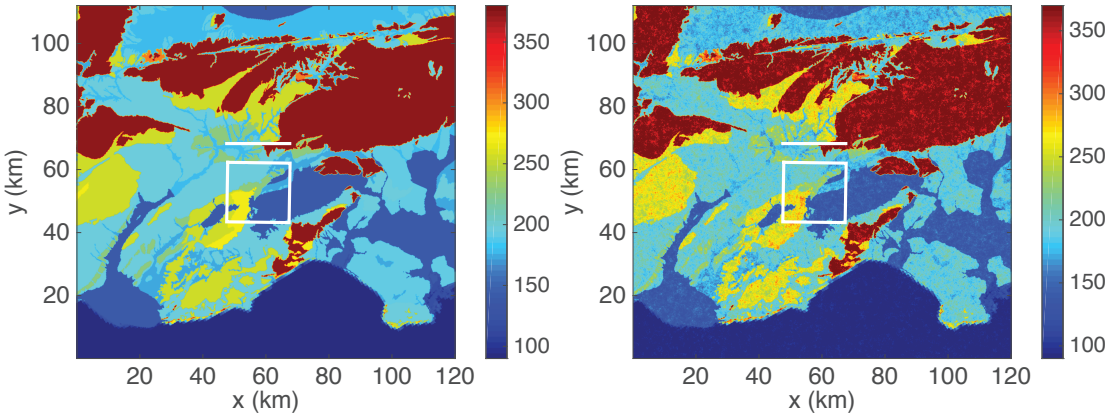

Figure 4.6: Map-view of shear wave velocity extracted from CVMSi.426, including a GTL layer (left) without and (right) with small-scale media heterogeneity.

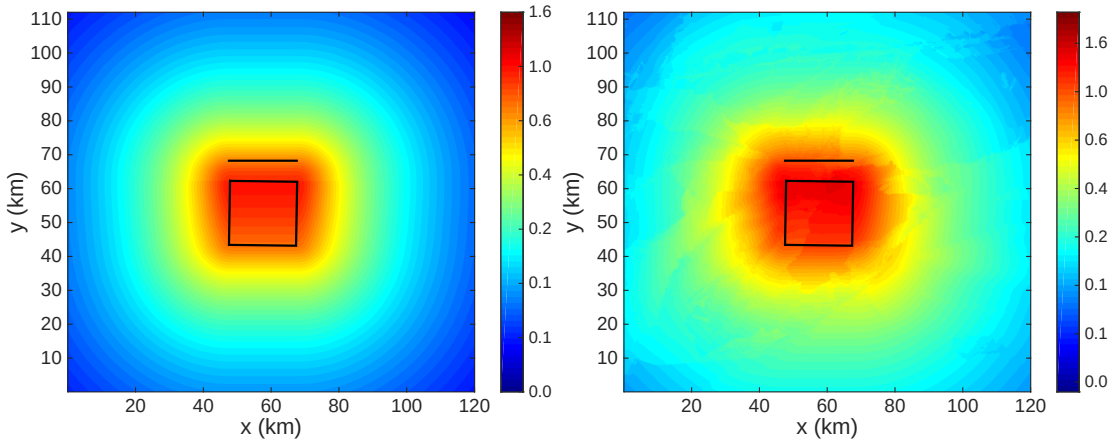

Figure 4.7: Average of 4 GMPE media predictions of SA(g) at a period of 0.3 s for (left) for 1D-layered model and (right) for the 3D CVM including a GTL layer.

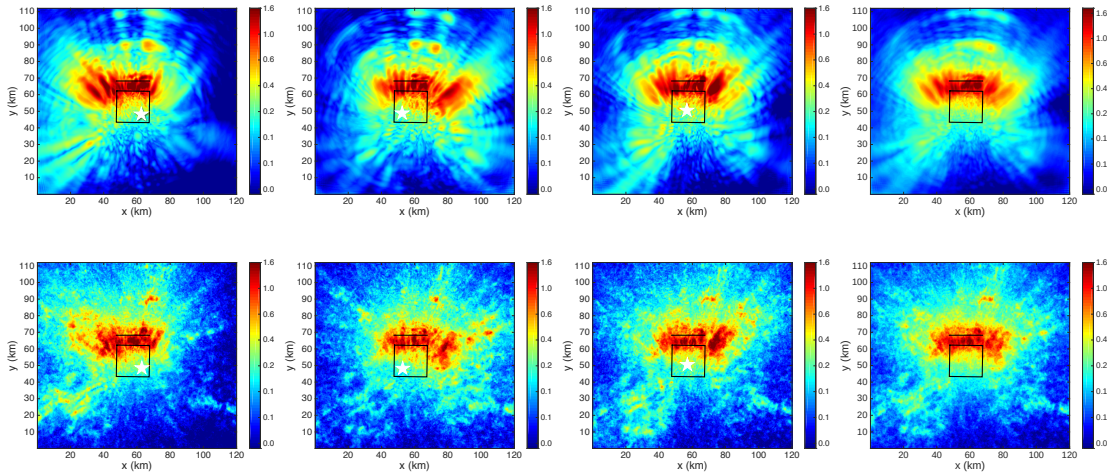

Figure 4.8: Spectral acceleration of $T = 0.3$ s in g for (top) models without small-scale heterogeneity, and (bottom) including small-scale heterogeneity. The left 3 columns indicate the three hypocenter locations as in Figure 4.4, with the rightmost column the average of the three.

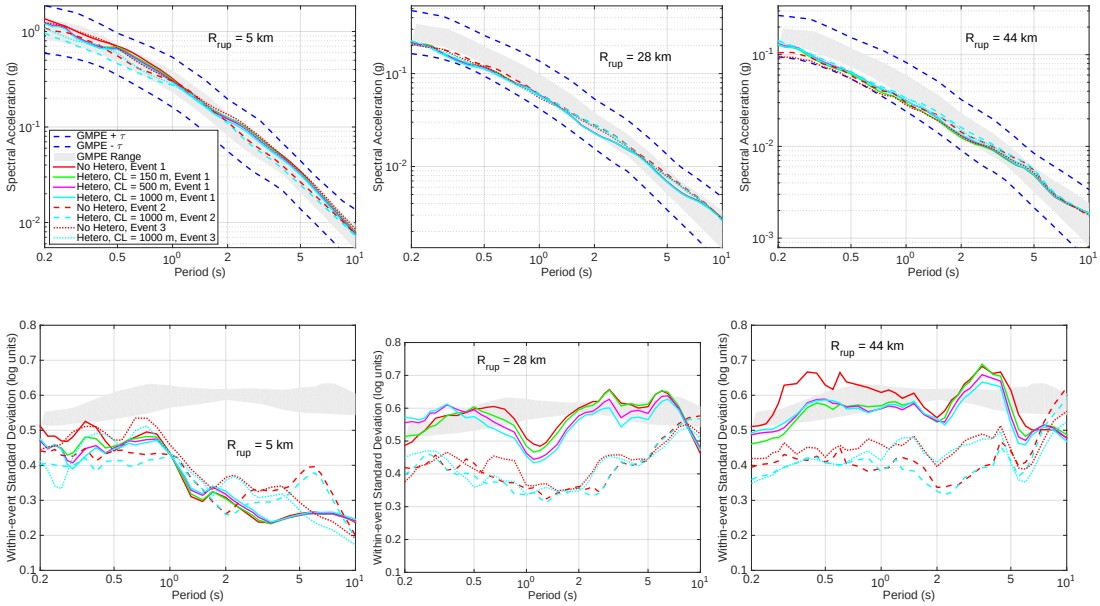

Figure 4.9: (Top) Median spectral acceleration and (bottom) intraevent variability as a function of period at a short, medium and far distance within our model domain. 'Hetero' refers to small-scale heterogeneity.

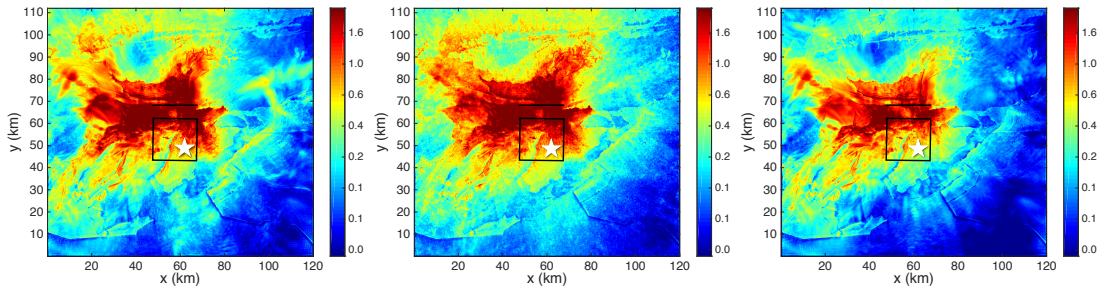

Figure 4.10: Spectral acceleration at 0.3 s (g) for a background CVM model (left) without small-scale heterogeneity, (middle) including small-scale heterogeneity, and (right) including both plasticity and small-scale heterogeneity.

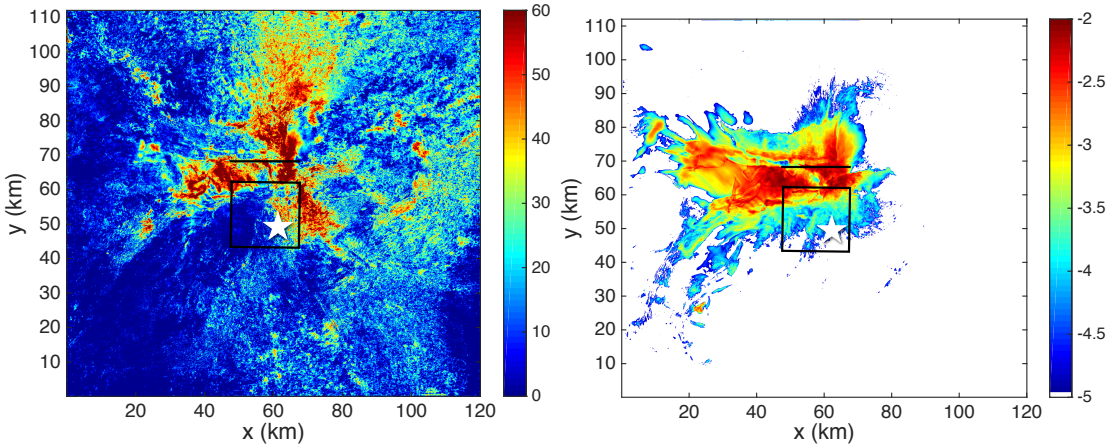

Figure 4.11: (Left) Reduction of SA % at 0.3 s for Event 1 when including plasticity within the model. (Right) Final principal plastic strain η at the surface (log units) corresponding to Event 1 plotted in Figure 4.10. The rectangle and line depict the surface projection of the fault plane and the projection of the fault to the surface, respectively.

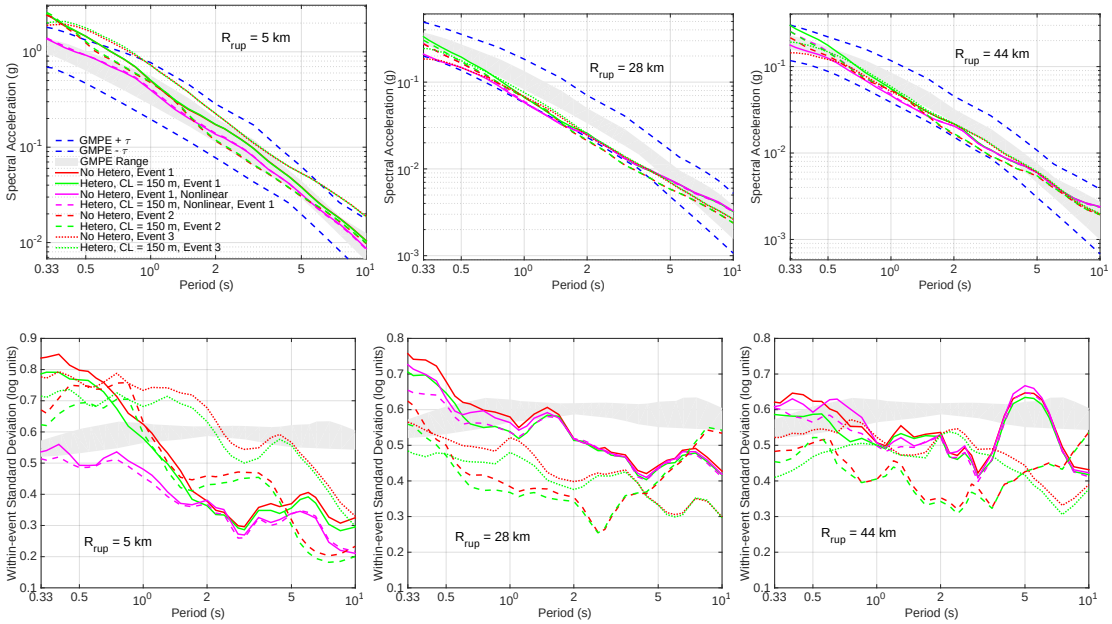

Figure 4.12: Similar to Figure 4.8, but using a 3D model with stations located in the basin.

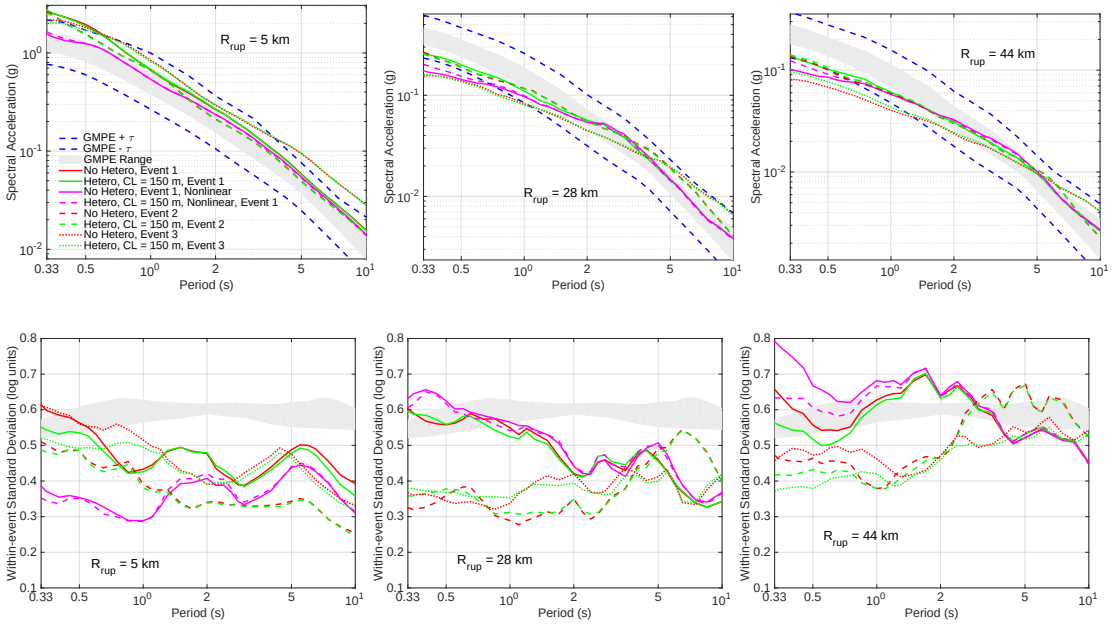

Figure 4.13: Same as Figure 4.12, but for rock sites.

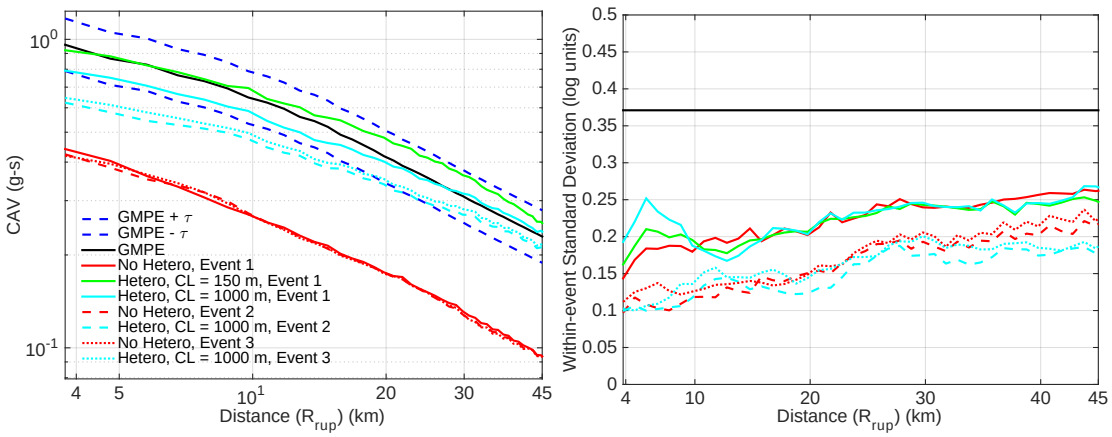

Figure 4.14: CAV versus distance for 1D layered velocity models. 'Hetero' refers to small-scale heterogeneity.

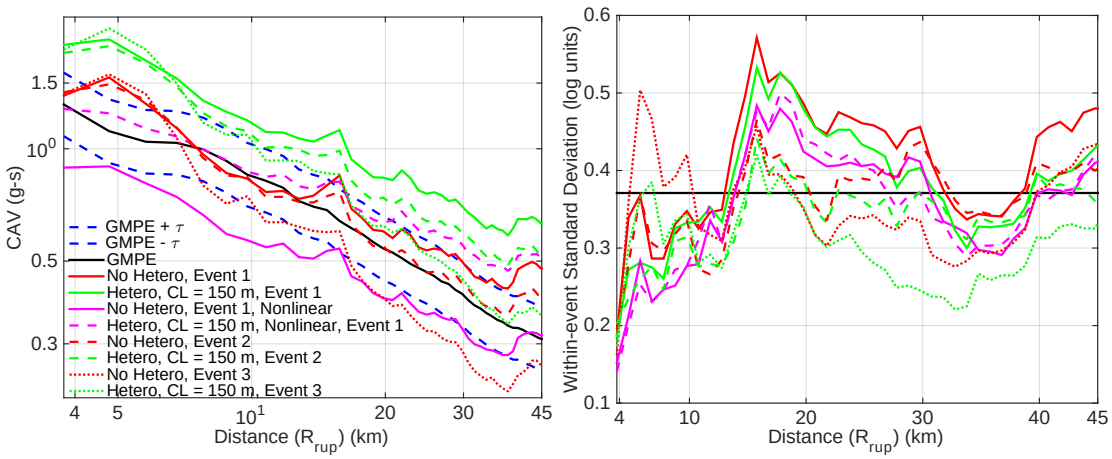

Figure 4.15: CAV versus distance for 3D background CVM velocity models for basin sites. 'Hetero' refers to small-scale heterogeneity.

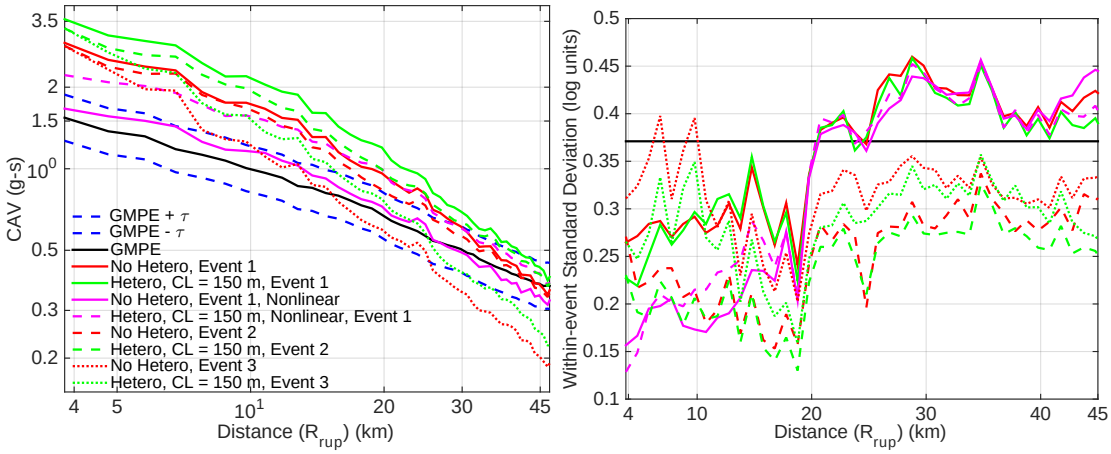

Figure 4.16: Same as Figure 4.17 but for rock sites. 'Hetero' refers to small-scale heterogeneity.

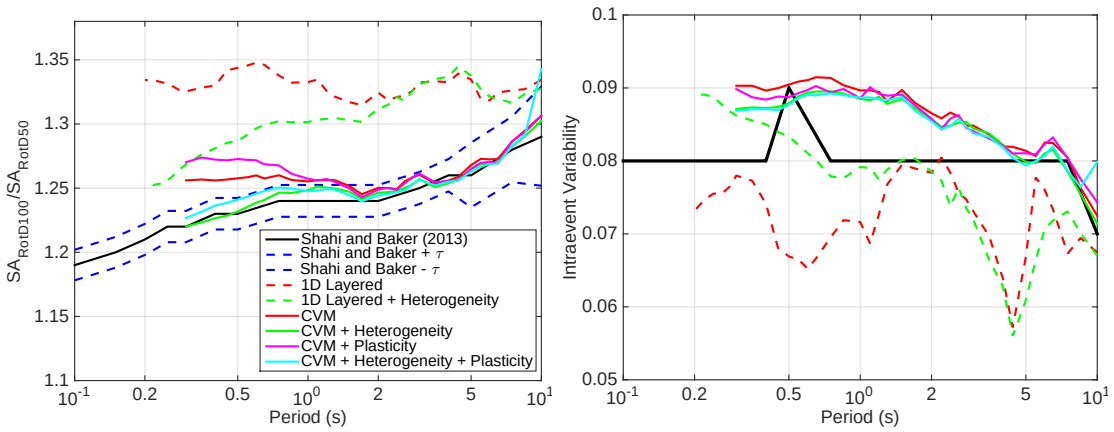

Figure 4.17: $SA_{RotD100}/SA_{RotD50}$ across period and intraevent variability prediction and comparison with synthetic models. 'Heterogeneity' refers to small-scale heterogeneity.

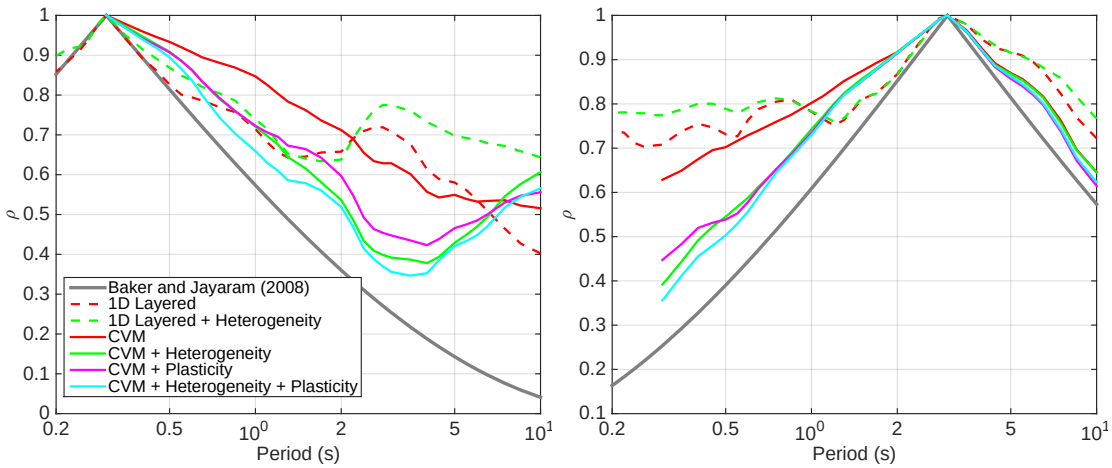

Figure 4.18: Correlation of ϵ at a reference period of (left) 0.3 and (right) 3 s for empirical and synthetic models. 'Heterogeneity' refers to small-scale heterogeneity.

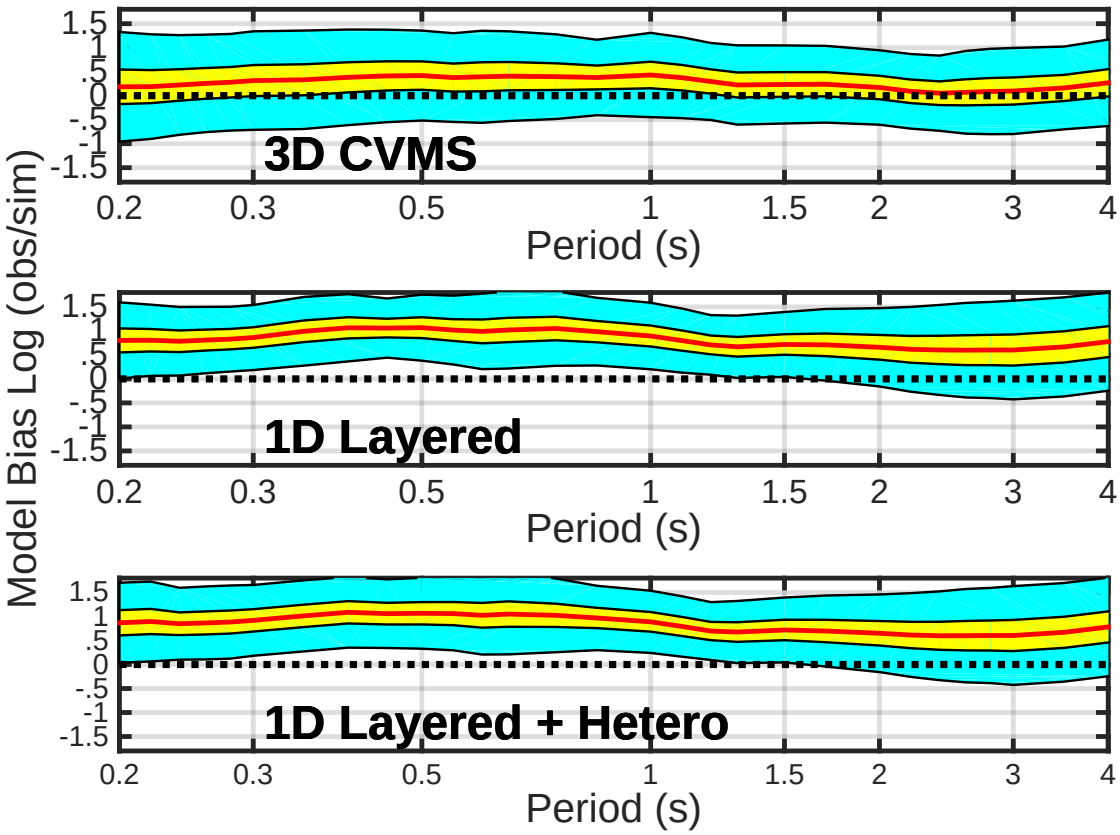

Figure 4.19: Bias (ln[data/model]) of spectral acceleration, depicting median, 95% confidence interval, and standard deviation. 'Hetero' refers to small-scale heterogeneity.

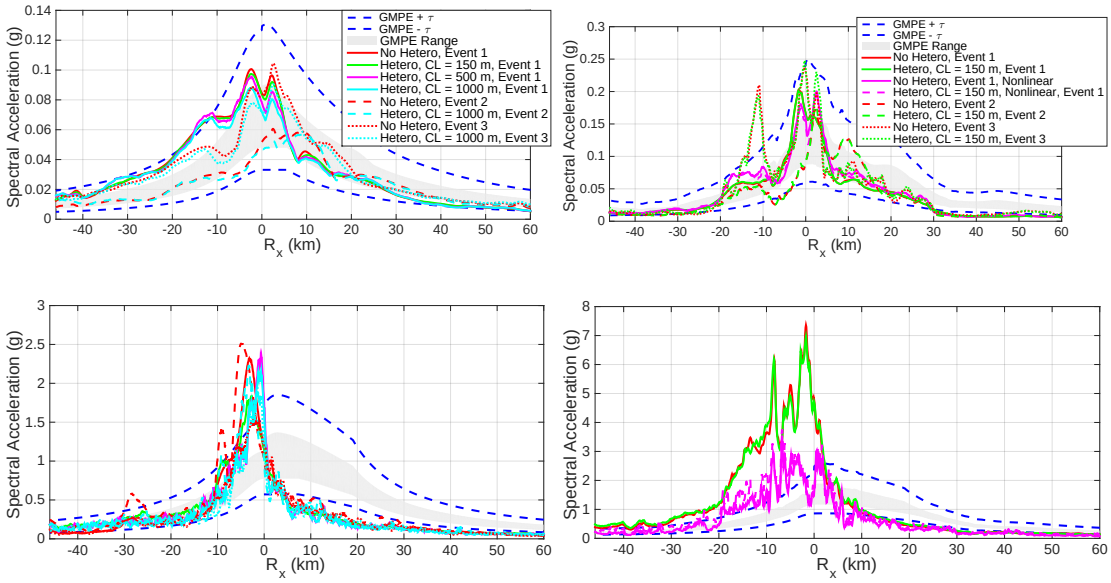

Figure 4.20: Spectral Acceleration (g) versus R_x for averaged profiles within the fault strike, for (left) 1D layered models, and (right) 3D CVM structures. (Top) is for period of 3.0 s and (bottom) for 0.3 s. 'Hetero' refers to small-scale heterogeneity.

4.10 Appendix

4.10.A Verification of the Two-step Procedure

Here we compare the accuracy of the two-step procedure, using the slip-rate time series and normal vectors output from SORD to convert to a moment-rate time-series for each subfault as the input into AWP. Figure 4.A.1 compares the SORD and AWP seismograms and frequency spectra for an example station up-dip from the hypocenter using a 1D layered model. We are only able to compare up to 4 Hz, due to the required 10 points per wavelength necessary in SORD for accurate wave-propagation in this velocity model. Using the Kristekova et al. (2009) approach to calculate the envelope and phase misfit between our models, we find envelope and phase misfits less than 5% for all components except for the fault-normal envelope, which has slightly higher error, most likely due to boundary reflections occurring late in the time series that are only partially damped within SORD .

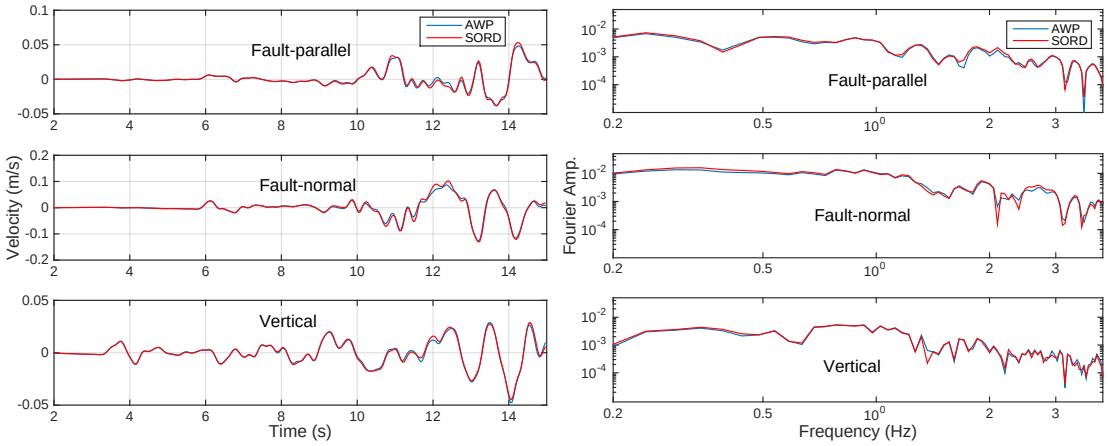

Figure 4.A.1: (Left) Comparison of fits obtained between dynamic and wave-propagation codes, SORD and AWP respectively, for (a) time-series low-passed to 4 Hz and (b) Fourier spectra.

0.49

4.11 References

References

Abrahamson, N. a., W. J. Silva, and R. Kamai (2014). Summary of the ASK14 Ground Motion Relation for Active Crustal Regions. *Earthquake Spectra*, **30**, 1025–1055. ISSN 8755-2930.

Abrahamson, N. A. and P. G. Somerville (1996). Effects of the Hanging Wall and Footwall on Ground Motions Recorded during the Northridge Earthquake. *Bull. Seism. Soc. Am.*, **86**, 93–99.

Baker, J. W. and N. Jayaram (2008). Correlation of Spectral Acceleration Values from NGA Ground Motion Models. *Earthquake Spectra*, **24**, 299–317.

Boore, D., J. Stewart, E. Seyhan, and G. Atkinson (2015). NGA-West 2 Equations for Predicting PGA, PGV, and 5%-Damped PSA for Shallow Crustal Earthquakes. *Earthquake Spectra*.

Boore, D. M. (2006). Orientation-Independent Measures of Ground Motion. *Bull. Seism. Soc. Am.*, **96**, 1502–1511. ISSN 0037-1106.

Burks, L. S. and J. W. Baker (2014). Validation of Ground-Motion Simulations through Simple Proxies for the Response of Engineered Systems. *Bull. Seism. Soc. Am.*, **104**, 1930–1946.

Campbell, K. and Y. Bozorgnia (2014). NGA-West2 Ground Motion Model for the Average Horizontal Components of PGA, PGV, and 5%-Damped Linear Acceleration Response Spectra. *Earthquake Spectra*.

Campbell, K. W. and Y. Bozorgnia (2010). A Ground Motion Prediction Equation for the Horizontal Component of Cumulative Absolute Velocity (CAV) Based on the PEER-NGA Strong Motion Databse. *Earthquake Spectra*, **26**, 635–650.

Campbell, K. W. and Y. Bozorgnia (2012). A Comparison of Ground Motion Prediction Equations for Arias Intensity and Cumulative Absolute Velocity Developed Using a Consistent Database and Functional Form. *Earthquake Spectra*, **28**, 931–941.

Chiou, B. and R. Youngs (2014). Update of the Chiou and Youngs NGA model for the average horizontal component of peak ground motion and response spectra. *Earthquake Spectra*.

Donahue, J. L. and N. Abrahamson (2014). Simulation-Based Hanging Wall Effects. *Earthquake Spectra*, **30**, 1269–1284.

Kristekova, M., J. Kristek, and P. Moczo (2009). Time-frequency misfit and goodness-of-fit criteria for quantitative comparison of time signals. *J. Geophys.*, **178**, 813–825.

Olsen, K. (2000). Site Amplification in the Los Angeles Basin from Three-Dimensional Modeling of Ground Motion. *Bull. Seism. Soc. Am.*

Roten, D., K. B. Olsen, S. M. Day, Y. Cui, and D. Fäh (2014). Expected seismic shaking in Los Angeles reduced by San Andreas fault zone plasticity. *Geophys. Res. Lett.*, **41**, 2769–2777.

Roten, D., K. B. Olsen, and J. C. Pechmann (2012). 3D Simulations of M 7 Earthquakes on the Wasatch Fault, Utah, Part II: Broadband (0-10 Hz) Ground Motions and Nonlinear Soil Behavior. *Bull. Seism. Soc. Am.*, **102**, 2008–2030. ISSN 0037-1106.

Roten, D., K. B. Olsen, J. C. Pechmann, and H. Magistrale (2011). 3D Simulations of M 7 Earthquakes on the Wasatch Fault , Utah , Part I : Long-Period (0 1 Hz) Ground Motion. *Bull. Seism. Soc. Am.*, **101**, 2045–2063.

Shahi, S. K. and J. W. Baker (2014). NGA-West2 Models for Ground Motion Directionality. *Earthquake Spectra*, **30**, 1285–1300.

Shi, Z. and S. M. Day (2013). Rupture dynamics and ground motion from 3-D rough-fault simulations. *J. Geophys.: Solid Earth*, **118**, 1122–1141. ISSN 21699313.

Wald, D. J., T. H. Heaton, and K. W. Hudnut (1996). The Slip History of the 1994 Northridge , California , Earthquake Determined from Strong-Motion, Teleseismic, GPS, and Leveling Data. *Bull. Seism. Soc. Am.*, **86**, 49–70.

Withers, K. B., K. B. Olsen, and S. M. Day (2015). Memory-Efficient Simulation of Frequency-Dependent Q. *Bull. Seism. Soc. Am.*, **105**, 3129–3142.

Chapter 5

Conclusions

5.0.1 Overview

The objective of this thesis was to better constrain seismic hazard in the bandwidth important for engineering applications by deterministically modeling broadband seismic ground motion, with application to regions with poor data coverage. This study helped determine the importance of different components in broadband ground motion simulations that contribute to the level of seismic hazard. This included the impact of the source from both a generic strike-slip fault and a suite of dynamic ruptures occurring along a blind thrust dip-slip fault, as well as contributions from the medium, such as anelastic attenuation, scattering from small-scale heterogeneities, and nonlinear effects such as plasticity. The synthetic ground motion was validated by using empirical data by first comparing with leading ground motion prediction equations as well as a group of proxy metrics that a wide range of data has been shown to be consistent with.

Whereas available computational resources have limited previous deterministic ground motion studies, this research used the Titan supercomputer's GPUs to extend ground motion prediction to higher frequencies using a 3D fourth-order staggered-grid finite difference method (AWP-ODC) with a grid spacing of 20 m. We deterministically model earthquakes by incorporating realistic fault topography in 3D simulations of earthquake source models and include scattering effects caused by small-scale velocity and density heterogeneities in the medium

(that match borehole studies in a statistical sense) affecting the ground motion intensity. To further increase the accuracy of our model, we have implemented frequency-dependent attenuation via a power law above a reference frequency.

We model generic strike-slip events and blind thrust earthquakes matching the fault dimensions of the 1994 Northridge earthquake extending up to 8 Hz. First, we perform the dynamic rupture propagation using SORD along several realizations of rough fault topographies. An ensemble of displip scenarios is modeled by varying the hypocenter location that results in similar moment magnitudes. The slip-rate data is converted to a kinematic source and input into the wave propagation code AWP-ODC, which incorporates frequency-dependent attenuation as well as Drucker-Prager plasticity. We also include small-scale medium complexity in both a 1D-layered model and a 3D medium extracted from SCEC CVM-S4 including a surface geotechnical layer. The ground motion is analyzed spatially by binning the ground motion as a function of distance and comparing with GMPEs.

5.1 Summary of findings

We find that the spectral acceleration at various periods from our models are typically within 1 inter-event standard deviation from the median GMPEs and compare well with that of recordings from strong ground motion stations at both short and long periods. At periods shorter than 1 second, Q(f) is needed to match the decay of spectral acceleration seen in the GMPEs as a function of distance from the fault, using a Q(f) power-law exponent in the range $0.6 - 0.8$. Plasticity is needed to reduce near-field ground motion to that near observable levels in regions of near-surface low velocity layers. Small-scale media complexity is observed to decrease the polarization ratio to that of similar to observations. We find that when binning stations with a common distance metric that media heterogeneity can also have a significant impact on the level of ground motion (both decreasing and increasing it), due to scattering attenuation and redistribution of energy.

Small-scale heterogeneity can significantly affect the intra-event variability at frequencies greater than $\sim$ 1 Hz, becoming increasingly important at larger dis-

tances from the source. The intra-event variability of our simulations in the CVM is typically larger than that for the observations at frequencies > 1 Hz. However, this discrepancy tends to decrease when small-scale heterogeneity in the medium is included in the simulations, suggesting the need for a highly complex velocity model to fit ground motion variability. Plastic effects in the medium also reduce the variability, particularly at distances close to the source. The intra-event variability for the layered model simulations is near observed values of single-station standard deviation. Also, the agreement of intra-event variability between simulations and observations increases when small-scale heterogeneity is included, in some cases dramatically reducing the uncertainty. This is particularly important, because uncertainty in ground motion estimates dominates the overall uncertainty in seismic risk.

Additionally, we showed that it is important to compare our synthetic ground motion with alternative metrics, to emphasize the importance of different components we include within our simulations. An example is the 5-95% duration of Arias Intensity, where small-scale heterogeneity has a significant effect on the durations, due to the scattering of energy into the coda. Also, there is a group of proxy ground motion metrics that a wide range of data has been consistently shown to agree with. It is important to verify that our simulations are realistic and comparable to that of these ground motion proxies if they are to be used for future seismic hazard purposes. One example we used was the the maximum-to-median spectral acceleration across all horizontal orientations. It was shown that full 3D complexity in the velocity model, both on the large scale extracted from the CVM and the small-scale from heterogeneities is needed to match empirical observations. Other proxies also emphasized the importance of different components to include within our simulations, for example the correlation of spectral acceleration across periods and the characteristic pulse period.

5.2 Future research directions

Future simulations will add potentially even further complexities, e.g. topography, a damage zone along the fault, etc. A goal will be to identify key components (particularly path and site effects) using the computational simulations that contribute to the uncertainty in ground motion across a bandwidth appropriate to earthquake hazard assessment, with the goal of better characterizing and reducing the intra-event variability. Simulations will be designed to first match recent events, where strong ground motions records exist. After validation of the approach, the procedure will be applied in regions with poor data coverage. A focus will be on simulating ground motion for possible future events, using existing community velocity models for the region. This well help to better determine future ground motion and its variability, to better constrain seismic hazard. With these simulations, characterization of different effects could be implemented into the framework of ground motion prediction equations to better determine and constrain ground motion, essential to properly assigning seismic hazard and risk.